Spring 5-15-2019

Preclinical Imaging of Multiple Myeloma Therapy Response

Deep Hathi
Washington University in St. Louis

Recommended Citation

Hathi, Deep, "Preclinical Imaging of Multiple Myeloma Therapy Response" (2019). *McKelvey School of Engineering Theses & Dissertations*. 446.
https://openscholarship.wustl.edu/eng_etds/446

WASHINGTON UNIVERSITY IN ST. LOUIS

School of Engineering and Applied Sciences

Department of Biomedical Engineering

Dissertation Examination Committee:
Monica Shokeen, Chair
Samuel Achilefu
Joseph J.H. Ackerman
Mark Anastasio
Joel R. Garbow
Kooresh Shoghi
Jonathan Silva

Preclinical Imaging of Multiple Myeloma Therapy Response

by

Deep K. Hathi

A dissertation presented to
The Graduate School
of Washington University in
partial fulfillment of the
requirements for the degree
of Doctor of Philosophy

May 2019
Saint Louis, Missouri

Table of Contents

List of Figures iv
List of Tables viii
Acknowledgments ix
Abstract xi
Chapter 1: Introduction 1
1.1 Overview 1
1.2 Significance 2
1.2.1 MM is a plasma cell dyscrasia with spatiotemporal heterogeneity 2
1.2.2 *Interaction between myeloma cells and their BM niche is critical to progression and survival* 5
1.2.3 MM treatment strategies induce significant changes in BM-resident cells and affect the BM microenvironment 13
1.2.4 Summary 21
1.3 Noninvasive imaging provides spatiotemporal sampling of MM staging 22
1.3.1 Introduction 22
1.3.2 Applications of PET/CT in assessing therapy response 23
1.3.3 Magnetic resonance imaging is increasingly applied to MM diagnosis and staging…………………………………………………………………………………….. 30
1.3.4 *Near-infrared optical imaging provides high-throughput preclinical functional imaging*…. 35
1.4 Summary 37
1.5 Specific aims and Dissertation outline 38
1.5.1 Specific aims 38
1.5.2 Dissertation outline 39
1.6 References 40
Chapter 2: Imaging melphalan therapy response in preclinical extramedullary myeloma with ^{18}F-FDOPA and ^{18}F-FDG PET 50
2.1 Overview 50
2.2 Introduction 50
2.3 Materials and Methods 52
2.3.1 Cell Culture and Reagents 52
2.3.2 Tumor Model and Melphalan Therapy 52
2.3.3 In vivo Structural and Metabolic Imaging 53
2.3.4 PET Image Analysis 54
2.3.5 Immunohistochemistry 54
2.3.6 Statistical Analysis 55
2.4 Results 55
2.5 Discussion 63
2.6 Conclusion 66
2.7 References 67
Chapter 3: Near-infrared imaging of VLA-4 expression for monitoring bortezomib efficacy in preclinical MM 70
3.1 Overview 70
3.2 Introduction 70

3.3 Materials and Methods 72
  3.3.1 Cell culture and reagents 72
  3.3.2 In vitro LLP2A-Cy5 uptake and specificity 72
  3.3.3 Saturation binding assay 72
  3.3.4 Tumor model and bortezomib therapy 73
  3.3.5 In vivo NIR imaging 73
  3.3.6 Statistical analysis 73
3.4 Results 74
3.5 Discussion 79
3.6 Conclusion 81
3.7 References 81
Chapter 4: Longitudinal MRI of bortezomib-treated diffuse tumor burden in intramedullary myeloma 84
4.1 Overview 84
4.2 Introduction 85
4.3 Materials and Methods 86
  4.3.1 Cell culture and reagents 86
  4.3.2 Tumor model and bortezomib therapy 86
  4.3.3 Preclinical MRI 87
  4.3.4 Bone histology and imaging 88
  4.3.5 Data analysis 88
  4.3.6 Statistical analysis 89
4.4 Results 90
  4.4.1 Observed differences in normalized 3D CE T1-weighted MRI 90
  4.4.2 Effect of disease stage and bortezomib therapy on T2 parametric maps 94
  4.4.3 Validation of imaging results with H&E of femur and tibia BM 96
4.5 Discussion 99
4.6 Conclusion 102
4.7 References 103
Chapter 5: Conclusions and Future Work 106
5.1 Summary 106
5.2 Limitations 108
5.3 Future work 110
5.4 Conclusions 111

List of Figures

Figure 1.1: Summary of incidence and mortality rates for MM for male and female populations in the world. Reprinted from (2). 2

Figure 1.2: Summary of MM progression and genetic diversity. Reprinted from (6). 3

Figure 1.3: Summary of B cell maturation pathways and terminally differentiated states. NK, natural killer; DC, dendritic cell; HSC, hematopoietic stem cell; ELP, early lymphoid progenitor; CLP, common lymphoid progenitor; CSR, class switch recombination; MZB, marginal zone B cells. Reprinted from (7). 4

Figure 1.4: Summary of BM physiology and cellular components. MSC, mesenchymal stem cells; HSC, hematopoietic stem cells; CAR cell, CXCL2 abundant reticular cell. Adapted and reprinted from (12). 7

Figure 1.5: Summary of the feed-forward loop between tumors and osteolysis, through direct (solid arrows) and indirect (dotted arrows) means. (MMPs, matrix metalloproteinases; PTHRP, parathyroid hormone-related protein). MMP2s cleave membrane-bound RANKL (blue balls on the surface of osteoblasts) or epidermal growth factor-like proteins (red diamonds), resulting in an increased osteoclastogenesis via a higher ratio of RANKL to osteoprotegerin. Reprinted from (45). 12

Figure 1.6: Treatment strategy for risk strata and transplant eligibility in newly diagnosed MM patients. (a) Approach in transplant-eligible patients. (B) Approach in elderly, transplant-ineligible patients. VD, bortezomib-dexamethasone; VCD, bortezomib-cyclophosphamide-dexamethasone; VMP, bortezomib-melphalan-predinisone; VRd, bortezomib-lenalidomide-dexamethasone. Reprinted from (52). 14

Figure 1.7: Summary of apoptotic pathways induced by bortezomib-mediated inhibition of the catalytic 26S proteasome. Reprinted from (55). 17

Figure 1.8: Summary of (A) microenvironment and (B) immune system effects induced by IMiDs. APC, antigen-presenting cell; NKT cell, NK cells with T lymphocyte markers and functionality; ADCC, antibody-dependent cellular cytotoxicity. Adapted and reprinted from (73). 20

Figure 1.9: Summary of the types of possible coincidence events in a PET scanner following positron annihilation. Reprinted from (91). 25

Figure 1.10: Representative T1-weighted (left) and fat-suppressed (fs) T2-weighted (right) MRI of spinal column in a patient with symptomatic MM. White arrow, focal lesion; red arrowhead, diffuse infiltration. Adapted and reprinted from (102). 33

Figure 1.11: Absorption spectra of common tissue components. Hb, deoxygenated hemoglobin; HbO2, oxygenated hemoglobin. Reprinted from (111). 36

Figure 2.1: Timeline for melphalan treated and untreated cohorts. Melphalan was administered weekly beginning either (A) week 2, with imaging performed on separate, contiguous days at the end of the study, or (B) week 3 post tumor implantation. Longitudinal imaging with MRI, ^{18}F-FDG, and ^{18}F-FDOPA PET/CT was initialized prior to the start of therapy for the week 3 cohort and continued through to week 5 post tumor implantation. 53

Figure 2.2: Representative T_2-weighted MRI transverse images of (A) untreated, (B) week 2-4 treated, and (C) treated weeks 3-5 post tumor implantation, at the (left) pre-treatment baseline and weeks (middle) 4 and (right) 5. 56

Figure 2.3: Localization of tumor and average time activity profile in treated and untreated 5TGM1 tumor-bearing C57Bl/KaLwRij mice imaged with ^{18}F-FDG and ^{18}F-FDOPA PET/CT. Representative co-registered PET/CT transverse view of (left) untreated and (right) treated tumors in dynamic (A) ^{18}F-FDG and (B) ^{18}F-FDOPA imaging. TACs from (C) ^{18}F-FDG and (D) ^{18}F-FDOPA are displayed (mean ± SEM at each time point), with statistical significance calculated using the 2-way ANOVA with repeated measures (*** $p < 0.001$). 57

Figure 2.4: Distribution of ^{18}F-FDG and ^{18}F-FDOPA uptake and avidity metrics in treated and untreated 5TGM1 tumor-bearing C57Bl/KaLwRij mice. Scatter plots with mean and SEM distributions are displayed for (A) TLA (left) and TLG (right), (B) SUV_{Max}, and (C) total uptake for ^{18}F-FDOPA (left) and ^{18}F-FDG (right). Statistical significance between treated and untreated cohorts for TLA and TLG was calculated using the two-tailed Student's t-test, while 1-way ANOVA with the Bonferroni multiple comparison post-test was used to assess statistical significance between groups and tissue for SUV_{Max} and total uptake (* $p < 0.05$, ** $p < 0.01$, and *** $p < 0.001$). 58

Figure 2.5: Representative maximum intensity projections of longitudinal (A) ^{18}F-FDG and (B) ^{18}F-FDOPA-PET/CT at the pretreated baseline and weeks 1 and 2 during melphalan therapy. 60

Figure 2.6: Distribution of ^{18}F-FDOPA and ^{18}F-FDG uptake metrics during longitudinal treatment and imaging. (A) TACs for ^{18}F-FDOPA (left) and ^{18}F-FDG (right), with statistical significance calculated with 2-way ANOVA with repeated measures and Bonferroni comparisons post-test. (B) TLA (left) and TLG (right) were calculated for each week, as were (C) SUV_{Max} and (D) total uptake from ^{18}F-FDOPA and ^{18}F-FDG TACs. Time points (weeks 1 and 2) were relative to pre-treatment baseline (week 3 post tumor implantation). Statistical significance for the individual comparisons was calculated using 1-way ANOVA with Tukey post-hoc test (*$p<0.05$, **$p<0.01$, ***$p<0.001$). 61

Figure 2.7: Immunohistochemistry of LAT1 (top) and GLUT1 (bottom) expression for (A) untreated and treated tumors with initialization of melphalan therapy at (B) weeks two and (C) three post tumor implantation. Expression for each stain was visualized as a maximum intensity projection (63X magnification; 20µm scale bar) separately and as a composite with GFP (green) and DAPI nuclear stain (blue). 62

Figure 2.8: Immunohistochemistry of CD31 (top) and CD98 (bottom) for representative (A) untreated and (B) treated tumors with initialization of melphalan therapy at week 2 post tumor implantation. Expression for each stain was visualized as a maximum intensity projection (63X magnification; 20µm scale bar) separately and as a composite with GFP (green) and DAPI nuclear stain (blue). 63

Figure 3.1: Representative confocal fluorescent images of LLP2A-Cy5 binding in 5TGM1 cells. (A) 1 µM LLP2A-Cy5, (B) 1 µM scLLP2A-Cy5, and (C) 1 µM LLP2A-Cy5 in presence of 100 µM unlabeled LLP2A, were incubated with 5TGM1-GFP cells at 4^{o}C for 15 min. (D) 5TGM1 cells were incubated with 1 µM LLP2A-Cy5 at 37^{o}C for 2.5 h. A-C, 60X magnification, scale bar, 15 µm; D, 100X magnification, scale bar, 3um. Blue channel, DAPI; Red channel, Cy5. 75

Figure 3.2: LLP2A-Cy5 uptake in 5TGM1 cells *in vitro*. (A) Total uptake in cells at 4^{o}C (15 min incubation). Integrated density is the product of the region of interest area and mean intensity value. (B) Saturation binding of LLP2A-Cy5 in 5TGM1 cells. Statistical significance was assessed using 1-way ANOVA with Tukey multiple comparisons test (***p<0.001)..................76

Figure 3.3: Representative 18-24 h fluorescence signal in C57Bl/KaLwRij mice bearing diffuse, intramedullary 5TGM1 tumors. (A) Untreated, week 4 post tumor implantation. (B) Bortezomib treated, week 6 post implantation. (Left) GFP, (Middle) Cy5, (Right) Overlay of GFP and Cy5 signal. Scale bar, 10mm....77

Figure 3.4: Ex vivo fluorescence biodistribution in end-stage treated and untreated mice. Background subtracted fluorescence intensity in each tissue was normalized by the mean muscle intensity, and presented as Tissue to Muscle ratios. (A) LLP2A-Cy5 biodistribution. (B) GFP biodistribution. Statistical significance was assessed using 2-way ANOVA with Sidak multiple comparisons test (*$p<0.05$). 78

Figure 3.5: FACS of treated and untreated BM in the femur and tibia. The cell population is the percentage of GFP^+ and $LLP2A\text{-}CY5^+GFP^+$ cells within all cells in the BM. Statistical significance was assessed using the Student's two-tailed t-test within each gated group (**$p<0.01$, ns, not significant). 78

Figure 4.1: Study design, imaging, and therapy timeline. Untreated tumor-bearing (N = 5) 5TGM1/KaLwRij were imaged weekly with non-CE T2 parametric mapping and 3D CE T1-weighted MR weekly beginning two weeks post 5TGM1 tumor implantation. The bortezomib treatment cohort (N = 9) was similarly implanted with 5TGM1 tumors and injected with bortezomib via intraperitoneal injection at 1 mg/kg twice a week, beginning two weeks post tumor implantation. On imaging days (e.g., day 14, 21, 28), therapy and vehicle injections were performed immediately following imaging. As with the untreated tumor-bearing cohort, each mouse was imaged weekly with non-CE T2 parametric mapping and a 3D CE T1-weighted pulse sequence....87

Figure 4.2: Representative sagittal sections of T1-weighted CE-MRI. Each voxel in the volume was normalized by the mean of representative muscle VOI located in the lower leg. (A) Non-tumor bearing. (B) Untreated tumor-bearing, week 4. (C) Treated tumor-bearing, week 6. Red arrows highlight regions of significant spatial intensity variation. Scale bar, 4 mm....90

Figure 4.3: Gray-level, normalized, CE T1-weighted representative sagittal sections. Images were normalized by distributing the grayscale intensity value of each voxel into 8 equal-width bins. (A) Non-tumor bearing. (B) Untreated tumor-bearing, week 4. (C) Treated tumor-bearing, week 6. Scale bar, 4 mm....91

Figure 4.4: Representative sagittal sections of T1-weighted CE and T2 parametric images of mid-series time points in untreated and treated tumor-bearing mice. (A-B) T1-weighted CE 3D MRI, normalized by the mean voxel intensity of the representative muscle ROI in untreated (week 3) and treated (week 4) tumor-bearing. (C-D) T1-weighted CE 3D MRI, normalized by gray level equalization. (E-F) T2 parametric maps of femur and tibia ROIs overlaid on T1-weighted non-CE oblique slices. Scale bar, 4 mm; T2 range, 0-60 ms....92

Figure 4.5: Mean autocorrelation of 3D gray-level co-occurrence matrix (GLCM) in tibia and femur VOIs in T1-weighted CE images. (A) Mean GLCM autocorrelation for non-tumor bearing (NT), untreated tumor-bearing at weeks 3 (U3) and 4 (U4), and treated tumor-bearing at weeks 3-4 (MT) and weeks 5-6 (ET) groups. (B) Mean GLCM autocorrelation relative to week 2 baseline for each animal (%difference = (Time-point Mean – Baseline Mean)/(Baseline Mean)). Statistical significance was assessed using a one-way ANOVA with Tukey multiple comparisons test performed individually on the tibia and femur VOIs (*$p < 0.05$). Whiskers indicate 5-95% confidence intervals. 93

Figure 4.6: Mean CE T1-weighted intensity, normalized by mean muscle intensity, in femur and tibia VOIs. (A) Mean CE T1-weighted normalized intensity in non-tumor bearing (NT) mice,

untreated tumor bearing mice at weeks 3 (U3) and 4 (U4), and treated tumor-bearing mice at weeks 3-4 (MT) and 5-6 (ET). (B) Mean CE, T1-weighted normalized intensity relative to week 2 baseline for each animal (%difference = (Time-point Mean – Baseline Mean)/(Baseline Mean)). Statistical significance was calculated using a one-way ANOVA with the Tukey multiple comparisons test performed individually on the tibia and femur VOIs (*p < 0.05, **p < 0.01, ***p < 0.001; closed line indicates comparison between two groups, open-ended line indicates statistical significance between one group against all other included groups). Whiskers indicate 5-95% confidence intervals. 93

Figure 4.7: Representative T2 parametric maps of femur and tibia BM. (A) Non-tumor bearing mice. (B) Untreated tumor-bearing mice, week 4. (C) Treated tumor-bearing mice, week 6. Femur and tibia T2 maps were overlaid on non-CE, oblique, T1-weighted intensity images normalized by the mean voxel intensity of the muscle ROI. Scale bar, 4 mm; T2 range 0-60 ms. 94

Figure 4.8: Mean T2 in femur and tibia VOIs. (A) Mean T2 in non-tumor bearing (NT) mice, untreated tumor-bearing mice at weeks 3 (U3) and 4 (U4), and treated tumor-bearing mice at weeks 3-4 (MT) and weeks 5-6 (ET). (B) Mean T2 relative to week 2 baseline for each animal (%difference = (Time-point Mean – Baseline Mean)/(Baseline Mean)). Statistical significance was assessed using a one-way ANOVA with Tukey multiple comparisons test performed individually on the tibia and femur VOIs (*p < 0.05, **p < 0.01, ***p < 0.001; closed line indicates comparison between two groups, open-ended line indicates statistical significance between one group against all other included groups). Whiskers indicate 5-95% confidence intervals...........95

Figure 4.9: Representative H&E sections. (A) Non-tumor bearing mice. (B) Untreated tumor-bearing mice, week 4. (C) Treated tumor-bearing mice, week 6. Green outline indicates tumor boundaries. Top inset highlights non-tumor cells, as indicated by the presence of megakaryocytes (red arrowhead) and segmented nuclei (red arrow). The bottom inset highlights tumor cells, as indicated by the presence of mitoses (green arrowhead) and oval plasma cell nuclei (green arrow). Scale bar, 500 µm; inset scale bar, 20 µm. 97

Figure 4.10: Representative H&E sections and quantification of total tumor burden. (A) Mid-treatment, week 4. Green outline indicates tumor boundaries. Top inset highlights non-tumor cells, as indicated by the presence of segmented nuclei (red arrows). Bottom inset highlights tumor cells, as indicated by the presence of mitoses (green arrowheads) and oval plasma cell nuclei (green arrows). (B) %Tumor burden in untreated week 4 (U4) and treated weeks 3-4 (MT) and weeks 5-6 (ET) (%tumor burden = (Total Tissue Area – Non-tumor Area)/(Total Tissue Area)*100%). Statistical significance was assessed using one-way ANOVA with Tukey multiple comparisons test on the tibia and femur individually (***p<0.001). Whiskers denote 5-95% confidence intervals. Scale bar, 500 µm; Inset scale bar, 20 µm. 98

List of Tables

Table 2.1: Summary of ^{18}F-FDOPA and ^{18}F-FDG measurements 56

Table 2.2: Summary of Lin's correlation coefficient relative to ^{18}F-FDG-PET/CT parameters ... 59

Table 4.1: Summary of MR markers and their corresponding biological features for each imaging group relative to the untreated week 4 group. 0, no effect; +, difference in features; ++, significant difference in features. 99

Acknowledgments

Dr. Monica Shokeen provided exceptional mentorship and support over the course of my doctoral research. Her knowledge of the field, attention to detail, and limitless energy were an inspiration to me and helped me push the boundaries in my work. Dr. Shokeen's patience and teaching ability transformed my outlook in research, and made me a better scientist that is unafraid to explore and ask the big questions of the field. I thank her for providing me with intellectually challenging and rewarding research questions and for building a rigorous foundation to my scientific education.

Dr. Samuel Achilefu has been an excellent and endless source of advice and inspiration throughout my graduate education. He has provided creative solutions and continually challenged me to explore and integrate lateral thinking into my doctoral research. His guidance and mentorship have helped foster my scientific growth and helped me become an independent scientist.

I would like to thank my colleagues in the Shokeen Lab and the Optical Radiology Lab for their continual support, in both personal and scientific pursuits. Dr. Anchal Ghai and Nicholas Cho in the Shokeen Lab have supported me in all my projects and are a source of inspiration for me for their unstinting work ethic, leadership, and ability to develop ideas into innovative research directions. Nicholas Cho has assisted me in several of my projects, particularly with animal handling and imaging, tissue culture experiments, and data analysis and presentation. Ms. Gail Sudlow in the Optical Radiology Lab has assisted me in all of my animal handling efforts, especially in providing training and performing critical injections and implantations.

I am grateful to my external collaborators Dr. Jonathan McConathy and Dr. Walter Akers. Dr. McConathy provided initial impetus in driving my first aim and provided valuable clinical insights into imaging for multiple myeloma. Dr. Akers provided mentorship and training during my early years in the doctoral program, and especially helped me learn critical animal

handling skills. His expertise and enthusiasm were inspiring and assisted me in developing independence as a researcher.

My friends have provided me with endless support that has been critical for maintaining constant excellence and a positive attitude through all stages of my graduate education. I would especially like to thank Dr. Andrew Badachhape, Dr. Suman Mondal, Dr. Dolonchampa Maji, Debbie Yee, Dr. Rebecca Gilson, and many others for providing me with timely advice on navigating research and in helping fuel my personal and scientific growth over the years.

I would like to thank my family for their continued patience and support for me throughout my education and beyond. My parents, my brother Shobhit, and my fiancée Disha have helped me work through difficult times in my PhD education and have remained a continual source of inspiration and advice.

Finally, I would like to acknowledge funding from the National Cancer Institute (NCI) grants R01 CA176221 and U54 CA199092. Support was also provided from the National Institutes of Health (NIH) CA094056, DE-SC0012737, K08CA154790, and pilot imaging funds from the Mallinckrodt Institute of Radiology at the Washington University School of Medicine.

Deep K. Hathi

Washington University in St. Louis

May 2019

ABSTRACT OF THE DISSERTATION

Multiple myeloma (MM) is a debilitating hematologic malignancy of terminally differentiated plasma cells in the bone marrow (BM). Advances in therapeutic regimens and the use of autologous stem cell transplantation have significantly improved survival rates and quality of life in patients. However, the disease remains incurable, with shorter, successive remission cycles following relapse. To reduce systemic, off-target toxicity and improve quality of life, there is a need for improved stratification of responding patients. Identification of specific, noninvasive, imaging biomarkers that correlate to therapeutic efficacy is an attractive strategy for stratifying responding patients, since the use of positron emission tomography (PET), computed tomography (CT), and magnetic resonance imaging (MRI) is clinically established. Here, we have developed a strategy for imaging MM disease pathogenesis and response to clinically relevant therapeutics by studying the bidirectional interactions between the BM microenvironment and myeloma cells at the cellular, environmental, and anatomical levels. Specifically, we have validated imaging markers that identify BM and myeloma-specific behaviors through three specific aims:

The first aim validated the use of the phenylalanine analog ^{18}F-FDOPA for monitoring the uptake and efficacy of the DNA alkylating agent melphalan, which is used extensively in elderly, non-transplant eligible patients and in relapsed, refractory disease. ^{18}F-FDOPA uptake was significantly reduced in melphalan-treated mice with orthotopic myeloma tumors, and was concordant with the established ^{18}F-FDG-PET imaging. Immunohistochemistry was used to validate ^{18}F-FDOPA uptake results. Importantly, expression of LAT1, which is known to mediate ^{18}F-FDOPA and melphalan uptake, was visibly increased, although this may be a result of increased tumor vascularity. Our results suggest that ^{18}F-FDOPA-PET can provide complementary imaging to ^{18}F-FDG-PET for monitoring response to melphalan therapy and overall LAT1 expression in MM.

The second aim assessed the specificity and sensitivity of the peptidomimetic near-infrared fluorophore LLP2A-Cy5 for imaging the expression of the activated conformation of the VLA-4 integrin on the surface of myeloma cells. LLP2A-Cy5 imaging was also used to study response to treatment with the proteasome inhibitor bortezomib, which forms the backbone of several front-line MM therapy strategies. Uptake of LLP2A-Cy5 was significantly reduced in bortezomib-treated mice bearing intramedullary tumors, indicating a reduction in the expression of activated VLA-4. These observations are concordant with the known downregulation of adhesion-mediated drug resistance and VLA-4 by bortezomib. Our results indicate the viability of using LLP2A-Cy5 near-infrared imaging for sensitive, longitudinal assessment of VLA-4 expression for monitoring bortezomib treatment response.

Finally, the third aim validated the use of preclinical, multi-parametric MRI for studying changes in the BM in a diffuse infiltrative intramedullary tumor model. Longitudinal imaging of the BM in the femur and tibia demonstrated significant regional differences in T1-weighted contrast uptake and parametric T2 that correlated to changes in viable tumor burden following treatment with bortezomib. Hematoxylin and eosin staining (H&E) was used to validate the MRI observations. H&E showed complete diffuse infiltration of the BM in untreated animals, while bortezomib therapy caused the concentration of tumor burden near the epiphyseal plate of the distal femur and proximal tibia. These observations, in combination with MRI results, establish the use of preclinical MRI for studying effects of disease progression and therapy response on the BM in a longitudinal, noninvasive manner.

In summary, these studies established a combination of qualitative observations and quantitative results in PET, optical, and MRI based strategies. Thus, this project has integrated a structured, multi-modal approach for assessing changes in tumor burden and monitoring therapy response at varying granular levels within the myeloma/BM interaction spectrum. Future studies would adapt this approach into different cell lines and tumor models.

Chapter 1: Introduction

1.1 Overview

Multiple myeloma (MM) is an incurable, debilitating hematologic malignancy of terminally differentiated plasma B-cells in the bone marrow (BM). It is the second most common hematologic malignancy and accounts for 15-20% of all hematologic malignancy-related mortalities (*1,2*). In the United States alone, there were over 30,000 estimated new cases and over 12,000 deaths in 2018 (*3*). MM median 5-year survival has improved from 34.6% in 2004 to 49.6% in 2013 (*4,5*). This increase in survival is linked to the improvements in diagnosis and the availability of autologous stem cell transplantation and combination therapies consisting of immunomodulatory drugs, proteasome inhibitors, and other chemotherapeutics. However, therapy efficacy in the MM clinical population remains variable, especially at late stages in MM disease progression. Implementation of personalized stratification strategies is crucial towards improving patient quality of life and reducing toxicities and costs associated with ineffective therapies. Noninvasive, whole-body imaging has the potential for improving stratification, with spatiotemporal localization of therapy response in the MM population. Molecular and structural imaging of MM burden and its effects on the BM environment can be studied at progressing levels of granularity, ranging from whole tissue to single cell surface biomarker expression. This chapter reviews the underlying MM biology, the impact of the BM niche on MM progression, current and future treatment strategies, and the increasing use of noninvasive imaging for diagnosis and staging. The section concludes with an overview of the three specific aims encompassing the efforts towards furthering MM molecular imaging for assessing therapy response in preclinical MM.

1.2 Significance

1.2.1 MM is a plasma cell dyscrasia with spatiotemporal heterogeneity

Multiple myeloma (MM) is a semi-solid plasma cell dyscrasia that develops in bone marrow (BM) sites, prior to metastasizing to extramedullary lesions. Traditionally, MM is characterized by abnormal serum levels of non-functional monoclonal immunoglobulin-G (IgG; M-protein) and the presence of hyper**c**alcemia, **r**enal failures, **a**nemia, and **b**one fractures (CRAB) symptoms. MM is the second most common hematologic malignancy after lymphoma and predominantly affects 65+ year-old adults. **Figure 1.1** highlights the epidemiology and the primary affected populations.

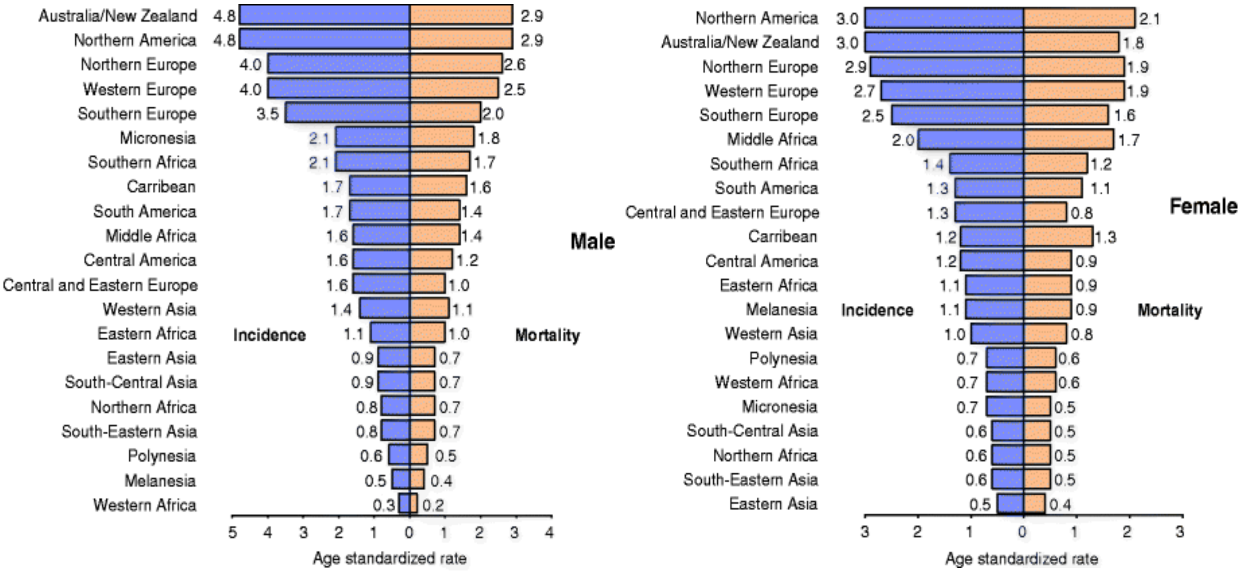

Figure 1.1: Summary of incidence and mortality rates for MM for male and female populations in the world. Reprinted from (*2*).

Interestingly, myeloma is a spectrum disease, characterized by a transition from relatively asymptomatic stages to the symptomatic MM. The asymptomatic stages are primarily identified by M-protein levels and their rate of progression to symptomatic MM. The first precursor, monoclonal gammopathy of undetermined significance (MGUS), has approximately a 1 in 100 chance of progression, while the second precursor stage, smoldering myeloma (SM), has a 1 in 10 chance. Genome-wide studies have identified several characteristic genetic mutations associated with each stage, although the drivers for the transition from MGUS to smoldering myeloma and symptomatic MM are unclear (**Figure 1.2**) (*1*,*6*).

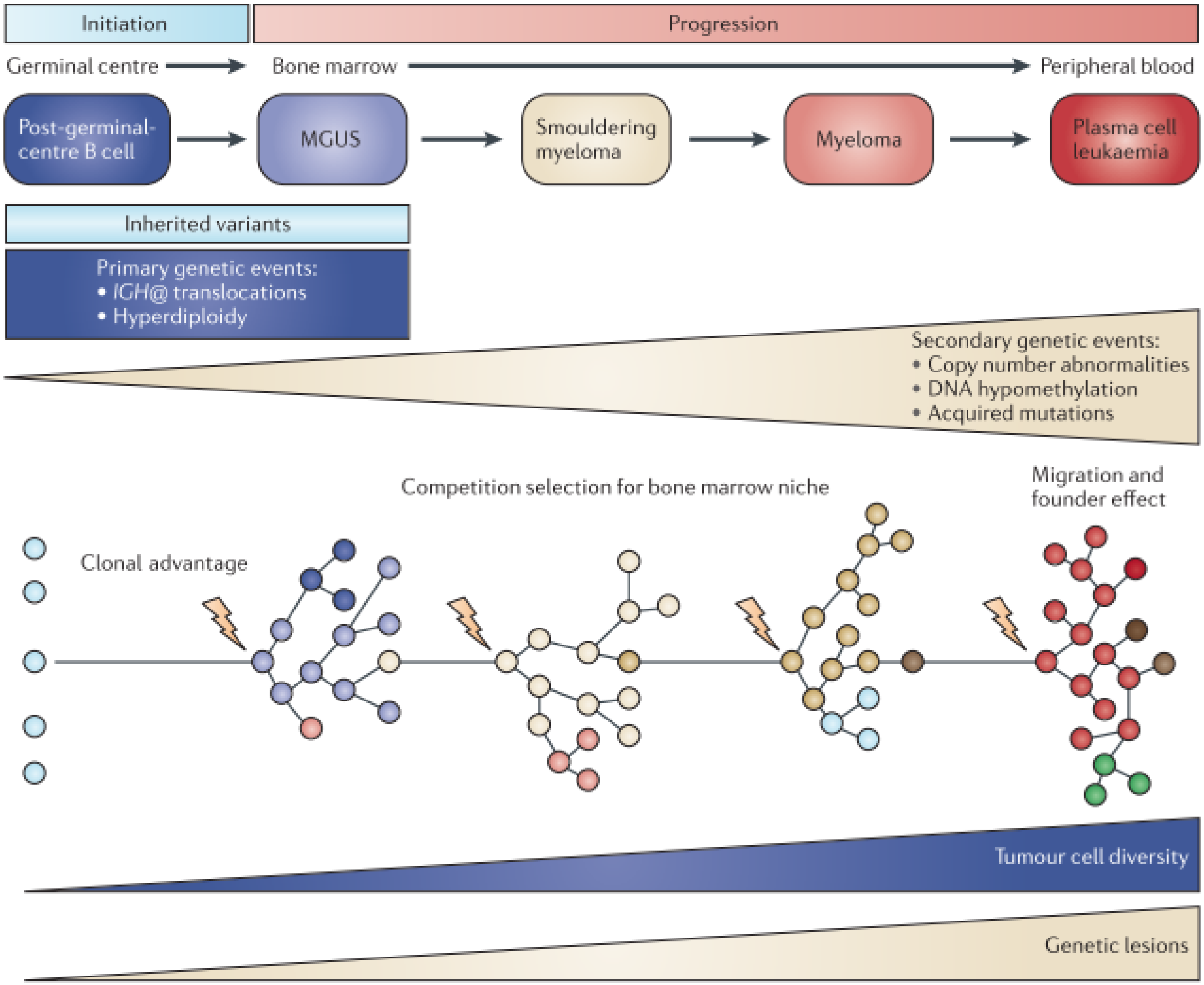

Figure 1.2: Summary of MM progression and genetic diversity. Reprinted from (6).

As noted in **Figure 1.2**, MM is characterized by clonal heterogeneity and high inter- and intra-lesion genetic diversity. This diversity is driven partly by the underlying B-cell maturation process. Immature B-cells are first differentiated from clonal progenitor cells in the hematopoietic niches in the BM. In pro- and pre- B-cell stages, cells undergo recombination of genes within the variable heavy and light chain loci. This process is known as VDJ recombination, due to the involvement of the variable (V), diversity (D), and joining (J) genes, and is central to the generation of antigen recognition. Self-reactive B-cells may undergo receptor editing, wherein secondary rearrangement of light chain variable regions generate antigen receptors with altered specificity. Failure to complete the maturation phase due to continued self-reactivity or other causes may also result in apoptosis *via* clonal deletion.

At this stage, immature B-cells leave the BM and are activated by antigen recognition and the presence of thymus dependent or independent co-stimulation. Activated B-cells migrate to the germinal centers of lymph nodes and undergo somatic hypermutation and class switch recombination to develop specificity to the target antigen (**Figure 1.3**). Both processes are mediated by the generation of double strand DNA breaks. These breaks are mostly repaired locally, but may be joined to breaks at other sites in the genome. These errors result in aberrant chromosomal translocations, which are considered as a genetic hallmark of myeloma. As a result of these affinity maturation processes and subsequent maturation to the high affinity plasma cell stage, B-cells encounter the potential of significant genetic hits that contribute to subclonal heterogeneity.

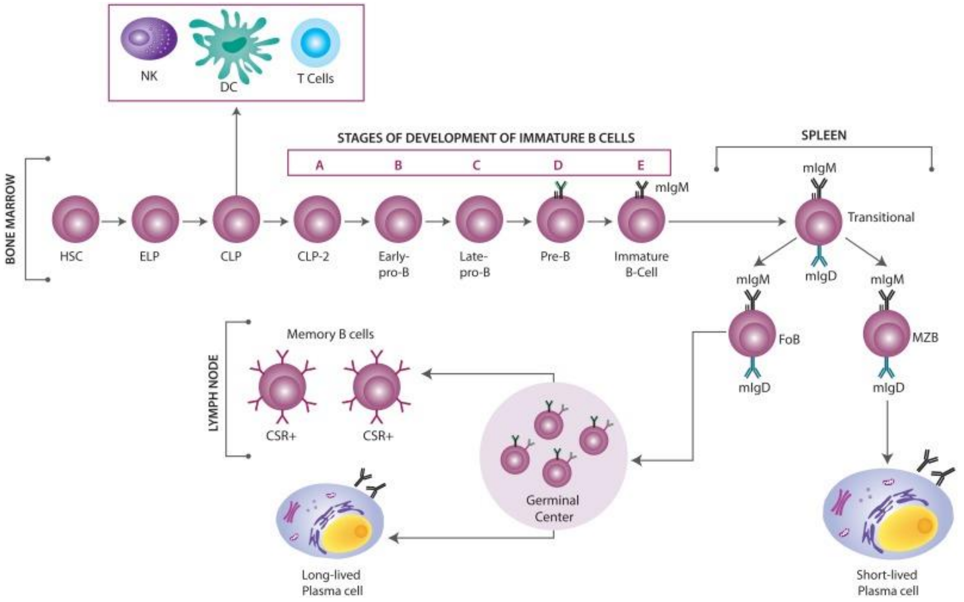

Figure 1.3: Summary of B cell maturation pathways and terminally differentiated states. NK, natural killer; DC, dendritic cell; HSC, hematopoietic stem cell; ELP, early lymphoid progenitor;

CLP, common lymphoid progenitor; CSR, class switch recombination; MZB, marginal zone B cells. Reprinted from (*7*).

Although the etiology of MM is currently unknown, general hallmarks of the disease include the upregulation of proliferation and cell survival genes, especially in the RAS/MAPK/ERK pathway, immortalization of plasma cells through abnormal plasma cell differentiation and resistance to apoptosis *via* mutations to the P13K/AKT pathways, and the upregulation of the NF-κB pathway (*6*). The primary aberrant chromosomal translocations, which have been recognized primary drivers for nearly 50% of all myeloma-related events, are the *t*(4; 14), *t*(11; 14), *t*(14; 16), and *t*(14; 20) (*8*). Detection of any of these translocations by cytogenetic assays is correlated to poor prognosis. Additionally, due to the presence of the transitory, asymptomatic MGUS and SM stages, myeloma plasma cells also undergo additional mutations and epigenetic changes that contribute to significant spatiotemporal heterogeneity within individual nascent BM sites.

1.2.2 *Interaction between myeloma cells and their BM niche is critical to progression and survival*

The tumor microenvironment has been increasingly linked to a cancer's aggressiveness and response to therapy (*9,10*). These observations are especially true for MM, where residence in the BM niche protects and promotes the myeloma plasma cell's immortalization and transformation. Due to the outsize role of the BM niche on myeloma pathogenesis, it is important to understand the complex cellular and structural characteristics of the BM, and their influence on therapeutic response and myeloma disease progression.

The BM is localized within axial and long bones (*11*). Bones have external cortical bone, which is composed of dense and osseous bone tissue. Cortical bone is organized into concentric circles called osteons, with each circular unit made of collagen and calcified extracellular matrix (ECM). Nerves, lymphatics, and blood vessels run through the middle of the osteon in the central canal, with orthogonal, branching vessels to supply surrounding tissue. Spongy, cancellous bone lines the interior of cortical bone, consisting of lattice-like trabecular bone. Sites within trabeculae are primarily linked to hematopoietic activity. **Figure 1.4** summarizes the bone structure and tissue compartments (*12*).

1.2.2.1 Adipose Marrow

The BM is composed, primarily, of adipose, yellow marrow and hematopoietic, red marrow. In humans, the adipose marrow constitutes the diaphysis of the long bones. This marrow adipose tissue (MAT) can be either constitutive or regulated, and provide endocrine and paracrine control of skeletal remodeling and hematopoiesis (*12,13*). The regulated MAT is concentrated in single adipocyte depots in the proximal femur and vertebrae close to hematopoietic niches. Regulated MAT expression changes dynamically with external and physiological stresses, including cold shock, estrogen levels, and age. By contrast, the constitutive MAT is concentrated in large depots and provide the characteristic yellow marrow phenotype. Constitutive MAT levels remain relatively stable in response to external drivers, but increases primarily with age and follows a spatial gradient from distal tibia and caudal vertebrae to more proximal vertebrae (*14*).

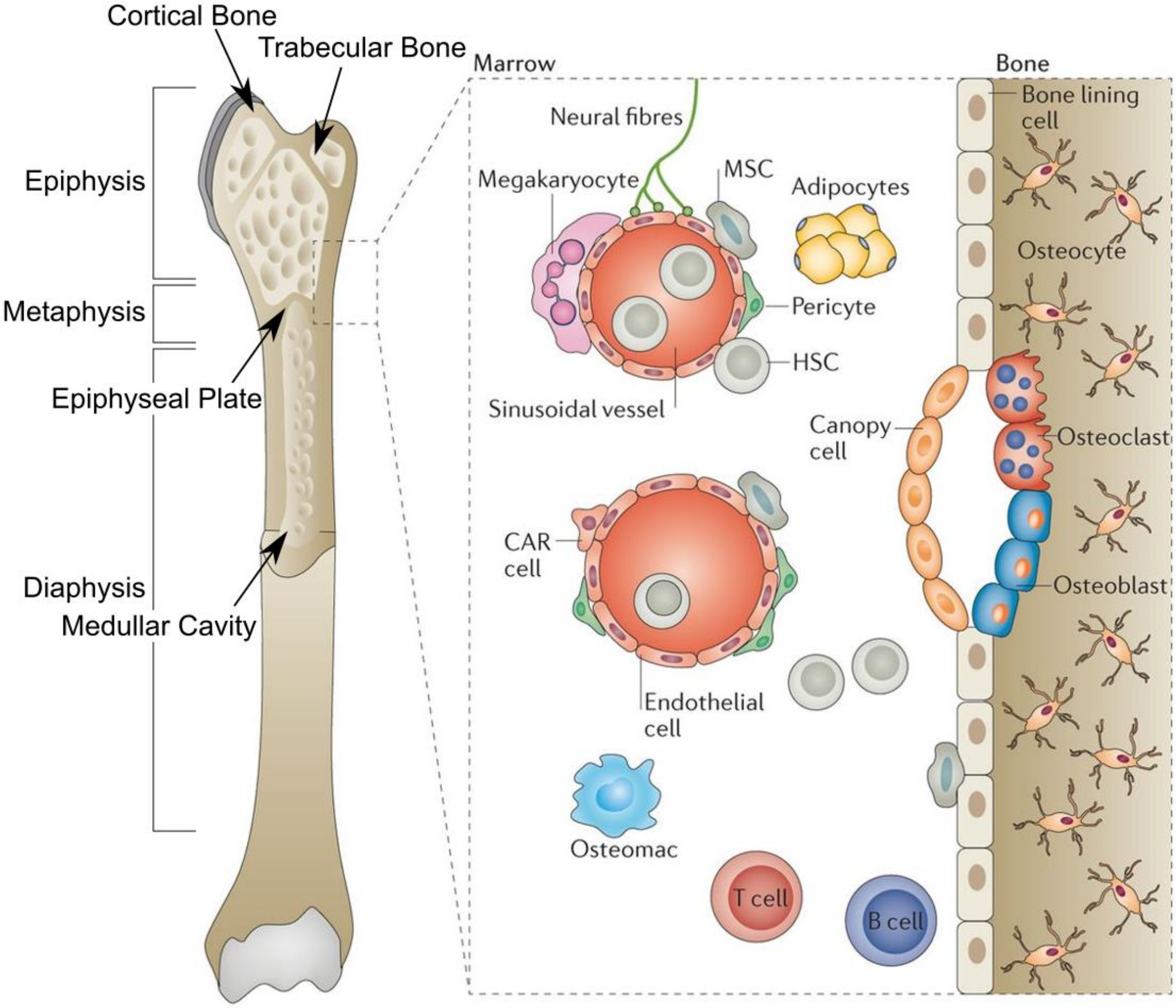

Figure 1.4: Summary of BM physiology and cellular components. MSC, mesenchymal stem cells; HSC, hematopoietic stem cells; CAR cell, CXCL2 abundant reticular cell. Adapted and reprinted from (*12*).

The role of MAT in regulating hematopoiesis is controversial in the literature (*15*). Generally, there is an inverse correlation between MAT levels and bone mass in both clinical and preclinical studies (*16,17*), although regions with high constitutive MAT may be better protected against bone loss (*18*). This association is also generally extended to the relationship between hematopoietic marrow cellularity and MAT deposits. The inverse relationship may be driven by competition for space within the BM cavity between adipocytes and hematopoietic cells. This hypothesis is consistent with the observation that implantation of hematopoietic stem cells (HSCs) and adipocyte progenitors result in reductions in overall HSC populations following irradiation, at least in part due to expansion of the MAT (*19*). By contrast, other studies have found a positive impact for MAT on hematopoietic activity in the marrow. In caudal vertebrae, for instance, secretion of stem cell factor (c-kit) by marrow adipocytes is critical for maintenance of hematopoietic cells (*20*). Additionally, adiponectin secretion is linked to improved HSC activation and recovery following irradiation (*21*). Finally, regeneration of erythroid progenitors and granulocytes in leukemia is increased following MAT expansion with peroxisomal proliferator activated receptor-γ (PPAR-γ) agonists (*22*). These studies indicate the complexity and heterogeneity in the observed interactions between marrow adipocytes and hematopoietic cells.

MAT performs an important role in regulating MM through both direct and indirect mechanisms. Due to fatty acid lipotoxicity, adipocytes have a well-known inhibitory effect on osteoblast proliferation (*23*). Additionally, secretion of CXCR2-activating chemokines by marrow adipocytes may accelerate osteoclast maturation (*24*). Both of these mechanisms indirectly assist in myeloma tumor proliferation by enhancing osteolysis and tumor cell escape from the intramedullary space. MAT also produces several tumor-promoting growth factors, including interleukin-6 (IL-6), tumor necrosis factor-α (TNFα), and insulin-like growth factor-1 (IGF-1), which provide significant endocrine signaling leading to cell migration, resistance, and proliferation pathways (*25*). Activation of the MAPK/ERK and Akt pathways by TNFα, for instance, stimulates IL-6 production and autocrine signaling in MM cells in a feedforward loop, which enhances cell proliferation and survival (*26,27*). Additionally, fatty acid secretion by marrow adipocytes provides an energy source and serves potentially as an antigen for inducing tumor-driving mutations during the MGUS state (*27,28*).

As with the complex and contradictory relationship exhibited between MAT and hematopoietic tissue, however, there is also significant evidence of inhibitory behavior by the MAT on MM. Lipid secretions modulate autophagy signaling, which reduce apoptosis from unfolded proteins in either positive or inhibitory roles (*25*). Furthermore, obesity may provide high-energy lipids and signaling that translates to poor prognosis due to increased drug resistance. However, severely obese or morbidly obese patients in one study (*n* = 1087) were found to respond more strongly to melphalan therapy, resulting in improved progression-free and overall survival rates relative to normal and overweight patients (*29*). Furthermore, adipokines, such as adiponectin and leptin, also have an impact on MM cell survival. Adiponectin is an anti-inflammatory cytokine secreted primarily by adipocytes, but also by osteoblasts and BM mesenchymal stem cells (MSCs). Adiponectin expression is decreased in obesity, cardiovascular disease, and myeloma (*30*). Adiponectin inhibits MM proliferation through the activation of the protein kinase-A/AMP-activated kinase pathways, resulting in increased cell death (*31*). On the other hand, leptin expression increases autophagy response and suppression of apoptosis in melphalan-treated MM cells. Understanding the role of individual signaling molecules secreted by adipocytes in the MAT and external adipose tissue can assist in developing new therapeutic strategies for MM treatment.

1.2.2.2 Hematopoietic Marrow

The hematopoietic (red) marrow primarily constitutes the epiphysis of long bones and spinal vertebrae and dominates temporally at early ages, before giving way to increasing constitutive MAT. Hematopoietic niches are predominantly localized within trabeculae in the perivascular space (*32*), and are supported by BM stroma, vasculature, and immune cells. These niches hold HSCs, which provide the regenerating stem cell basis for erythroid, myeloid, and lymphoid progenitors needed to support red and white blood cell production. Although HSCs circulate freely in and out of niches, there is evidence suggesting lineage restriction and localization of progenitors to specialized niches (*32,33*). For instance, B-cell progenitors are concentrated in CXCL2-expressing osteoblastic niches that are functionally different from perivascular niches that primarily maintain HSCs.

Current literature describes the hematopoietic niches as a complex array of MSC, endothelial cells, and hematopoietic progenitors that drive and regulate hematopoiesis (**Figure**

1.4) (*12*). The presence of MSCs and factors driving their differentiation into the osteoblast lineage are linked to HSC expansion and egress from the BM niche (*34*). Additionally, BM macrophages, or osteomacs, are critical for erythroid maturation and proliferation, while also facilitating BM homing and quiescence of HSCs (*35-37*). Indeed, treatment with granulocyte colony-stimulating factor was shown to increase differentiation, while reducing osteoblast and osteomac populations (*37*). Finally, a population of CXCL2 abundant reticular cells (CAR cells) promote osteoblastogenesis, perivascular space organization, and establishment of the microenvironment (*38,39*).

Micro-vascularization of the BM niches is regulated by the release of angiogenic factors by BM stromal cells (BMSCs), pericytes, and megakaryocytes located within the endosteam. As a result, the hematopoietic niches often comprise of a heterogeneous mixture of highly vascularized and hypoxic regions. The hypoxic regions generally house the quiescent HSCs and progenitors, while more prolific and differentiating cells are localized within the vascularized regions (*40*). The hypoxic microenvironment is maintained by the expression of the hypoxia-inducible factor-1α (HIF-1α) and its impact on HSC differentiation. HIF-1α is normally degraded soon after folding under normoxic conditions by hydroxylating enzymes and the proteasome complex (*41*). Under hypoxic conditions, HIF-1α translocates to the nucleus where it upregulates several glycolytic and pentose phosphate pathway related genes (*42*). As a result of this upregulation, oxidative phosphorylation is suppressed, allowing HSCs to tolerate oxidative stress and maintain quiescence. These conditions, in combination with the immune tolerance induced by large numbers of immune suppressor cells, result in the BM hematopoietic niches becoming attractive sites for tumor metastases or generation (*43*).

1.2.2.3 Bidirectional communication between MM and BM niches

Myeloma cell proliferation and survival is greatly facilitated by the conditions in the BM niches. The hypoxic environment may play a significant role in the selection of the tumorigenic genes and maintenance of the cancer cell stem-like behavior for drug resistance. Additionally, neovascularization is increased through HIF-1α activation of strong angiogenic proteins, including the vascular endothelial growth factor-A (VEGF-A) (*44*). Myeloma cells also generate a feed-forward loop that support and accelerate tumor cell proliferation. Production of the receptor activator of NF-κb ligand (RANKL) by osteoblasts and tumor cells and subsequent stimulation of RANK on pre-osteoblasts results in increases in osteoclast number and activity. This, in turn, results in increased myeloma tumor cell proliferation through the release of transforming growth factor-β (TGFβ), insulin-like growth factors (IGFs), and calcium following bone resorption (**Figure 1.5**) (*45*). Additionally, myeloma cells release Dickkopf-1 (DKK-1) in phenotypically mature MM cells and soluble Frizzled-related proteins (sFRPs) in plasmablastic states to inhibit BMSC differentiation for osteoblastogenesis (*46*). These proteins are antagonists to the Wnt signaling pathway, resulting in the increased production of osteoprotegerin and RANKL and subsequent osteoclastogenesis (*47*). Finally, production of chemokines and cytokines, particularly within in the CXCL12-CXCR4 signaling axis, integrins, and adhesion molecules by BMSCs and osteoblasts may be linked to improved tumor cell homing and engraftment within the BM niche.

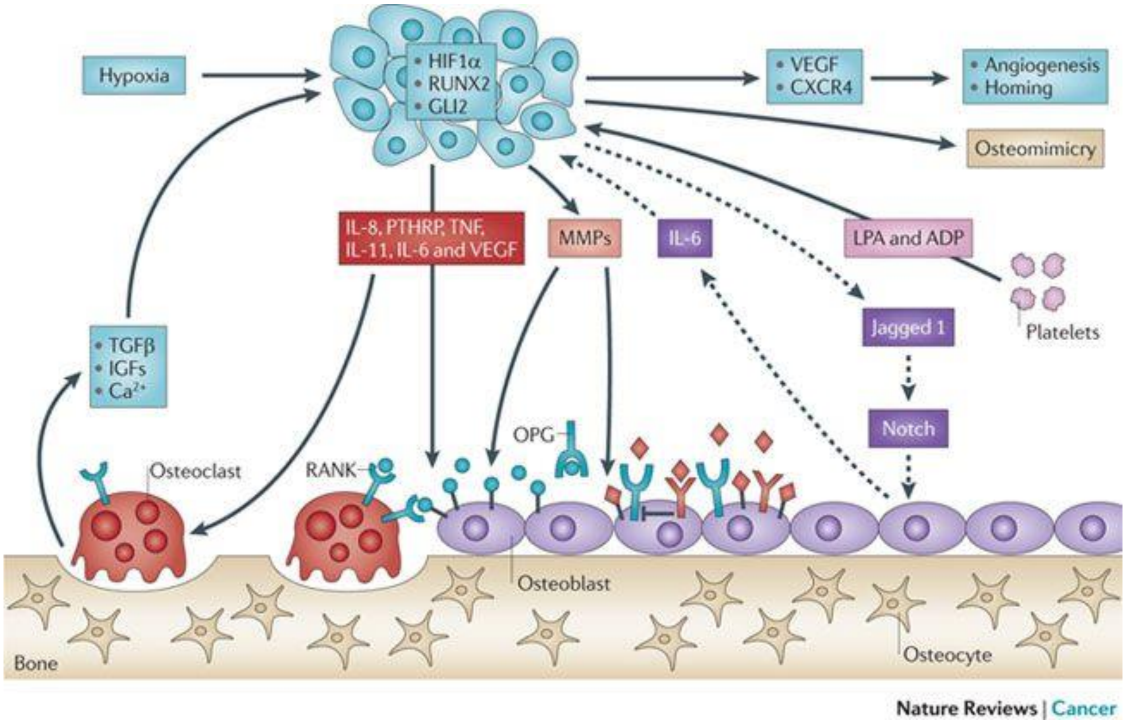

Figure 1.5: Summary of the feed-forward loop between tumors and osteolysis, through direct (solid arrows) and indirect (dotted arrows) means. (MMPs, matrix metalloproteinases; PTHRP, parathyroid hormone-related protein). MMP2s cleave membrane-bound RANKL (blue balls on the surface of osteoblasts) or epidermal growth factor-like proteins (red diamonds), resulting in an increased osteoclastogenesis *via* a higher ratio of RANKL to osteoprotegerin. Reprinted from (*45*).

Interactions with BMSCs provide critical adhesion and drug resistance, through cell adhesion mediated drug resistance (CAM-DR) pathways. In the presence of myeloma tumor cells, BMSCs produce several growth and survival proteins, including IL-6, IGF-1, CXCL12 (also known as stromal cell-derived factor-1 (SDF-1)), VEGF, and RANKL (*48*). Production of these cytokines is primarily driven by the overexpression of the bidirectional very-late integrin-4 (VLA-4; also known as $\alpha_4\beta_1$) on the surface of the myeloma cells. Expression and activation of VLA-4 is driven by autocrine signaling *via* myeloma cell-derived macrophage inflammatory protein-1α (MIP-1α) and VLA-4 binding with vascular cell adhesion molecule-1 (VCAM-1) and fibronectin on BMSCs (*49*). Importantly, VLA-4 is implicated in various myeloma pathogenic behaviors, including tumor adhesion, survival, proliferation, and drug resistance (*50,51*).

As described in this overview, myeloma pathogenesis is affected significantly by the BM niche. Hypoxia, coupled with favorable stromal support and immunosuppressive environment, provides an attractive, supportive structure for metastatic cancers, including MM. As a result, the development of stronger understanding of myeloma cell interactions at both intercellular and environmental levels are critical for improving therapeutic strategies.

1.2.3 MM treatment strategies induce significant changes in BM-resident cells and affect the BM microenvironment

Therapeutic strategies for MM have advanced significantly in the past two decades, resulting in substantial improvements in survival rates and patient quality of life. These pharmaceutical agents target a combination of intracellular pathogenic processes in myeloma cells and the surrounding environment. This section provides an overview of the literature on clinical MM therapies and their intracellular and extracellular effects.

Clinical stratification and initial treatment plans are predicated on transplant eligibility and risk stratification (*52*). The latter is determined using a combination of factors, including age, disease stage, and renal function, with further refinement for overall outcome estimation using the cytogenetic type (*53*). Based on these outcome estimates, a patient is stratified into standard, intermediate, and high risk strata. In newly diagnosed transplant-eligible patients, autologous stem cell transplantation (ASCT) of the hematopoietic marrow is performed following induction with two- or three-drug combination and high dose melphalan conditioning. By contrast, elderly, transplant-ineligible patients receive combination therapy followed by single-agent maintenance. The current treatment algorithm for each risk strata and transplant eligibility is summarized in **Figure 1.6**.

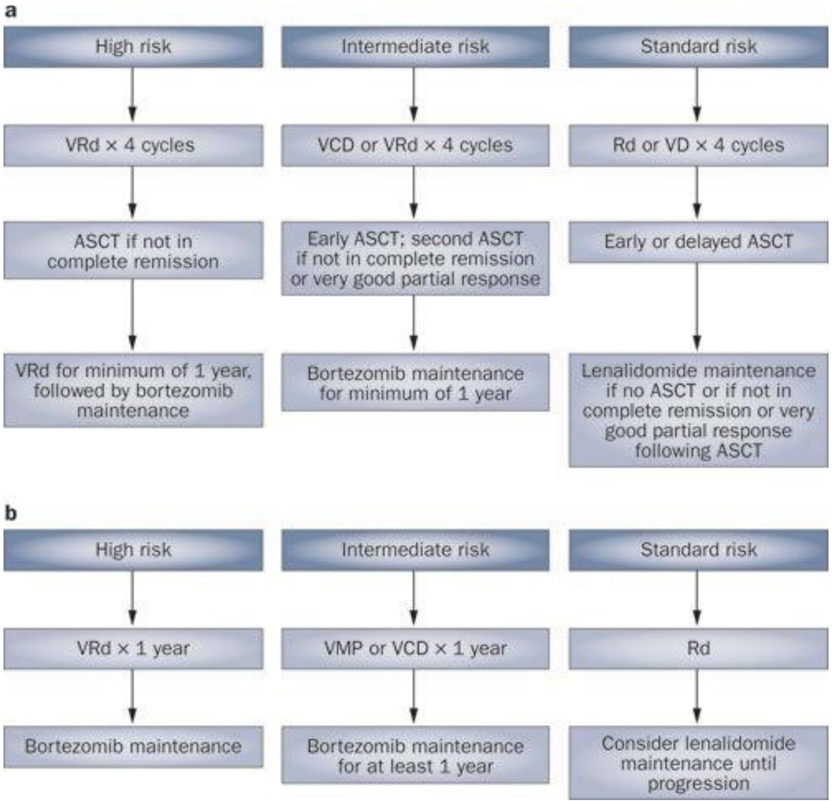

Figure 1.6: Treatment strategy for risk strata and transplant eligibility in newly diagnosed MM patients. (a) Approach in transplant-eligible patients. (B) Approach in elderly, transplant-ineligible patients. VD, bortezomib-dexamethasone; VCD, bortezomib-cyclophosphamide-dexamethasone; VMP, bortezomib-melphalan-predinisone; VRd, bortezomib-lenalidomide-dexamethasone. Reprinted from (*52*).

As noted in **Figure 1.6**, the majority of combination therapies involve the proteasome inhibitor bortezomib. Indeed, the approval of bortezomib for clinical use and subsequent combinations with immunomodulatory drugs (IMiDs) is linked to the improvements in overall survival seen in the past decade. A decreasing subset of induction combinations use the DNA alkylator melphalan as the headlining chemotherapeutic, due to relatively poorer progression-free survival, overall survival, and higher toxicities. Melphalan-centered combination therapies are instead predominantly used in relapsed and multi-drug refractory scenarios. For each of these agents, therapeutic efficacy is derived on effecting changes in the targeted myeloma cellular processes and the supporting BM niches.

1.2.3.1 Bortezomib

Bortezomib (Velcade, Takeda Pharmaceutical, Inc.) is a small molecule, dipeptide boronic acid analog. The primary mechanism of action for bortezomib is the reversible binding of the 26S proteasome subunit, triggering apoptosis through the unfolded protein response. Specifically, bortezomib has high affinity for the β5 subunit, which confers chymotrypsin-like functionality. The dipeptide groups form an anti-parallel β sheet conformation *via* hydrogen bonding to conserved amino acid residues in the β5 subunit. The boronic acid moiety forms a reversible stable adduct with the catalytic site, resulting in the complete inhibition of the chymotryptic subunit and partial inhibition of the tryptic and caspase-like subunits (*54*).

The downstream mechanism of action for bortezomib is based on several pathways. Initially, the primary mechanism was thought to be through the NF-κB pathway. NF-κB is an oncogenic transcription factor that translocates to the nucleus upon proteasomal degradation of the inhibiting I-κB (*55*). Prevention of proteasomal degradation would result in NF-κB remaining in its inactive complex. However, several studies showed that this effect was cell dependent, since NF-κB was activated through non-proteasomal degradation of I-κB in peripheral blood mononuclear cells (*56*). As a result, it is unlikely that the inhibition of the NF-κB pathway is the main mechanism of action.

Instead, bortezomib induces apoptosis through a combination of intrinsic and extrinsic pathways, and the activation of endoplasmic reticulum (ER) stress. In the intrinsic pathway, the apoptosis regulator Bax accumulates in the cytosol and translocates to the mitochondria, resulting in the release of cytochrome C and subsequent activation of caspase-9 (*57*). Inhibition of proteasomal degradation of the p53 tumor suppressor also results in p53-mediated apoptosis. The extrinsic pathway involves the downstream increases in c-Jun N-terminal kinase activity and death-inducing receptors Fas and DR5, which enhances caspase-8 activation (*58*). Finally, ER stress is induced by the buildup of misfolded proteins, which triggers apoptotic unfolded protein response and caspase-2 mediated cell death (*59*). The pathways and their components are shown in **Figure 1.7**.

Bortezomib therapy also significantly affects the surrounding BM niche. As mentioned in Section 1.2.2.3, MM engages supporting BMSCs, osteoclasts, and osteoblasts through a vicious feed-forward loop that causes increasing osteolytic activity, neo-angiogenesis, and drug resistance. Bortezomib promotes osteoclast apoptosis through the inhibition of p38 mitogen-activated protein kinase (MAPK), activator protein-1, and NF-κB pathways (*60*). Osteoblast differentiation from osteoblast progenitors and MSCs is also induced through stabilization of β-catenin, and accumulation of β-catenin and the transcription factor Runx2/Cbfa1 in the nucleus (*61*). Furthermore, bortezomib reduces adhesion to BMSCs through the inhibition of the MAPK pathway, which contributes to a reduction in adhesion-mediated drug resistance (*62*). Finally, angiogenesis by BMSCs and other endothelial cells is reduced through down-regulation of VEGF, IL-6, and other angiogenesis-inducing factors (*63*).

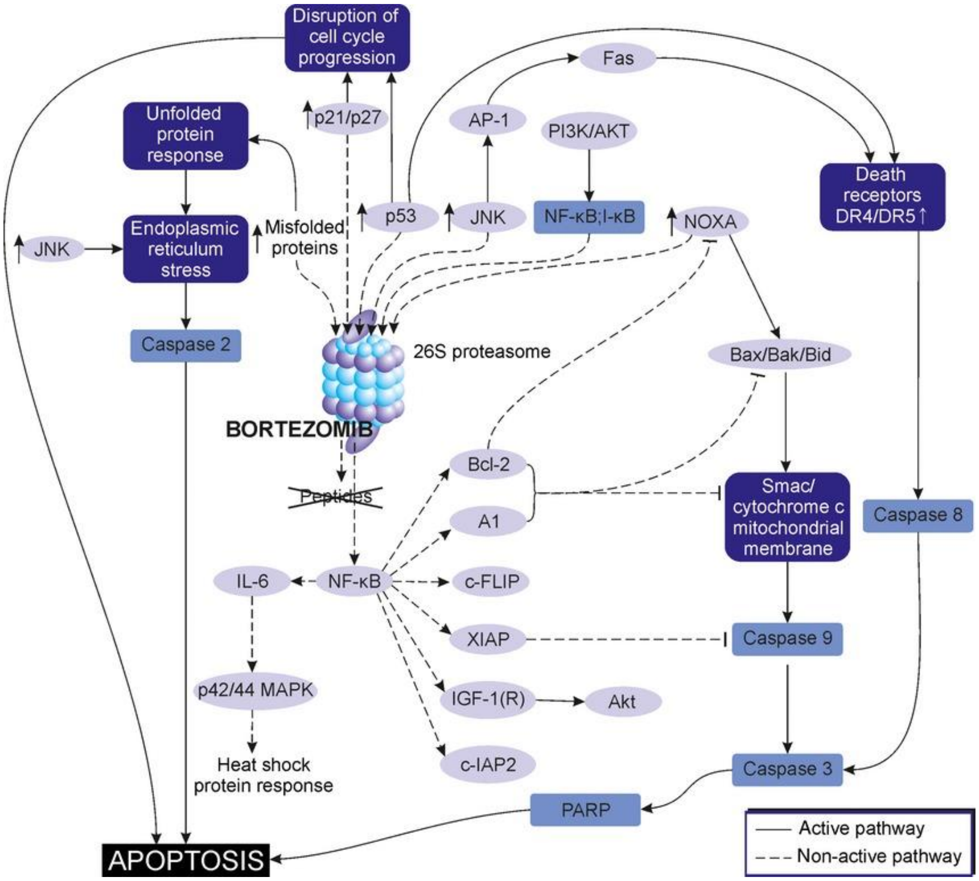

Figure 1.7: Summary of apoptotic pathways induced by bortezomib-mediated inhibition of the catalytic 26S proteasome. Reprinted from (*55*).

The success of bortezomib and bortezomib-driven combination therapies in MM clinical care has resulted in significant interest in novel, second- and third-generation proteasome inhibitors. For instance, the second-generation proteasome inhibitor carfilzomib (Krypolis, Onyx Pharmaceuticals) has recently been approved for use in MM clinical care in bortezomib-refractory disease and frontline treatment (*64,65*). Carfilzomib is an irreversibly binding epoxyketone that also inhibits the chymotryptic β5 subunit (*66*). The development of these agents is needed to overcome the challenges of off-target toxicity and cell line-dependent resistance to bortezomib, which is primarily mediated by mutations in the proteasome subunit β5 gene and increases in proteasomal capacity (*67,68*).

1.2.3.2 Immunomodulatory drugs (IMiDs)

BM niches have immunosuppressive environments that provide a favorable area for myeloma tumors, especially following the expansion of myeloid derived suppressor cells (MDSCs) and regulatory T (Treg) cells. Both MDSCs and Treg levels are increased in the tumor microenvironment and in the peripheral blood (*69*). MDSCs and myeloma cells have a bidirectional relationship (*70*). MDSCs induce myeloma tumor growth through suppression of T-cell mediated immunity, while myeloma cells promote MDSC differentiation from healthy peripheral blood mononuclear cells. Tumor-induced MDSCs may also contribute to tumor-associated osteolysis due to an increased potential to differentiate into mature, functional osteoclasts relative to non-tumor controls (*69*).

Tregs are a subset of $CD4^+$ T cells that suppress antigen-presenting cells and effector T cells through direct binding or release of IL-10 and TGF-β (*69*). Increases in Treg levels in the tumor microenvironment and peripheral blood are correlated to poor prognosis. However, the direct mechanism of myeloma induction of Tregs is not well understood, although *in vitro* studies suggest direct induction in an antigen-presenting cell independent way (*71*). Regardless, the inhibition of excess immunosuppression by MDSCs, Tregs, and other tumor-related immune cells is critical for improving outcomes.

In MM clinical care, this strategy is primarily implemented using immunomodulatory drugs (IMiDs), often in combination with a proteasome inhibitor or melphalan, and a corticosteroid (e.g., dexamethasone, prednisone). IMiDs currently used for MM are the first-generation thalidomide and second-generation lenalidomide (Revlimid, Celgene Corporation) and pomalidomide (Pomalyst, Celgene Corporation). While the exact mechanism of action is unclear, IMiDs induce immunostimulation and MM cytotoxicity through several direct and indirect pathways. Specifically, second-generation IMiDs cause myeloma cell apoptosis through the up-regulation of the cell cycle arrest with $p21^{waf1}$, inhibition of NF-κb, and activation of caspase-8 (*72*).

IMiDs also disrupt the interaction between the myeloma cells and their surrounding microenvironment by downregulating adhesion, neo-angiogenesis, and the release of cytokines and growth factors (**Figure 1.8A**) (*73*). Thalidomide inhibits TNFα, resulting in the downregulation of cell surface adhesion molecules, including VLA-4, lymphocyte function-associated antigen-1 on plasma cells, and VCAM-1 and the intercellular adhesion molecule-1 (ICAM-1) on BMSCs (*74*). Thalidomide and the second-generation IMiDs also inhibit other inflammatory cytokines to varying degrees, although the contribution of this action towards curtailing MM activity is uncertain. Finally, IMiDs display anti-angiogenic behavior, by abrogating VEGF and basic fibroblast growth factor (βFGF) production through interference of PI3K/Akt pathway in both BMSCs and plasma cells (*75,76*).

In addition to disruption of the BM-myeloma environment, all IMiDs augment adaptive and innate immune system response to MM to some extent (**Figure 1.8B**), although there is conflicting evidence for mechanisms or the overall *in vivo* effect. IMiDs, particularly lenalidomide and pomalidomide, induce co-stimulation of partially activated $CD4^+$ and $CD8^+$ through increased production of IL-2 and interferon-γ (IFNγ) (*77*). The production of IL-2 also promotes natural killer (NK) cell proliferation, and the second-generation IMiDs also enhance antibody-dependent cellular cytotoxicity and the natural NK cell cytotoxic function (*78*). In Tregs, lenalidomide and pomalidomide reduce expression of the transcription factor FOXP3, and subsequently the population and function of the Tregs within the overall T cell population (*79*).

Despite these observed *in vitro* effects, the degree to which IMiDs affect immunosuppression, or general immunoparesis, is unknown. In part, this may be due to the use of the corticosteroid dexamethasone, which functions as an immunosuppressant. As a result, patients responding to combination therapies containing dexamethasone and an IMiD show a significant reduction in T and B lymphocytes, and NK cells. Additionally, Treg suppression *in vitro* does not fully translate to clinical results, where response to lenalidomide therapy correlated to a relative increase in the Treg population, relative to normal MM patients (*73*).

Furthermore, there is no significant inhibitory effect on the suppressive function of MDSCs by either bortezomib or lenalidomide, resulting in increased levels of MDSCs in both BM and peripheral blood of MM patients (*80*).

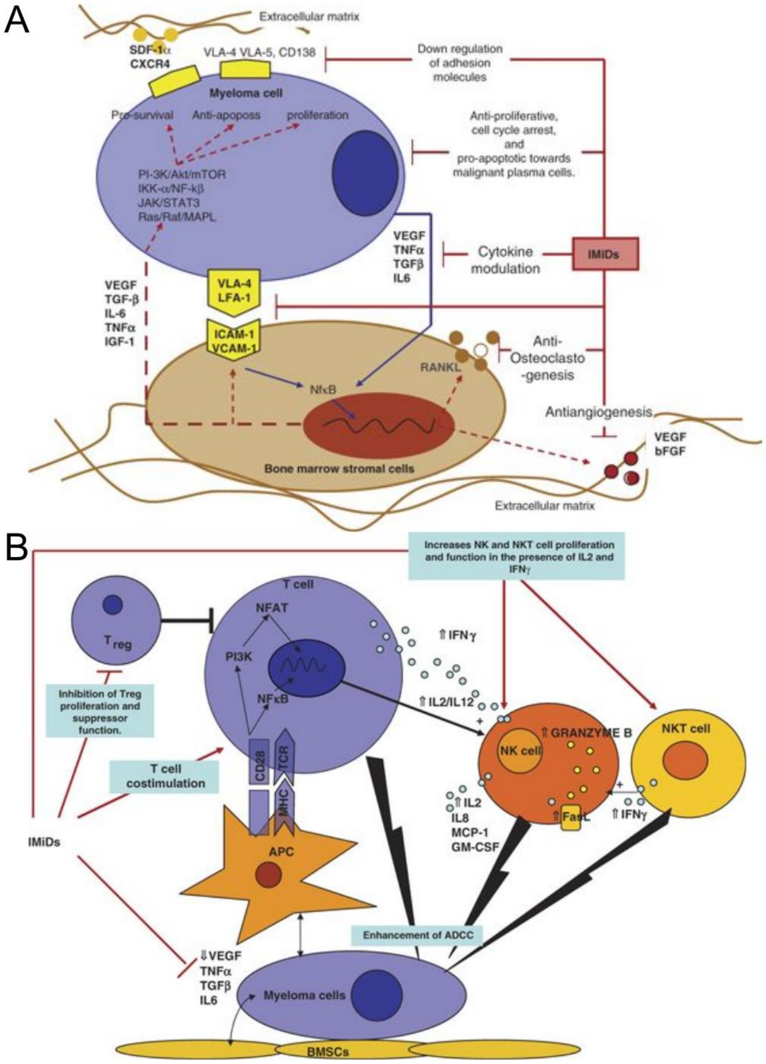

Figure 1.8: Summary of (A) microenvironment and (B) immune system effects induced by IMiDs. APC, antigen-presenting cell; NKT cell, NK cells with T lymphocyte markers and functionality; ADCC, antibody-dependent cellular cytotoxicity. Adapted and reprinted from (*73*).

Given the complex, environment dependent efficacy of IMiDs and their safety profiles, and the importance of modulating and reducing immunoparesis, there is a significant push in developing novel cancer immunotherapies, vaccines, and adoptive T cell transfer mechanisms. Work in engineering chimeric antigen receptor T cells, immune checkpoint antibodies, and cancer vaccines has shown considerable promise and potential clinical value. However, discussion of these technologies is beyond the scope of this review.

1.2.3.3 Melphalan

Melphalan (L-phenylalanine mustard) is one of the oldest chemotherapeutic agents still used to treat MM. Originally approved in 1962, melphalan is used in combination with bortezomib, corticosteroids, and IMiDs for elderly, transplant-ineligible patients and as a high-dose conditioning regimen prior to ASCT. Due to off-target toxicities and relatively poor overall survival rates compared to bortezomib-based therapies, melphalan-centered combinations are slowly being phased out in front-line care, although they are used in patients where bortezomib-based treatment is not feasible (*52*).

Melphalan induces cell death by alkylating DNA non-specifically and creating cross-linked adducts within the DNA. These adducts can result in deletions and strand breaks, eventually leading to downstream apoptosis through Bax activation and cytochrome c release (*81*). Melphalan may also contribute to the disruption of BM myeloma microenvironment by inhibiting IL-6 production in BMSCs and osteoblasts, thereby reducing MM autocrine signaling and recruiting inflammatory cells to the BM niche (*82,83*). Interestingly, melphalan has also been suggested to provide immunomodulatory effects in the BM microenvironment, by recruiting $CD8^+$ T cells and reducing Treg and MDSC populations (*84*).

1.2.4 Summary

MM is a highly clonal disease that is significantly influenced by its tumor microenvironment. Myeloma cells utilize bidirectional signaling with other cells in the BM milieu, including immune cells, BMSCs, osteoblasts, and osteoclasts, resulting in increased myeloma proliferation, survival, and drug resistance. Although current therapeutic regimens effect marked reductions in adhesion-mediated resistance, immunosuppression, vascularization, and tumor burden, MM remains an inherently incurable disease. Indeed, following relapse, each therapy cycle is successively shorter, resulting in increasing resistance to treatment regimens (*85*).

Resistance and relapse are driven by clonal evolution and selection of drug resistant cells, and adhesion-mediated activation of anti-apoptotic pathways (*86*). As a result, methods for identifying resistant phenotypes early are necessary for reducing off-target toxicities, improving patient quality of life, and affecting changes in the treatment strategy for mitigating increases in tumor burden.

1.3 Noninvasive imaging provides spatiotemporal sampling of MM staging

1.3.1 Introduction

Due to the inevitable relapse and emergence of refractory disease, it is necessary to assess response to therapy. As an immunoglobulin secreting disease, the traditional method for screening therapy response is by quantifying serum M-protein load, and, latterly, free light-chain content with the serum protein electrophoresis (SPEP) and the free light-chain (FLC) assay, respectively. Liquid biopsies sampled from BM tissue, typically from long bones or the pelvis, provide the percentage of plasma cells in the BM. This information, in combination with imaging data such as changes in number of lesions, BM architecture, and tumor metabolic activity, forms the basis for monitoring the treatment approach.

The SPEP assay is a mainstay for diagnosis and staging of MM and its asymptomatic precursor states. Using charged, size-dependent diffusion, SPEP assays identify the most common serum protein fractions. The presence of monoclonal (M) protein is detected as an intense band or spike in the γ-globulin fractions (*87*). Response to therapy is correlated to M-protein intensity, since M-protein production is linked to tumor burden. However, SPEP has a high detection limit, requiring more than 500-2000 mg/L in serum protein for analysis (*88*). In addition, approximately 15-20% of patients have non-secretory, light-chain, or oligo-secretory MM, which prevents the detection of intact immunoglobulins in the sera. Finally, due to the slow clearance rates of IgG antibodies (biological half-life, ~23 days), SPEP is not sensitive to rapid changes in tumor burden associated with therapy response (*89*).

To ameliorate some of these concerns, serum FLC assay is increasingly used in MM staging. In oligo-secretory and light-chain myeloma, M-protein is at low concentrations with primarily light chain present in the serum. Serum FLC is more rapidly responsive to changes in immunoglobulin production and secretion than standard SPEP or urine protein electrophoresis. However, in approximately 3% of initially diagnosed patients and patients that have received long-term treatment, there is little to no detectable secretion of intact or light-chain immunoglobulin (*90*).

Finally, liquid biopsies sampled at the site of myeloma lesions, typically with noninvasive imaging guidance, provide changes in total myeloma cells present within the biopsy. However, biopsies sample regions within a lesion and are hindered by both the inter- and intra-lesion spatial heterogeneity. Because of the clonal and spatial heterogeneity, whole-body noninvasive imaging is increasingly used in the diagnosis and staging of MM. Changes in BM tumor microenvironment translate to visible, quantifiable changes in imaging parameters. Therefore, this section addresses the major imaging technologies used in monitoring treatment response in MM.

1.3.2 Applications of PET/CT in assessing therapy response

Positron emission tomography (PET) is the workhorse technology for molecular imaging and treatment response assessment for clinical cancer care. In particular, [^{18}F]-fluorodeoxyglucose (FDG) is the primary contrast agent used for imaging due to its versatility and applicability for inflammatory diseases. In MM care, FDG-PET is used primarily in staging prognosis following treatment, but due to a combination of factors, it has limited sensitivity and specificity in intramedullary disease. To assess the role of FDG-PET and its pitfalls in managing MM care, it is necessary to understand the mechanism behind contrast generation, FDG uptake and retention biology, and promising alternate tracers.

1.3.2.1 Principles of image acquisition

PET is a functional imaging technique that detects and transforms radioactive decay into an image. The contrast agents used for PET are unstable, proton-rich nuclei that decay to the immediate lower atomic number, while keeping the mass number constant. There are two common methods for this decay. The first is *via* positron emission, where a proton decays to a neutron, positron (e^+), and neutrino (*v*) (**(1.1**). The other method is by electron capture, where the nucleus captures an orbital electron and converts a proton to a neutron, while releasing x-rays or gamma rays (**(1.2**). The two methods compete with one another, with positron emission dominant in low atomic number (Z) nuclei and electron capture more likely in higher Z nuclei.

$$ {}^{Z}_{A}M \rightarrow {}_{A-1}^{Z}D + e^{+} + \nu \tag{1.1}$$

$$ {}^{Z}_{A}M \rightarrow {}_{A-1}^{Z}D + \nu \tag{1.2}$$

The emitted positron has a very short lifetime. Upon encountering an electron, the positron and electron combine and annihilate, resulting in the generation of two 511 kilo-electronvolt (keV) γ-photons traveling in opposite, collinear directions. This process has several advantages that are harnessed for PET image generation. The first is that the generated photons have energies that are an order of magnitude higher than those of diagnostic x-rays, which reduces risk of attenuation by tissue and enhances external detection. More importantly, the collinear nature of the emission is detected at opposite ends within a timing window, resulting in coincidences that provide collimation without the need for physical collimators. As a result, PET offers highly sensitive imaging that translates to improvements in temporal resolution and image quality.

However, this coincidence detection is affected by unwanted coincidental sources, which significantly hamper the signal to noise ratio. These unwanted sources include scattered, random, and multiple coincidence events. Scattered events are caused by Compton scattering, where high energy radiation is deflected off nuclei in the radiation path, resulting in loss of energy. PET detectors have relatively poor energy resolution, resulting in the acceptance of different energies, and an incorrect localization of the annihilation event. In random occurrences, two γ-rays generated from different events are detected within the timing window. The rate of random coincidences is proportional to the amount of activity and the length of the timing window. Finally, multiple coincidences occur with the detection of three or more events within the timing window. The different types of coincidences, both true and accidental are summarized in **Figure 1.9**.

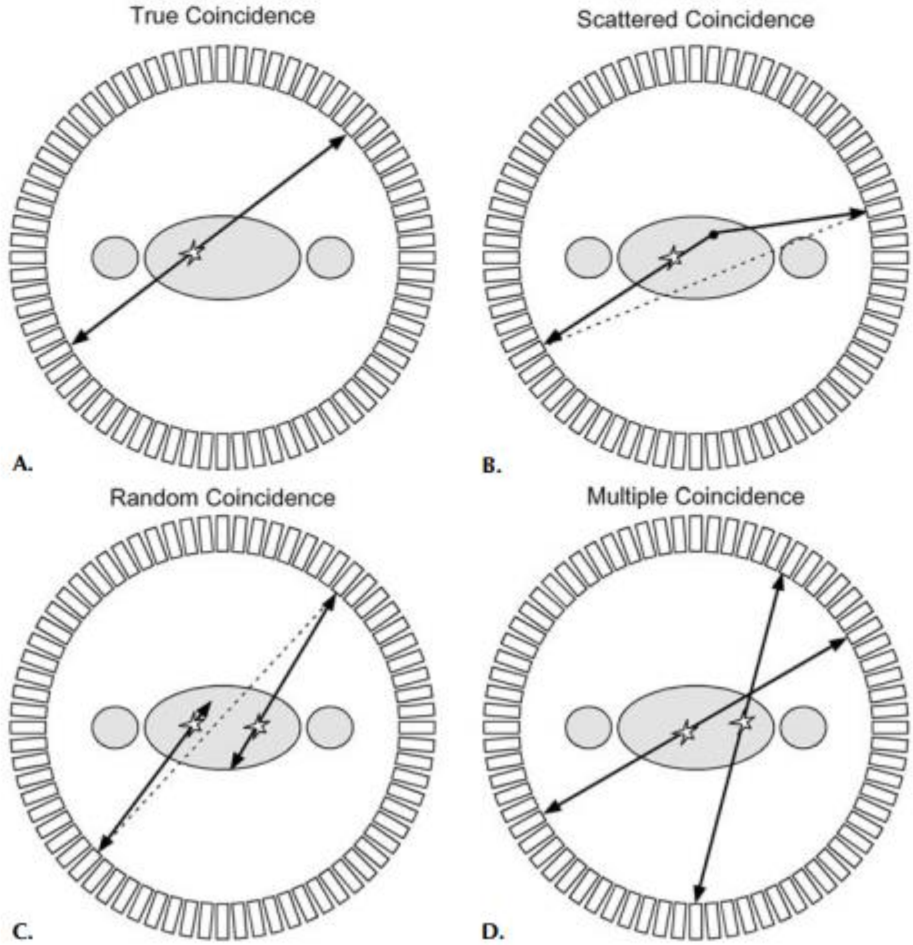

Figure 1.9: Summary of the types of possible coincidence events in a PET scanner following positron annihilation. Reprinted from (*91*).

The spatial resolution in PET is primarily affected by the positron decay itself, due to the combination of non-zero positron range and non-collinearity. Non-zero positron range stems from the distance traveled by the positron before it is annihilated. This energy is dependent on the emission energy, which is sampled from an exponential probability distribution bounded between zero and the maximum endpoint energy. The maximum endpoint energy is dependent on the difference in atomic mass between the parent and daughter atoms, as well as the excited state gamma emission. As a result, the positron range limits the maximum attainable spatial resolution in PET. In addition, the positron often has a non-zero momentum when annihilated, resulting in the generation of photons that are not traveling in exactly 180^o directions. The effect on spatial resolution by non-collinear photons is driven entirely by the distance between detectors. As a result, this effect is negligible in small animal PET imaging systems, but potentially significant in clinical systems.

Because of the use of coincidence events and the absence of physical collimation, PET possesses higher sensitivity than other imaging technologies. Additionally, scan time is minimized, leading to improvements in temporal resolution. The main disadvantage of PET is the poor spatial resolution relative to structural imaging modalities and single photon emission computed tomography. However, the combination of high sensitivity and temporal resolution make PET an attractive functional imaging technology for assessing aspects of metabolism and receptor densities.

1.3.2.2 Mechanisms of FDG contrast generation

FDG is the most commonly used radiotracer for PET imaging and accounts for over 95% of all radioactivity generated for medical imaging in the United States. It is synthesized by substituting ^{18}F for the hydroxyl group at the C-2 position in glucose. ^{18}F has a half-life of 109.7 minutes, and is generated with a cyclotron or linear accelerator. As a glucose analog, FDG probes glucose uptake for glycolysis, which is required for sustenance and upregulated in high energy tissue, proliferative diseases, and inflammation. Furthermore, glucose is linked to several metabolic pathways for energy production, nucleotide and amino acid synthesis, and signaling.

Glucose uptake is mediated by glucose transporter (GLUT) types 1, 3, or 4. Following uptake, glucose is phosphorylated and converted into glucose-6-phosphate by hexokinase, at which point it is either shunted towards glycolysis or nucleotide synthesis through the pentose phosphate pathway. The primary end product of glycolysis is pyruvate, which is translocated to the mitochondria where it enters the tricarboxylic acid (TCA) cycle and oxidative phosphorylation. In non-proliferative cells and normoxic tissue, oxidative phosphorylation is the dominant pathway following glycolysis for pyruvate, since it produces the most adenosine triphosphate (ATP) per glucose molecule. Thus, glucose and its products are linked to several tightly regulated metabolic pathways.

In cancer cells, however, oxidative phosphorylation is minimized, with the majority converted into lactate, as per the Warburg effect hypothesis (*92*). This observation implies the predominance of aerobic glycolysis in cancer cells, which increases glucose accessibility for generating precursors for fatty acids, nonessential amino acids, and nucleotides, which are critical for rapid growth and division. Thus, to support proliferative growth, cancer cells have upregulated GLUT proteins, particularly GLUT1, and hexokinase-2 to mediate glucose uptake and conversion to glucose-6-phosphate, respectively.

The upregulation of these proteins provide the impetus for FDG contrast generation. Following uptake, FDG is converted into FDG-6-phosphate, which is unable to progress in later glycolytic reactions or in the pentose phosphate pathway. Additionally, the hexokinase forward reaction is generally irreversible, except in select tissues including the liver, where the enzyme glucose-6-phosphatase convert glucose-6-phosphate back into glucose. Therefore, FDG uptake is irreversible and correlates to the exogenous glucose metabolism of the cell.

The irreversible nature of FDG uptake and the upregulation of aerobic glycolysis in tumors makes FDG an attractive contrast agent for imaging active tumors *in vivo*. Furthermore, since tumors remain mostly glucose-avid, apoptosis and reductions in tumor burden correlate to losses in FDG uptake. As a result, FDG-PET is one of the main imaging technologies for quantifying treatment response in most cancers.

In MM, however, FDG-PET is not as reliable as in most proliferative cancers. Indeed, FDG-PET has over 95% sensitivity in detecting extramedullary lesions, but approximately 60% sensitivity for intramedullary lesions (*93*). This discrepancy may be due to a combination of factors. First, intramedullary lesions are composed of largely hypoproliferative cells, in part due to the influence of the BM microenvironment. More importantly, MM tumors have inconsistent overexpression of hexokinase-2 and GLUT1, which reduces FDG uptake, even in untreated tumors. Additionally, uptake of FDG may be compromised by the presence of significant inflammation, since inflammatory cells are highly glucose-avid, thereby resulting in false positives. As a result, the most recent International Myeloma Working Group (IMWG) have deprioritized FDG-PET for diagnostic imaging for MM, although FDG-PET continues to be used for staging therapy response, especially in extramedullary lesions (*94*).

1.3.2.3 Alternate tracers

In recent years, there has been an increase in the development and validation of alternate radiotracers to probe other features of the myeloma pathogenesis. These probes are specific for overexpressed receptors, transporters, and pathways that are necessary for myeloma cell function and pathogenesis. The aim of this development is to provide complementary diagnostic information, and potential links to therapy efficacy since MM treatment induces significant shifts in BM environmental interaction and expression of critical pathways.

In addition to glucose uptake, there are several metabolic pathways with clinical significance in MM. Amino acid transport and fatty acid metabolism are two such pathways. The synthesis of nonessential amino acids is a vital strategy for all cancers, especially MM due to the continual overproduction of M-protein. Indeed, the system L amino acid transport protein family is overexpressed in MM, with high expression of the L-type amino acid transporter-1

(LAT1) linked to poor clinical prognosis and survival (*95*). LAT1 is a sodium-independent obligatory exchange transporter that mediates the transport of aromatic and branched amino acids. Amino acid uptake from these transporters takes part in intracellular signaling, regulation of the TCA cycle, protein synthesis, and several other processes. Thus, PET amino acid probes mostly study the uptake of amino acids and, therefore, expression of the amino acid transporter. The primary tracers studied for this application are tyrosine, methionine, and phenylalanine analogs (*96*). LAT1 imaging for MM using the phenylalaine analog 3,4-dihydroxy-6-[^{18}F]fluoro-L-phenylalanine (^{18}F-FDOPA) and its connection to melphalan therapy efficacy will be explored in this dissertation.

Fatty acid metabolism is also upregulated in MM. In particular, exogenous acetate uptake is increased, due to its role in the biosynthesis of nucleotides, amino acids, and cell membrane components (*97*). Acetate is ligated with coenzyme-A (CoA) to form Acetyl-CoA, a highly versatile molecule with several end products. Acetyl-CoA is a precursor for lipid synthesis through fatty acid synthases, which are overexpressed in myeloma cells. Our lab has previously demonstrated the utility of ^{11}C-acetate for monitoring response to myeloma therapy (*98*). Pharmacological inhibition of fatty acid synthase activity induces significant toxicity in myeloma cells *in vitro* and *in vivo*. In patients, ^{11}C-acetate uptake has been correlated to systemic tumor burden and provided higher sensitivity for detecting intramedullary diffuse and focal lesions compared to FDG-PET (*99*).

In addition to imaging intracellular metabolism, expression of surface markers can be assessed using PET. For instance, we have demonstrated longitudinal imaging of VLA-4 expression in both intramedullary and extramedullary lesions *in vivo*, using a ^{64}Cu-labeled peptidomimetic that is highly specific for the activated conformation of VLA-4 (*100*). VLA-4 expression is linked to myeloma cell survival, adhesion, and proliferation through bidirectional signaling with VCAM-1 and fibronectin on the surface of BMSCs. Crucially, VLA-4 is a key mediator of CAM-DR, and may be used for monitoring therapy response.

1.3.3 Magnetic resonance imaging is increasingly applied to MM diagnosis and staging

Magnetic resonance imaging (MRI) is a noninvasive structural imaging method that provides strong soft tissue contrast and resolution. The use of MRI in MM care has increased significantly over the past decade due to its ability to resolve diffuse and focal intramedullary lesions. Due to the complimentary potential of multiple endogenous and exogenous contrast mechanisms, MRI is an attractive technology for enhanced detection and quantitative analysis of lesion changes following therapy.

1.3.3.1 Overview of MRI contrast mechanisms

MRI signal is generated through changes in the magnetic spins of hydrogen molecules in a strong magnetic field. Hydrogen spins are oriented in the direction of the axis of the magnetic field (B_0) induced by the scanner. The exposure of the magnetic moment in the field induces angular momentum and precession along the axis of B_0 at the Larmor frequency, which is dependent on the gyromagnetic ratio and the strength of the magnetic field. Thus, at equilibrium, the z-directional component of the spin is aligned with B_0, while the x- and y-directional components are incoherent and average to zero.

To perturb this equilibrium, radiofrequency (RF) energy is added to the system using RF coils. RF pulses cause the magnetic moment to become aligned off-axis. The recovery of the moment to equilibrium is the primary source of contrast in an MR scan. There are two primary contrast mechanisms. Longitudinal, spin-lattice, relaxation is driven by the recovery of the z-directional magnetic moment (M_z). M_z inversion by 180^o is followed by recovery towards the direction of B_0. This process follows an exponential curve, with the characteristic relaxation time given by T1 (**(1.3**). By contrast, transverse, spin-spin, relaxation is driven by the loss of coherence in xy-plane. The introduction of a 90^o RF pulse induces a non-zero average M_{xy} component, which decays back to zero with magnetic fluctuations and transfer of energy between magnetic moments. The characteristic relaxation time for transverse relaxation is given by T2 (**(1.4**).

$$M_z(t) = M_0(1 - \exp(-t/T_1)) \tag{1.3}$$

$$M_{xy}(t) = M_0 \exp(-t/T_2) \tag{1.4}$$

Localization of the MR signal to specific voxels for spatial characterization of T1 and T2 decay is performed using external electromagnets, which generate a gradient field in all directions in Cartesian space. Gradient pulses are combined with the RF pulse sequences to create a spatial distribution of transverse magnetization that is first structured as 2D/3D Fourier space, and then reconstructed into an MR image by taking the inverse Fourier transform. In general, most MR images are the magnitude component of the Fourier space. Low- and high-frequency components of the Fourier space provide the underlying contrast and edge maps, respectively.

The potential library of MRI experiments result in several types of contrast. The primary types are T1- and T2-weighted contrast. In T1-weighted imaging, the combination of generally low relaxation time (TR) and echo time (TE) results in the selective enhancement of short T1 regions relative to long T1 regions. Tissue with large macromolecules show efficient transfer of energy from the hydrogen nuclei to enable spins to transition from the high energy to lower energy state. As a result, tissue rich with macromolecules, such as adipose tissue, possess shortest T1, while dilute regions, including water-rich tumors and cysts, have relatively higher T1. Thus, tumors are typically hypointense in non-contrast enhanced T1-weighted imaging.

Introduction of paramagnetic contrast may be used to generate positive contrast, through T1 shortening. The most common paramagnetic contrast agents are gadolinium chelates. Gadolinium facilitates energy transfer for hydrogen nuclei by chemical exchange of water molecules in the inner coordination shell of the gadolinium molecule (*101*). Gadolinium chelates are preferentially taken up in tumor and inflammation regions due to high perfusion and vascular availability, resulting in hyper-intense signal intensity in the tumor region relative to surrounding tissue.

T2-weighted images rely on long TR and TE for the enhancement of relatively high T2 regions, such as inflamed or diseased tissue. T2 dephasing is driven by the molecular environment with dipole-driven non-uniformities in the magnetic field. Regions with high macromolecular content have a reduced rate of motion for water molecules, resulting in increased dipolar interactions and subsequent field inhomogeneities that translate to shorter T2. By contrast, water-rich regions with dilute concentration of macromolecules have rapid rates of motion, resulting in brief interactions and a more uniform magnetic environment. As a result, tumor and cystic tissue appears hyper-intense relative to surrounding tissue.

1.3.3.2 Current applications in MM

Due to its strong soft tissue contrast and spatial resolution, MRI is increasingly used in MM diagnosis and staging. IMWG recommendations suggest that the detection of one or more focal lesions is a leading indicator for the onset of symptomatic myeloma (*94*). The primary MR methods tested in MM clinical care are non-contrast enhanced T1- and T2-weighted imaging, diffusion weighted, and dynamic contrast enhancing sequences.

Due to the heterogeneous composition of hematopoietic and adipose marrow in the adult human vertebrae, T1-weighted and fat-suppressed T2-weighted imaging in a non-tumor bearing case show finely textured hyper-intense and isointense signal in the vertebrae, respectively. MM intramedullary lesions display focal lesions, diffuse infiltrations, or variegated textures that are detectable by T1-weighted and fat-suppressed T2-weighted MRI (**Figure 1.10**) (*102*). Several traditional biomarkers, including osteoclast numbers, VEGF expression, and plasma cell infiltration, are strongly correlated to the presence of these lesions in T1-weighted and fat-suppressed, T2-weighted imaging (*103,104*). T1-weighted MRI especially showed a high correlation between diffuse infiltration in the vertebrae and poor prognosis.

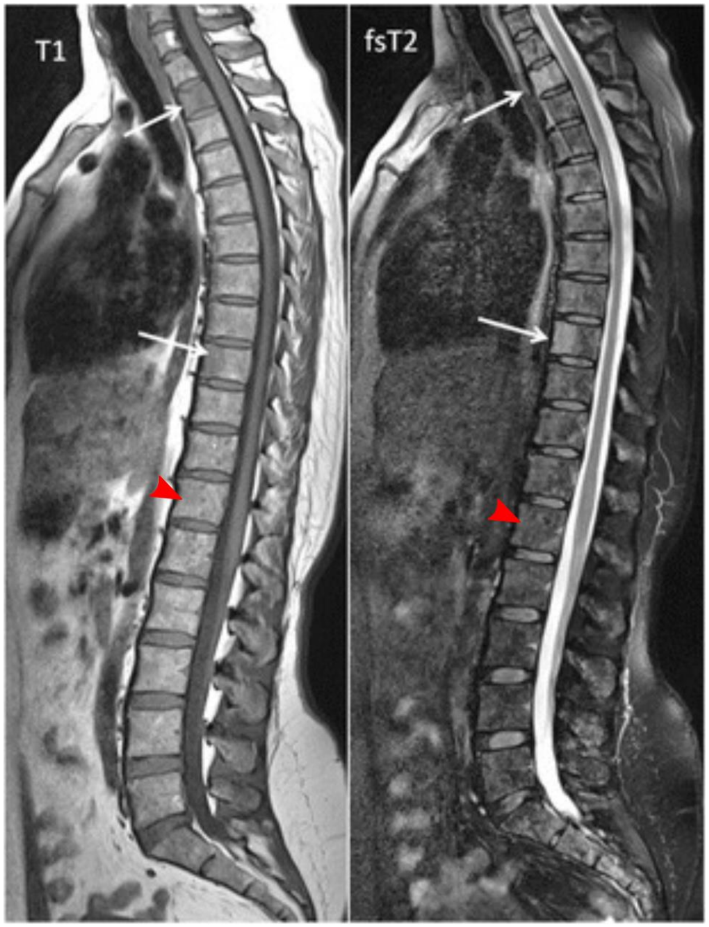

Figure 1.10: Representative T1-weighted (left) and fat-suppressed (fs) T2-weighted (right) MRI of spinal column in a patient with symptomatic MM. White arrow, focal lesion; red arrowhead, diffuse infiltration. Adapted and reprinted from (*102*).

Most standard MR protocols in imaging MM minimize the use of gadolinium contrast for highlighting tumor burden contrast due to the renal toxicity of these chelates. The Food and Drug Administration (FDA) black box warning on gadolinium states a risk of nephrogenic systemic fibrosis from gadolinium use in patients with renal insufficiencies. MM patients have a high possibility of renal failures from the release of calcium and M-protein into blood, which makes gadolinium use a significant challenge in MM. Thus, there is significant research in the development of alternate T1 and T2 weighted contrast agents, by utilizing ultra-small superparamagnetic iron oxide nanoparticles (<5nm) or novel doped iron oxide nanoparticles (*105,106*). The design and validation of these contrast agents is an active area of research.

However, gadolinium contrast is used experimentally in both clinical and preclinical studies for dynamic contrast enhanced (DCE) MRI. In DCE MRI, an intravenous bolus of gadolinium is tracked using a high temporal resolution gradient echo sequence within a field of view. Uptake and retention of the contrast agent is a function of vascular density and perfusion. Using kinetic modeling and curve statistics, DCE data can be converted into multi-parametric maps for the peak uptake, influx and washout rates, and total uptake (*107*). In MM, increases in peak uptake and influx rate derived from two-compartmental modeling of DCE MR in the pelvis of treated patients correlated with plasma cell infiltration and vessel density (*108*).

DCE MR can also be combined with diffusion-weighted imaging (DWI). DWI is dependent on the differential diffusion rates of macromolecules within a magnetic field to generate T2-weighted signal at two or more diffusion-sensitizing gradients. The characteristic time of the exponential decay in signal is the apparent diffusion constant (ADC). Voxel-wise ADC is dependent on several factors, including cell density and tortuosity. In MM, median ADC correlated to BM cellularity and vascular density, while showing statistically significant decreases following therapy (*109*).

Finally, several small studies have explored the use of voxel-wise magnetic resonance spectroscopy (MRS) to assess adipose tissue content and the ratio of adipose to hematopoietic marrow. MRS probes the 1D chemical spin composition of a region or voxel and provides a snapshot of the composing species in that area. MRS is used extensively in imaging brain tissue, particularly gliomas, where the presence of glutamate, choline, and other small molecule species correlate to disease progression and stage. In MM, the BM signal is generally overwhelmed by water and fatty acids, thus rendering MRS as a blunt tool for assessing adipose fractions. As discussed in Section 1.2.2.1, there is conflicting evidence on the role of the adipose marrow in regulating and protecting myeloma cells in the hematopoietic marrow. However, clinical MRS of spinal and pelvic BM has shown significant increases in lipid fractions in responding patients, suggesting an increase in adipose tissue relative to the hematopoietic marrow (*110*).

In addition to the technologies presented above, there are several imaging and post-processing strategies explored in the MM MRI literature. There is a recent explosion in studies using quantitative texture metrics in combination with non-linear regression models and machine learning approaches. These studies may improve assessments of therapy response by harnessing more granular information compared to standard statistics. However, research in these fields is relatively nascent and requires larger datasets to reduce overfitting and other errors derived from the larger, inhomogeneous MM patient population.

1.3.4 *Near-infrared optical imaging provides high-throughput preclinical functional imaging*

As discussed in Section 1.3.2, functional imaging plays an important role in the diagnosis, staging, and therapy response monitoring in clinical MM care. The primary modality is PET, which combines high sensitivity and temporal resolution for assessment of tissue metabolic activity. For preclinical testing and validation of contrast agents and biomarkers, however, PET has certain disadvantages. The technology is relatively low throughput, and, due to the positron-based contrast generation, cannot provide support the use of multiple contrast agents in parallel. Multiplexed biomarkers can be used to identify the spatial distribution of corresponding metabolic activities at the tissue and individual cell levels.

One preclinical alternative is to use optical imaging. Optical imaging is low cost and high-throughput. Additionally, due to the availability of multiple wavelengths that can be utilized, it supports the combination of several imaging probes within the same experiment. Crucially, this provides a method for multiplexing contrast agents for identifying the spatial localization of target markers within the tissue and cells.

Fluorescent optical imaging is primarily hampered by its penetration depth and spatial resolution. All tissue contain several endogenous chromophores that minimize penetration of excitation and emission light, primarily due to absorbance, while background autofluorescence contributes to imaging noise. As a result, near infrared (NIR) fluorophores are used for *in vivo* imaging, due to the presence of a local minimum in the absorption of 700-900nm wavelengths by oxygenated and deoxygenated hemoglobin (**Figure 1.11**) (*111*). This enhances penetration and improves sensitivity.

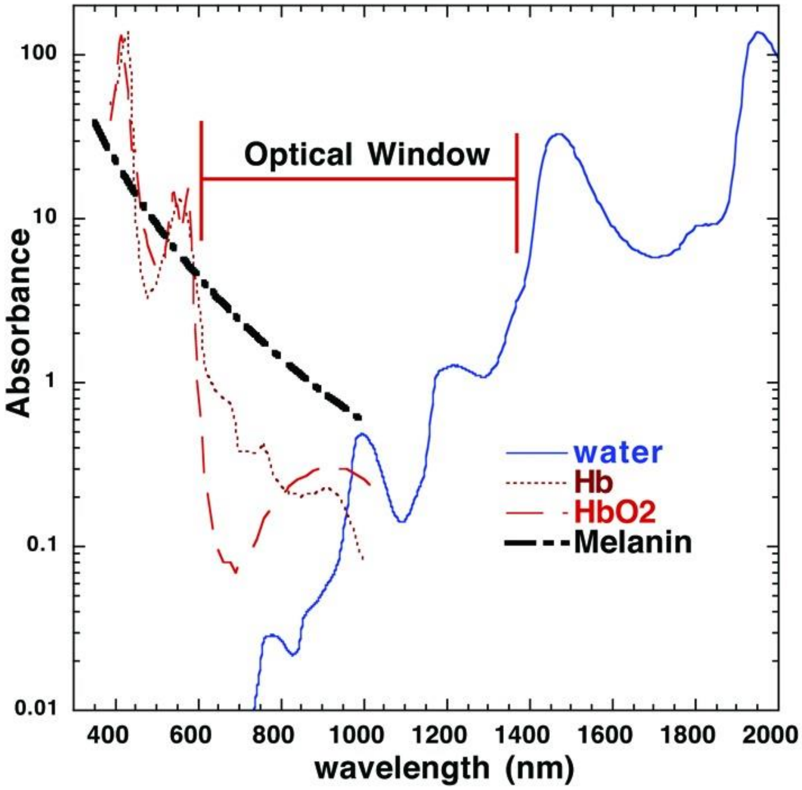

Figure 1.11: Absorption spectra of common tissue components. Hb, deoxygenated hemoglobin; HbO2, oxygenated hemoglobin. Reprinted from (*111*).

In MM preclinical research, there is paucity of exogenous NIR fluorophores that are targeted to myeloma-specific biomarkers. This is partly due to the limited spatial resolution of fluorescent imaging methods. Although the optical window affords increased light penetration, tissue turbidity, presence of large macromolecules, and other chromophores cause scattering.

As a result, fluorescent images exhibit diffuse signal that is more spatially distributed relative to its generating region. Several experimental methods and technologies have attempted to reduce the effect of scattering on image generation, including tomographic acquisition, structured illumination, and scatter correction using Monte Carlo simulations (*112-114*). However, these methods are often application specific. Most early stage MM is intramedullary, which severely restricts the use of fluorescence since dense bone tissue increases scattering.

Despite the limitations, there is some research in imaging joint inflammation for osteoarthritis and bone injury applications (*115*). For instance, use of a NIR bisphosphonate analog in a bone loss model demonstrated specific uptake of the contrast agent in osteonecrotic areas, indicating regional specificity for modeling bisphosphonate activity *in vivo* (*116*). Bisphosphonates are also used in MM, often in combination with chemotherapeutics, for promoting bone regrowth following myeloma-induced bone loss (*117*). Another study imaged osteoclast activity with a cathepsin-K specific activatable NIR probe to assess bone degradation and resorption (*118*). These studies show promise for bone-specific *in vivo* imaging for preclinical MM models. Additionally, exogenous fluorophores can be combined with transfection models that express luciferase or fluorescent proteins for spatial registration of markers. Optical imaging of VLA-4 activity in intramedullary, immunocompetent MM is explored in this dissertation.

1.4 Summary

Multiple studies have shown the dependence of MM tumors on the surrounding BM microenvironment and the role of the bidirectional signaling for influencing disease pathogenesis and treatment response. Clinical FDG-PET and MRI are critical for monitoring therapy response and changing treatment paradigms to minimize toxicities and improve patient quality of life. Both PET and MRI provide indirect metrics on state of disease, although PET tracers are designed to assess metabolic activity and receptor densities on the tumor cells. As a result, PET imaging correlates to the intra-tumor and tumor-microenvironment interactions, which respond to and affect the therapy response. In preclinical imaging, NIR optical imaging can provide PET-like sensitivity and offers parallelized biomarker imaging for identifying whole tissue expression that can be localized *ex vivo*.

By contrast, MRI provides a macro view on the BM tissue dynamics and its response to the MM tumors. Use of DCE and DWI in particular highlight angiogenesis and cell density, while standard T1- and T2-weighted imaging responds to changes in types of intramedullary lesions following treatment. MM clinical care typically utilizes multiple factors, including changes in total uptake and number of lesions in FDG-PET, multi-parametric MRI, and a combination of cytogenetic, serum, and site-specific biopsied markers, to derive an assessment for diagnostics, staging, and response to therapy. Despite several advances in treatment strategies and early identification of non-responders for stratification and personalization of care, MM remains incurable, with successive relapse cycles lasting progressively shorter. Thus, there is a need for the development and validation of contrast agents and methods for rapidly imaging changes in BM structure, intratumoral metabolic activity, and tumor to environment interactions.

1.5 Specific aims and Dissertation outline

1.5.1 Specific aims

Myeloma cells' interaction with the environment and their intracellular metabolic activity profiles drive disease progression and therapy efficacy. We have identified the following aims to probe disease behavior at intracellular, myeloma to BM environmental signaling, and macroscale BM tissue changes in preclinical intramedullary and extramedullary immunocompetent models of MM.

Aim 1: To validate LAT1 surface expression imaging using FDOPA-PET and develop FDOPA-PET uptake metrics as a surrogate for melphalan efficacy.

Aim 2: To study uptake of the VLA-4 specific optical probe for identifying VLA-4 expression *in vivo* and in response to bortezomib therapy.

Aim 3: To identify preclinical MRI parameters for longitudinal imaging of diffuse intramedullary tumor burden in response to bortezomib therapy.

1.5.2 Dissertation outline

The current chapter provides an overview of BM and MM biology, therapy strategies and mechanisms, and current imaging paradigms in MM care.

Imaging of LAT1 surface expression and melphalan therapeutic efficacy is covered in Chapter 2. ^{18}F-FDOPA-PET uptake in aggressive extramedullary MM was compared to structural tumor burden and LAT1 expression using T2-weighted MRI and immunohistochemistry, respectively.

In Chapter 3, *in vivo* imaging of the activated form of VLA-4 was used to assess response to proteasome inhibitor therapy using bortezomib. Uptake of the peptidomimetic optical probe in VLA-4 expressing tumor cells was validated using *ex vivo* flow cytometry and planar fluorescent biodistribution.

In Chapter 4, the overall effect on BM tissue and tumor burden was assessed longitudinally using small animal MRI in diffuse, intramedullary disease following bortezomib therapy. Tumor burden and changes in adipose tissue distribution and tissue density were validated using hematoxylin and eosin staining of the femur and tibia BM.

Finally, the general conclusions, limitations, and future work are discussed in Chapter 5.

1.6 References

1. Palumbo A, Anderson K. Multiple myeloma. *New England Journal of Medicine.* 2011;364:1046-1060.

2. Becker N. Epidemiology of multiple myeloma. In: Moehler T, Goldschmidt H, eds. *Multiple Myeloma*. Berlin, Heidelberg: Springer Berlin Heidelberg; 2011:25-35.

3. Siegel RL, Miller KD, Jemal A. Cancer statistics, 2018. *CA Cancer J Clin.* 2018;68:7-30.

4. Brenner H, Gondos A, Pulte D. Recent major improvement in long-term survival of younger patients with multiple myeloma. *Blood.* 2008;111:2521-2526.

5. Cancer stat facts: myeloma. https://seer.cancer.gov/statfacts/html/mulmy.html. Accessed December 16, 2017.

6. Morgan GJ, Walker BA, Davies FE. The genetic architecture of multiple myeloma. *Nat Rev Cancer.* 2012;12:335-348.

7. R.L.E C, H.D.E L. Introduction to T and B lymphocytes. In: Anaya JM, Shoenfeld Y, Rojas-Villarraga A, Levy RA, Cervera R, eds. *Autoimmunity: From Bench to Bedside*. Bogota (Colombia); 2013.

8. Prideaux SM, Conway O'Brien E, Chevassut TJ. The genetic architecture of multiple myeloma. *Adv Hematol.* 2014;2014:864058.

9. Mitsiades CS, Mitsiades NS, Munshi NC, Richardson PG, Anderson KC. The role of the bone microenvironment in the pathophysiology and therapeutic management of multiple myeloma: interplay of growth factors, their receptors and stromal interactions. *Eur J Cancer.* 2006;42:1564-1573.

10. van Kempen LCLT, Ruiter DJ, van Muijen GNP, Coussens LM. The tumor microenvironment: a critical determinant of neoplastic evolution. *Eur J Cell Biol.* 2003;82:539-548.

11. Travlos GS. Normal Structure, Function, and Histology of the Bone Marrow. *Toxicol Pathol.* 2006;34:548-565.

12. Reagan MR, Rosen CJ. Navigating the bone marrow niche: translational insights and cancer-driven dysfunction. *Nat Rev Rheumatol.* 2016;12:154-168.

13. Cawthorn WP, Scheller EL, Learman BS, et al. Bone marrow adipose tissue is an endocrine organ that contributes to increased circulating adiponectin during caloric restriction. *Cell Metab.* 2014;20:368-375.

14. Scheller EL, Cawthorn WP, Burr AA, Horowitz MC, MacDougald OA. Marrow Adipose Tissue: Trimming the Fat. *Trends Endocrinol Metab.* 2016;27:392-403.

15. Li Z, Hardij J, Bagchi DP, Scheller EL, MacDougald OA. Development, regulation, metabolism and function of bone marrow adipose tissues. *Bone.* 2018;110:134-140.

16. Justesen J, Stenderup K, Ebbesen EN, Mosekilde L, Steiniche T, Kassem M. Adipocyte tissue volume in bone marrow is increased with aging and in patients with osteoporosis. *Biogerontology.* 2001;2:165-171.

17. Martin RB, Zissimos SL. Relationships between marrow fat and bone turnover in ovariectomized and intact rats. *Bone.* 1991;12:123-131.

18. Li M, Shen Y, Qi H, Wronski TJ. Comparative study of skeletal response to estrogen depletion at red and yellow marrow sites in rats. *The Anatomical Record.* 1996;245:472-480.

19. Ambrosi TH, Scialdone A, Graja A, et al. Adipocyte Accumulation in the Bone Marrow during Obesity and Aging Impairs Stem Cell-Based Hematopoietic and Bone Regeneration. *Cell Stem Cell.* 2017;20:771-784.e776.

20. Zhou BO, Yu H, Yue R, et al. Bone marrow adipocytes promote the regeneration of stem cells and haematopoiesis by secreting SCF. *Nat Cell Biol.* 2017;19:891.

21. DiMascio L, Voermans C, Uqoezwa M, et al. Identification of Adiponectin as a Novel Hemopoietic Stem Cell Growth Factor. *The Journal of Immunology.* 2007;178:3511-3520.

22. Boyd AL, Reid JC, Salci KR, et al. Acute myeloid leukaemia disrupts endogenous myelo-erythropoiesis by compromising the adipocyte bone marrow niche. *Nat Cell Biol.* 2017;19:1336.

23. Elbaz A, Wu X, Rivas D, Gimble JM, Duque G. Inhibition of fatty acid biosynthesis prevents adipocyte lipotoxicity on human osteoblasts in vitro. *J Cell Mol Med.* 2010;14:982-991.

24. Hardaway AL, Herroon MK, Rajagurubandara E, Podgorski I. Marrow adipocyte-derived CXCL1 and CXCL2 contribute to osteolysis in metastatic prostate cancer. *Clin Exp Metastasis.* 2015;32:353-368.

25. Falank C, Fairfield H, Reagan MR. Signaling Interplay between Bone Marrow Adipose Tissue and Multiple Myeloma cells. *Front Endocrinol (Lausanne).* 2016;7:67.

26. Lee C, Oh J-I, Park J, et al. TNFα Mediated IL-6 Secretion Is Regulated by JAK/STAT Pathway but Not by MEK Phosphorylation and AKT Phosphorylation in U266 Multiple Myeloma Cells. *BioMed Research International.* 2013;2013:8.

27. Fairfield H, Falank C, Avery L, Reagan MR. Multiple myeloma in the marrow: pathogenesis and treatments. *Ann N Y Acad Sci.* 2016;1364:32-51.

28. Nair S, Branagan AR, Liu J, Boddupalli CS, Mistry PK, Dhodapkar MV. Clonal Immunoglobulin against Lysolipids in the Origin of Myeloma. *N Engl J Med.* 2016;374:555-561.

29. Vogl DT, Wang T, Pérez WS, et al. Effect of Obesity on Outcomes after Autologous Hematopoietic Stem Cell Transplantation for Multiple Myeloma. *Biol Blood Marrow Transplant.* 2011;17:1765-1774.

30. Dalamaga M, Karmaniolas K, Panagiotou A, et al. Low circulating adiponectin and resistin, but not leptin, levels are associated with multiple myeloma risk: a case–control study. *Cancer Causes Control.* 2009;20:193-199.

31. Medina EA, Oberheu K, Polusani SR, Ortega V, Velagaleti GVN, Oyajobi BO. PKA/AMPK signaling in relation to adiponectin's antiproliferative effect on multiple myeloma cells. *Leukemia.* 2014;28:2080.

32. Morrison SJ, Scadden DT. The bone marrow niche for haematopoietic stem cells. *Nature.* 2014;505:327.

33. Ding L, Morrison SJ. Haematopoietic stem cells and early lymphoid progenitors occupy distinct bone marrow niches. *Nature.* 2013;495:231.

34. Asada N, Katayama Y. Regulation of hematopoiesis in endosteal microenvironments. *Int J Hematol.* 2014;99:679-684.

35. Chow A, Huggins M, Ahmed J, et al. CD169+ macrophages provide a niche promoting erythropoiesis under homeostasis and stress. *Nat Med.* 2013;19:429.

36. Chang MK, Raggatt L-J, Alexander KA, et al. Osteal Tissue Macrophages Are Intercalated throughout Human and Mouse Bone Lining Tissues and Regulate Osteoblast Function In Vitro and In Vivo. *The Journal of Immunology.* 2008;181:1232-1244.

37. Winkler IG, Sims NA, Pettit AR, et al. Bone marrow macrophages maintain hematopoietic stem cell (HSC) niches and their depletion mobilizes HSCs. *Blood.* 2010;116:4815-4828.

38. Sugiyama T, Kohara H, Noda M, Nagasawa T. Maintenance of the Hematopoietic Stem Cell Pool by CXCL12-CXCR4 Chemokine Signaling in Bone Marrow Stromal Cell Niches. *Immunity.* 2006;25:977-988.

39. Sacchetti B, Funari A, Michienzi S, et al. Self-Renewing Osteoprogenitors in Bone Marrow Sinusoids Can Organize a Hematopoietic Microenvironment. *Cell.* 2007;131:324-336.

40. Winkler IG, Barbier V, Wadley R, Zannettino AC, Williams S, Levesque JP. Positioning of bone marrow hematopoietic and stromal cells relative to blood flow in vivo: serially reconstituting hematopoietic stem cells reside in distinct nonperfused niches. *Blood.* 2010;116:375-385.

41. Palomäki S, Pietilä M, Laitinen S, et al. HIF-1α is upregulated in human mesenchymal stem cells. *Stem Cells.* 2013;31:1902-1909.

42. Andrade PZ, Soure AM, Santos F, Paiva A, Cabral JMS, Silva CL. Ex vivo expansion of cord blood haematopoietic stem/progenitor cells under physiological oxygen tensions: clear-cut effects on cell proliferation, differentiation and metabolism. *J Tissue Eng Regen Med.* 2015;9:1172-1181.

43. Baschuk N, Rautela J, Parker BS. Bone specific immunity and its impact on metastasis. *BoneKEy reports.* 2015;4:665-665.

44. Kingsley LA, Fournier PGJ, Chirgwin JM, Guise TA. Molecular Biology of Bone Metastasis. *Mol Cancer Ther.* 2007;6:2609-2617.

45. Weilbaecher KN, Guise TA, McCauley LK. Cancer to bone: a fatal attraction. *Nature Reviews Cancer.* 2011;11:411.

46. Oshima T, Abe M, Asano J, et al. Myeloma cells suppress bone formation by secreting a soluble Wnt inhibitor, sFRP-2. *Blood.* 2005;106:3160-3165.

47. Qiang Y-W, Chen Y, Stephens O, et al. Myeloma-derived Dickkopf-1 disrupts Wnt-regulated osteoprotegerin and RANKL production by osteoblasts: a potential mechanism underlying osteolytic bone lesions in multiple myeloma. *Blood.* 2008;112:196-207.

48. Abe M. Targeting the interplay between myeloma cells and the bone marrow microenvironment in myeloma. *Int J Hematol.* 2011;94:334-343.

49. Abe M, Hiura K, Ozaki S, Kido S, Matsumoto T. Vicious cycle between myeloma cell binding to bone marrow stromal cells via VLA-4–VCAM-1 adhesion and macrophage inflammatory protein-1α and MIP-1β production. *J Bone Miner Metab.* 2009;27:16-23.

50. Sanz-rodríguez F, Teixidó J. VLA-4-Dependent Myeloma Cell Adhesion. *Leuk Lymphoma.* 2001;41:239-245.

51. Schlesinger M, Bendas G. Contribution of very late antigen-4 (VLA-4) integrin to cancer progression and metastasis. *Cancer Metastasis Rev.* 2015;34:575-591.

52. Rajkumar SV. Treatment of multiple myeloma. *Nature Reviews Clinical Oncology.* 2011;8:479.

53. Fonseca R, Bergsagel PL, Drach J, et al. International Myeloma Working Group molecular classification of multiple myeloma: spotlight review. *Leukemia.* 2009;23:2210.

54. Groll M, Berkers CR, Ploegh HL, Ovaa H. Crystal Structure of the Boronic Acid-Based Proteasome Inhibitor Bortezomib in Complex with the Yeast 20S Proteasome. *Structure.* 2006;14:451-456.

55. Kubiczkova L, Pour L, Sedlarikova L, Hajek R, Sevcikova S. Proteasome inhibitors – molecular basis and current perspectives in multiple myeloma. *J Cell Mol Med.* 2014;18:947-961.

56. Hideshima T, Ikeda H, Chauhan D, et al. Bortezomib induces canonical nuclear factor-κB activation in multiple myeloma cells. *Blood.* 2009;114:1046-1052.

57. Wei MC, Zong W-X, Cheng EH-Y, et al. Proapoptotic BAX and BAK: A Requisite Gateway to Mitochondrial Dysfunction and Death. *Science.* 2001;292:727-730.

58. Mitsiades N, Mitsiades CS, Poulaki V, et al. Molecular sequelae of proteasome inhibition in human multiple myeloma cells. *Proceedings of the National Academy of Sciences.* 2002;99:14374-14379.

59. Obeng EA, Carlson LM, Gutman DM, Harrington WJ, Lee KP, Boise LH. Proteasome inhibitors induce a terminal unfolded protein response in multiple myeloma cells. *Blood.* 2006;107:4907-4916.

60. von Metzler I, Krebbel H, Hecht M, et al. Bortezomib inhibits human osteoclastogenesis. *Leukemia.* 2007;21:2025.

61. Giuliani N, Morandi F, Tagliaferri S, et al. The proteasome inhibitor bortezomib affects osteoblast differentiation in vitro and in vivo in multiple myeloma patients. *Blood.* 2007;110:334-338.

62. Hideshima T, Richardson P, Chauhan D, et al. The proteasome inhibitor PS-341 inhibits growth, induces apoptosis, and overcomes drug resistance in human multiple myeloma cells. *Cancer Res.* 2001;61:3071-3076.

63. Roccaro AM, Hideshima T, Raje N, et al. Bortezomib Mediates Antiangiogenesis in Multiple Myeloma via Direct and Indirect Effects on Endothelial Cells. *Cancer Res.* 2006;66:184-191.

64. Jakubowiak AJ, Dytfeld D, Griffith KA, et al. A phase 1/2 study of carfilzomib in combination with lenalidomide and low-dose dexamethasone as a frontline treatment for multiple myeloma. *Blood.* 2012;120:1801-1809.

65. Siegel DS, Martin T, Wang M, et al. A phase 2 study of single-agent carfilzomib (PX-171-003-A1) in patients with relapsed and refractory multiple myeloma. *Blood.* 2012;120:2817-2825.

66. Kuhn DJ, Chen Q, Voorhees PM, et al. Potent activity of carfilzomib, a novel, irreversible inhibitor of the ubiquitin-proteasome pathway, against preclinical models of multiple myeloma. *Blood.* 2007;110:3281-3290.

67. Oerlemans R, Franke NE, Assaraf YG, et al. Molecular basis of bortezomib resistance: proteasome subunit β5 (PSMB5) gene mutation and overexpression of PSMB5 protein. *Blood.* 2008;112:2489-2499.

68. Bianchi G, Oliva L, Cascio P, et al. The proteasome load versus capacity balance determines apoptotic sensitivity of multiple myeloma cells to proteasome inhibition. *Blood.* 2009;113:3040-3049.

69. Kawano Y, Moschetta M, Manier S, et al. Targeting the bone marrow microenvironment in multiple myeloma. *Immunol Rev.* 2015;263:160-172.

70. Hideshima T, Mitsiades C, Tonon G, Richardson PG, Anderson KC. Understanding multiple myeloma pathogenesis in the bone marrow to identify new therapeutic targets. *Nature Reviews Cancer.* 2007;7:585-598.

71. Feyler S, Scott GB, Parrish C, et al. Tumour Cell Generation of Inducible Regulatory T-Cells in Multiple Myeloma Is Contact-Dependent and Antigen-Presenting Cell-Independent. *PLoS One.* 2012;7:e35981.

72. Zhu YX, Kortuem KM, Stewart AK. Molecular mechanism of action of immune-modulatory drugs thalidomide, lenalidomide and pomalidomide in multiple myeloma. *Leuk Lymphoma.* 2013;54:683-687.

73. Quach H, Ritchie D, Stewart AK, et al. Mechanism of action of immunomodulatory drugs (IMiDS) in multiple myeloma. *Leukemia.* 2009;24:22.

74. Geitz H, Handt S, Zwingenberger K. Thalidomide selectively modulates the density of cell surface molecules involved in the adhesion cascade. *Immunopharmacology.* 1996;31:213-221.

75. Dredge K, Marriott JB, Macdonald CD, et al. Novel thalidomide analogues display anti-angiogenic activity independently of immunomodulatory effects. *Br J Cancer.* 2002;87:1166.

76. Dredge K, Horsfall R, Robinson SP, et al. Orally administered lenalidomide (CC-5013) is anti-angiogenic in vivo and inhibits endothelial cell migration and Akt phosphorylation in vitro. *Microvasc Res.* 2005;69:56-63.

77. Davies FE, Raje N, Hideshima T, et al. Thalidomide and immunomodulatory derivatives augment natural killer cell cytotoxicity in multiple myeloma. *Blood.* 2001;98:210-216.

78. Hayashi T, Hideshima T, Akiyama M, et al. Molecular mechanisms whereby immunomodulatory drugs activate natural killer cells: clinical application. *Br J Haematol.* 2005;128:192-203.

79. Galustian C, Meyer B, Labarthe M-C, et al. The anti-cancer agents lenalidomide and pomalidomide inhibit the proliferation and function of T regulatory cells. *Cancer Immunol Immunother.* 2009;58:1033-1045.

80. Görgün GT, Whitehill G, Anderson JL, et al. Tumor-promoting immune-suppressive myeloid-derived suppressor cells in the multiple myeloma microenvironment in humans. *Blood.* 2013;121:2975-2987.

81. Gomez-Bougie P, Oliver L, Le Gouill S, Bataille R, Amiot M. Melphalan-induced apoptosis in multiple myeloma cells is associated with a cleavage of Mcl-1 and Bim and a decrease in the Mcl-1/Bim complex. *Oncogene.* 2005;24:8076.

82. Esma F, Salvini M, Troia R, Boccadoro M, Larocca A, Pautasso C. Melphalan hydrochloride for the treatment of multiple myeloma. *Expert Opin Pharmacother.* 2017;18:1127-1136.

83. Rellick SL, Piktel D, Walton C, et al. Melphalan exposure induces an interleukin-6 deficit in bone marrow stromal cells and osteoblasts. *Cytokine.* 2012;58:245-252.

84. Kuczma M, Ding Z-C, Zhou G. Immunostimulatory Effects of Melphalan and Usefulness in Adoptive Cell Therapy with Antitumor CD4+ T Cells. *Crit Rev Immunol.* 2016;36:179-191.

85. Rajkumar SV. Multiple myeloma: 2014 Update on diagnosis, risk-stratification, and management. *Am J Hematol.* 2014;89:998-1009.

86. Yang W-C, Lin S-F. Mechanisms of Drug Resistance in Relapse and Refractory Multiple Myeloma. *BioMed Research International.* 2015;2015:17.

87. Vavricka SR, Burri E, Beglinger C, Degen L, Manz M. Serum protein electrophoresis: an underused but very useful test. *Digestion.* 2009;79:203-210.

88. Bhole MV, Sadler R, Ramasamy K. Serum-free light-chain assay: clinical utility and limitations. *Ann Clin Biochem.* 2014;51:528-542.

89. Bonilla FA. Pharmacokinetics of immunoglobulin administered via intravenous or subcutaneous routes. *Immunol Allergy Clin North Am.* 2008;28:803-819, ix.

90. Lonial S, Kaufman JL. Non-secretory myeloma: a clinician's guide. *Oncology (Williston Park).* 2013;27:924-928, 930.

91. Cherry SR, Dahlbom M. PET: physics, instrumentation, and scanners. Paper presented at: PET, 2006.

92. Vander Heiden MG, Cantley LC, Thompson CB. Understanding the Warburg effect: the metabolic requirements of cell proliferation. *Science.* 2009;324:1029-1033.

93. van Lammeren-Venema D, Regelink JC, Riphagen II, Zweegman S, Hoekstra OS, Zijlstra JM. 18F-fluoro-deoxyglucose positron emission tomography in assessment of myeloma-related bone disease: A systematic review. *Cancer.* 2012;118:1971-1981.

94. Rajkumar SV. Multiple myeloma: 2016 update on diagnosis, risk-stratification, and management. *Am J Hematol.* 2016;91:719-734.

95. Isoda A, Kaira K, Iwashina M, et al. Expression of L-type amino acid transporter 1 (LAT1) as a prognostic and therapeutic indicator in multiple myeloma. *Cancer Sci.* 2014;105:1496-1502.

96. Plathow C, Weber WA. Tumor Cell Metabolism Imaging. *J Nucl Med.* 2008;49:43S-63S.

97. Lyssiotis Costas A, Cantley Lewis C. Acetate Fuels the Cancer Engine. *Cell.* 2014;159:1492-1494.

98. Fontana F, Ge X, Su X, et al. Evaluating Acetate Metabolism for Imaging and Targeting in Multiple Myeloma. *Clin Cancer Res.* 2017;23:416-429.

99. Lin C, Ho C-L, Ng S-H, et al. 11C-Acetate as a new biomarker for PET/CT in patients with multiple myeloma: initial staging and postinduction response assessment. *Eur J Nucl Med Mol Imaging.* 2014;41:41-49.

100. Soodgupta D, Zhou H, Beaino W, et al. Ex Vivo and In Vivo Evaluation of Overexpressed VLA-4 in Multiple Myeloma Using LLP2A Imaging Agents. *J Nucl Med.* 2016;57:640-645.

101. Burtea C, Laurent S, Vander Elst L, Muller RN. Contrast Agents: Magnetic Resonance. In: Semmler W, Schwaiger M, eds. *Molecular Imaging I*. Berlin, Heidelberg: Springer Berlin Heidelberg; 2008:135-165.

102. Dutoit JC, Verstraete KL. MRI in multiple myeloma: a pictorial review of diagnostic and post-treatment findings. *Insights Imaging.* 2016;7:553-569.

103. Lee S-Y, Kim H-J, Shin YR, Park H-J, Lee Y-G, Oh SJ. Prognostic significance of focal lesions and diffuse infiltration on MRI for multiple myeloma: a meta-analysis. *Eur Radiol.* 2017;27:2333-2347.

104. Moulopoulos LA, Dimopoulos MA, Christoulas D, et al. Diffuse MRI marrow pattern correlates with increased angiogenesis, advanced disease features and poor prognosis in newly diagnosed myeloma treated with novel agents. *Leukemia.* 2010;24:1206-1212.

105. Wei H, Bruns OT, Kaul MG, et al. Exceedingly small iron oxide nanoparticles as positive MRI contrast agents. *Proceedings of the National Academy of Sciences.* 2017;114:2325-2330.

106. Clavijo Jordan MV, Beeman SC, Baldelomar EJ, Bennett KM. Disruptive chemical doping in a ferritin-based iron oxide nanoparticle to decrease r2 and enhance detection with T1-weighted MRI. *Contrast Media Mol Imaging.* 2014;9:323-332.

107. Image Post-processing Protocols. *Breast MRI: Fundamentals and Technical Aspects*. New York, NY: Springer New York; 2008:171-186.

108. Nosàs-Garcia S, Moehler T, Wasser K, et al. Dynamic contrast-enhanced MRI for assessing the disease activity of multiple myeloma: a comparative study with histology and clinical markers. *J Magn Reson Imaging.* 2005;22:154--162.

109. Hillengass J, Bauerle T, Bartl R, et al. Diffusion-weighted imaging for non-invasive and quantitative monitoring of bone marrow infiltration in patients with monoclonal plasma cell disease: a comparative study with histology. *Br J Haematol.* 2011;153:721-728.

110. Oriol A, Valverde D, Capellades J, Cabanas ME, Ribera JM, Arus C. In vivo quantification of response to treatment in patients with multiple myeloma by 1H magnetic resonance spectroscopy of bone marrow. *MAGMA.* 2007;20:93-101.

111. Kashiwagi S, Brauns T, Gelfand J, Poznansky MC. Laser vaccine adjuvants. History, progress, and potential. *Hum Vaccin Immunother.* 2014;10:1892-1907.

112. Ntziachristos V, Turner GM, Dunham J, et al. Planar fluorescence imaging using normalized data, 2005.

113. Sun J, Miller JP, Hathi D, et al. Enhancing *in vivo* tumor boundary delineation with structured illumination fluorescence molecular imaging and spatial gradient mapping, 2016.

114. Stuker F, Ripoll J, Rudin M. Fluorescence molecular tomography: principles and potential for pharmaceutical research. *Pharmaceutics.* 2011;3:229-274.

115. Slooter MD, Bierau K, Chan AB, Löwik CWGM. Near Infrared Fluorescence Imaging for early detection, monitoring and improved intervention of diseases involving the joint. *Connect Tissue Res.* 2015;56:153-160.

116. Kozloff KM, Volakis LI, Marini JC, Caird MS. Near-infrared fluorescent probe traces bisphosphonate delivery and retention in vivo. *J Bone Miner Res.* 2010;25:1748-1758.

117. Mhaskar R, Kumar A, Miladinovic B, Djulbegovic B. Bisphosphonates in multiple myeloma: an updated network meta-analysis. *Cochrane Database of Systematic Reviews.* 2017.

118. Kozloff KM, Quinti L, Patntirapong S, et al. Non-invasive optical detection of cathepsin K-mediated fluorescence reveals osteoclast activity in vitro and in vivo. *Bone.* 2009;44:190-198.

Chapter 2: Imaging melphalan therapy response in preclinical extramedullary myeloma with ^{18}F-FDOPA and ^{18}F-FDG PET

2.1 Overview

In this study, ^{18}F-FDOPA uptake in an extramedullary xenograft myeloma lesion was studied following melphalan therapy. Melphalan related toxicities and poor efficacy is a primary reason for the increasing lack of adoption of the chemotherapeutic agent in front-line MM clinical care. However, it is a key component of post-relapse treatment strategies and in elderly, transplant ineligible patients that cannot receive bortezomib-based regimens. To identify responding and non-responding patients, we proposed to use ^{18}F-FDOPA uptake as a surrogate for melphalan efficacy, since uptake of both melphalan and ^{18}F-FDOPA is mediated by the L-type amino acid transporter-1. Importantly, LAT1 overexpression is linked to poor prognosis in myeloma, and it is the primary system L transporter that is upregulated in most cancers.

Our results showed a significant decrease in ^{18}F-FDOPA uptake that was concordant with the established ^{18}F-FDG uptake. Immunohistochemistry showed a visible change in LAT1 expression, although, interestingly, surface density of LAT1 increased following an early and aggressive melphalan therapy regimen. This study suggests that ^{18}F-FDOPA-PET/CT can serve as a complementary method to ^{18}F-FDG-PET/CT for imaging melphalan treatment response. ^{18}F-FDOPA uptake was linked to LAT1 expression and melphalan response, with longitudinal imaging suggesting stabilization of LAT1 levels and melphalan tumor cytotoxicity. The material covered in this chapter is published in the *Journal of Nuclear Medicine (1)*.

2.2 Introduction

One of the main therapies used for treating multiple myeloma (MM) is the small molecule alkylating agent melphalan (*2-4*). However, melphalan efficacy is variable in the clinical population, especially in relapsed and refractory MM. It is also implicated in various toxicities including severe mucositis and myelosuppression. Thus, stratification of melphalan-responsive patients in the MM patient population is critical for reducing therapy-induced toxicities.

The L-type amino acid transporter-1 (LAT1) is a key mediator in the uptake and intracellular accumulation of melphalan and is correlated to melphalan sensitivity and response in MM and other cancers (*5-7*). LAT1 (SLC7A5) is a member of the system L family of transporters and is primarily expressed in fetal liver, bone marrow, placenta, and testes (*8,9*). It is overexpressed in MM and correlated to poor myeloma prognosis and survival (*7*). LAT1 is a heterodimer consisting of a light chain (SLC7A5), which provides the amino acid transporter function, and a glycosylated heavy chain subunit (CD98), which provides trafficking and membrane localization (*10,11*). LAT1 is implicated in tumor proliferation pathways, through the mammalian target of rapamycin and glutamine/glutamate signaling pathways (*12*).

The glucose analog 2-deoxy-2-[^{18}F]-fluorodeoxyglucose (^{18}F-FDG) is currently used for positron emission tomography (PET) imaging of myeloma and other cancers for disease staging and monitoring therapy response. Clinical trials in patients with MM have correlated the suppression of ^{18}F-FDG uptake to improved event-free survival (*13*). ^{18}F-FDG-PET/CT is useful for staging and response monitoring in MM, but the sensitivity for detecting marrow involvement by MM is variable, particularly with relatively low marrow burden of disease (*14*). ^{18}F-FDG uptake can be increased in the setting of inflammation after chemotherapy and in the presence of exogenous or endogenous marrow stimulation. Thus, there is a need for other PET tracers with increased sensitivity and specificity for detecting intramedullary myeloma, particularly for low disease burden. Additionally, ^{18}F-FDG uptake and retention is mediated by glucose transporter-1 (GLUT1) and hexokinase, which are involved primarily in glycolysis. As a result, ^{18}F-FDG uptake does not report on LAT1 expression and the melphalan sensitivity of MM tumors.

In this study, we sought an alternative tracer that directly interrogates the functional status of LAT1. The amino acid PET tracer 3,4-dihydroxy-6-[^{18}F]fluoro-L-phenylalanine (^{18}F-

FDOPA) is structurally related to melphalan and is primarily transported into cells by LAT1 (*15*). ^{18}F-FDOPA-PET is mostly used in imaging gliomas and neuroendocrine tumors in cancer patients (*16,17*). Because LAT1 mediates the intracellular accumulation of both ^{18}F-FDOPA and melphalan, we hypothesized that the quantification of ^{18}F-FDOPA uptake in myeloma cells will correlate with melphalan therapy response. Using an immunocompetent xenograft model of murine myeloma, we demonstrate that ^{18}F-FDOPA could serve as a complementary imaging agent to ^{18}F-FDG for MM PET imaging and potentially provide additional stratification of responders and non-responders to melphalan therapy.

2.3 Materials and Methods

2.3.1 Cell Culture and Reagents

5TGM1-GFP (5TGM1) (originally a kind gift from Dr. G. Mundy, Vanderbilt University, TN, USA; 5TGM1-GFP cells were obtained from Dr. Katherine N. Weilbaecher, Washington University, Department of Medicine) were maintained at 10^6 cells/mL in Iscove's Modified Dulbecco Medium supplemented with 10% v/v fetal bovine serum and 1% penicillin/streptomycin (all from Thermo Fisher Scientific, MA, USA). Melphalan (Sigma Aldrich, MO, USA) was prepared prior to weekly injections from 5 mg/mL 0.1M HCl EtOH stock. ^{18}F-FDG and ^{18}F-FDOPA were produced in compliance with current good manufacturing practices by the Washington University Cyclotron Facility.

2.3.2 Tumor Model and Melphalan Therapy

All animal studies were conducted according to protocols approved by the Washington University Animal Studies Committee. C57Bl/6 KaLwRij mice were unilaterally injected subcutaneously in the lower flank region with 10^6 5TGM1 cells. All tumor implantation and imaging procedures were conducted under 1-2% v/v isoflurane/100% O_2 anesthesia.

Tumor-bearing mice were separated into two independent studies. The first group consisted of two independent cohorts of treated (n=7) and untreated (n=6) mice, with melphalan therapy beginning at 14-18 days after tumor implantation. Imaging was performed at week 4 (**Figure 2.1A**). The second group (n=3) consisted of mice treated with melphalan beginning week 3 after tumor implantation. Imaging was performed weekly immediately prior to the start of the therapy regimen and continued until week 5 (**Figure 2.1B**). Melphalan therapy was administered weekly at 10mg/kg intraperitoneally in saline in each of the studies (*18*).

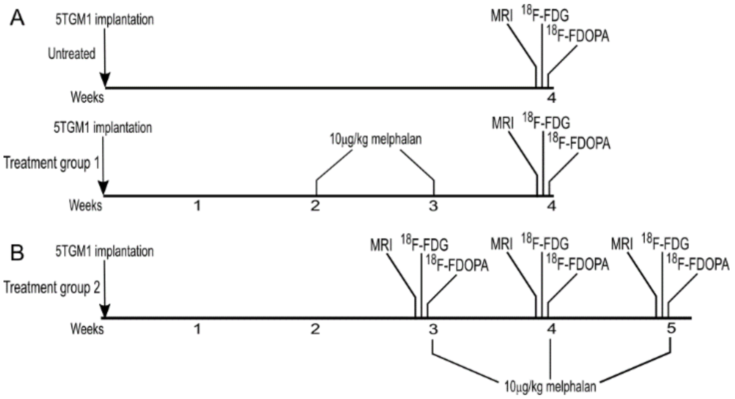

Figure 2.1: Timeline for melphalan treated and untreated cohorts. Melphalan was administered weekly beginning either (A) week 2, with imaging performed on separate, contiguous days at the end of the study, or (B) week 3 post tumor implantation. Longitudinal imaging with MRI, ^{18}F-FDG, and ^{18}F-FDOPA PET/CT was initialized prior to the start of therapy for the week 3 cohort and continued through to week 5 post tumor implantation.

2.3.3 In vivo Structural and Metabolic Imaging

Prior to PET/CT imaging, tumor structural volume was assessed by calipers and small animal magnetic resonance imaging (MRI). Mice were placed supine within a birdcage radiofrequency coil and imaged in 4.7 T (200 MHz) Varian/Agilent small animal scanner (Agilent Technologies, CA, USA). Respiration and body temperature were maintained at approximately 50 breaths/minute and 37 ^{o}C, respectively. Transverse T_2-weighted contiguous slices were collected using a spin echo sequence (repetition time, 1.5s; echo time, 40ms; averages, 2; field of view, 2.5 x 2.5 x 1.6 cm^3; data matrix 128 x 128 x 16). Region of interest analysis was performed using ImageJ (National Institutes of Health, MD, USA).

^{18}F-FDG and ^{18}F-FDOPA-PET/CT were performed on separate, contiguous days to minimize signal cross-contamination. Prior to radiotracer administration, a whole-body 60kVp CT was acquired on each mouse. Mice were injected intravenously with 7.4 MBq dosage of the tracer *via* the lateral tail vein. 60-minute dynamic scans were collected following injection of the tracer using Inveon PET/CT or Focus F220 PET imaging systems (all from Siemens Healthcare, Erlangen, Germany). ^{18}F-FDG-PET/CT was performed after mice were fasted for 6-8 hours with access to water. To standardize imaging, ^{18}F-FDOPA-PET/CT was performed after ^{18}F-FDG-PET/CT. ^{18}F-FDG and ^{18}F-FDOPA-PET/CT images were reconstructed using iterative reconstruction and displayed using Inveon Research Workplace 4.2 (Siemens Healthcare) in multi-planar views.

2.3.4 PET Image Analysis

Volumetric tumor and control tissue regions of interest were defined using companion CT and summed PET. Dynamic time activity curves (TACs) were decay corrected and converted to standard uptake values (SUV) prior to analysis. The metabolic tumor volume (MTV) (volume of tumor with $SUV > 0.42*SUV_{Max}$) (*19*), total lesion avidity (TLA) (Mean SUV in the MTV ($SUV_{Mean, MTV}$) * MTV), and total uptake (area under the curve of tracer TAC) were calculated for ^{18}F-FDOPA. MTV, total lesion glycolysis (TLG) ($SUV_{Mean, MTV}$ * MTV), and total uptake were also measured for ^{18}F-FDG. To minimize single voxel noise in SUV_{Max} measurements, SUV_{Max} was defined as the mean of the 95% isocontour (*20*).

2.3.5 Immunohistochemistry

Tumor tissue was excised, flash frozen in optimal cutting temperature compound (Tissue Tek, CA, USA), and stored at -20 ^{o}C. Tyramide amplified immunohistochemistry using Perkin Elmer TSA-Cy3 kit (PerkinElmer, Inc., MA, USA) was performed as per manufacturer's protocol(*21*). Briefly, sections were fixed in 4% v/v paraformaldehyde/phosphate buffered saline. Endogenous peroxidase and non-specific binding was blocked with 3% H_2O_2 and 0.5% TSA blocking reagent, respectively. Sections were incubated separately overnight at 4 ^{o}C with 1:50 dilutions of rabbit polyclonal anti-SLC7A5 (Proteintech Group, Inc., IL, USA), anti-GLUT1 (Abcam, Cambridge, UK), anti-CD98 (Santa Cruz Biotechnology, Inc., TX, USA), and anti-CD31 (Novus Biologicals, Littleton, CO, USA). The slides were mounted with Vectashield anti-fade mounting medium with DAPI (Vector Laboratories, Inc., CA, USA) after signal amplification with 1:50 TSA-Cy3. Stained slides were imaged on a Zeiss LSM 880 II Airyscan inverted confocal fluorescence microscope (Zeiss, Oberkochen, Germany). Slides were sequentially imaged with DAPI (excitation/emission 405/465 nm), GFP (excitation/emission 488/509 nm), and Cy3 (excitation/emission 561/603 nm) filters. As a negative control, muscle tissue excised from the contralateral leg was stained and imaged using the described settings.

2.3.6 Statistical Analysis

All statistical analysis was performed using GraphPad Prism 5.0 (GraphPad, CA, USA). Statistical significance between TACs was determined using 2-way analysis of variance (ANOVA) with repeated measures, while 1-way ANOVA with Bonferroni multiple comparisons post-testing and Student's two-tailed *t*-test were used for avidity, uptake, and volume comparisons between tracers, treatment, and tissue types. Lin's concordance correlation coefficients between ^{18}F-FDOPA and ^{18}F-FDG parameters were calculated using MATLAB 2014b (Mathworks, Inc., MA, USA).

2.4 Results

C57Bl/KaLwRij mice implanted subcutaneously with 5TGM1 congenic unilateral flank tumors were evaluated for ^{18}F-FDG and ^{18}F-FDOPA uptake at four weeks post tumor injection with 60 min dynamic PET/CT. Structural tumor volume was assessed with T_2-weighted non-contrast enhanced MRI. There was heterogeneous structural tumor volume reduction from melphalan therapy within the treatment cohort (9.9 ± 7.7-fold) (**Table 2.1; Figure 2.2A-B**). Correspondingly, metabolic volume representing ^{18}F-FDG and ^{18}F-FDOPA uptake decreased in treated mice relative to untreated mice (**Figure 2.3A-B**). Decay-corrected dynamic TACs derived from the tumor volume of interest for ^{18}F-FDG and ^{18}F-FDOPA showed decreased overall uptake across imaging time for treated mice (**Figure 2.3C-D**). Interestingly, treatment did not affect time to steady state in ^{18}F-FDOPA TACs, suggesting that melphalan therapy did not impact the overall uptake mechanism and washout kinetics in the tumors.

Table 2.1: Summary of ^{18}F-FDOPA and ^{18}F-FDG measurements

		Treated (n=7) (Mean ± SEM)	Untreated (n=6) (Mean ± SEM)	Untreated : Treated (Mean ± SEM)
Avidity	TLA	13.07 ± 5.89	603.9 ± 165.9	46.21 ± 24.37
	TLG	44.92 ± 12.05	2329 ± 532.1	51.85 ± 18.27
MTV (mm^3)	^{18}F-FDOPA	22.16 ± 7.67	636 ± 194.5	28.7 ± 13.22
	^{18}F-FDG	28.81 ± 5.35	416.1 ± 182.5	14.44 ± 6.88
SUV$_{Max}$	^{18}F-FDOPA	0.70 ± 0.13	1.48 ± 0.17	2.11 ± 0.46
	^{18}F-FDG	2.84 ± 0.65	7.03 ± 0.84	2.47 ± 0.64
Total Uptake	^{18}F-FDOPA	53.06 ± 8.33	118.9 ± 8.55	2.24 ± 0.39
	^{18}F-FDG	138.8 ± 28.18	483.5 ± 58.98	3.48 ± 0.83
Structural Tumor Volume (mm^3)		78.31 ± 53.6	771.2 ± 291.7	9.85 ± 7.70

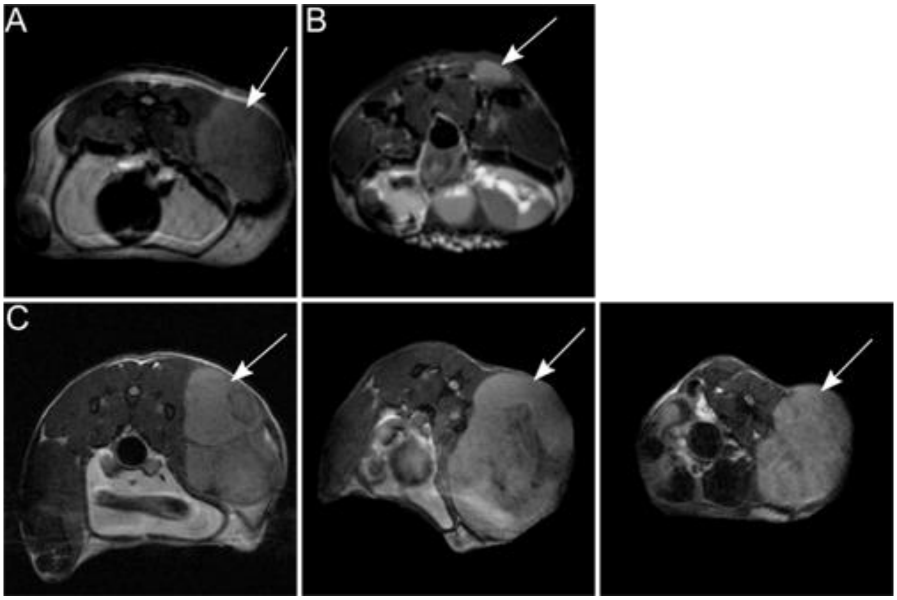

Figure 2.2: Representative T_2-weighted MRI transverse images of (A) untreated, (B) week 2-4 treated, and (C) treated weeks 3-5 post tumor implantation, at the (left) pre-treatment baseline and weeks (middle) 4 and (right) 5.

Avidity and uptake of both ^{18}F-FDOPA and ^{18}F-FDG were reduced in the treated tumors. There was a larger reduction in ^{18}F-FDOPA MTV (28.7 ± 13.2-fold) than ^{18}F-FDG MTV (14.4 ± 6.9-fold), although this difference in MTV reduction did not translate to significant correlation between MTV and structural tumor volume. Reductions in TLA and TLG were similar in treated tumors (**Figure 2.4A**). Overall ^{18}F-FDG SUV$_{max}$ was higher in both untreated and treated tumors than ^{18}F-FDOPA SUV$_{max}$ untreated and treated tumors (**Figure 2.4B; Table 2.1**). ^{18}F-FDOPA total uptake and maximal uptake metrics fell within control tissue levels upon melphalan treatment, as measured relative to bone marrow and muscle, while ^{18}F-FDG uptake remained significantly higher relative to control tissue within the tumor (**Figure 2.4C**). These results suggest that changes in ^{18}F-FDOPA uptake may be more specific to melphalan-mediated reduction in tumor size than ^{18}F-FDG for this tumor model.

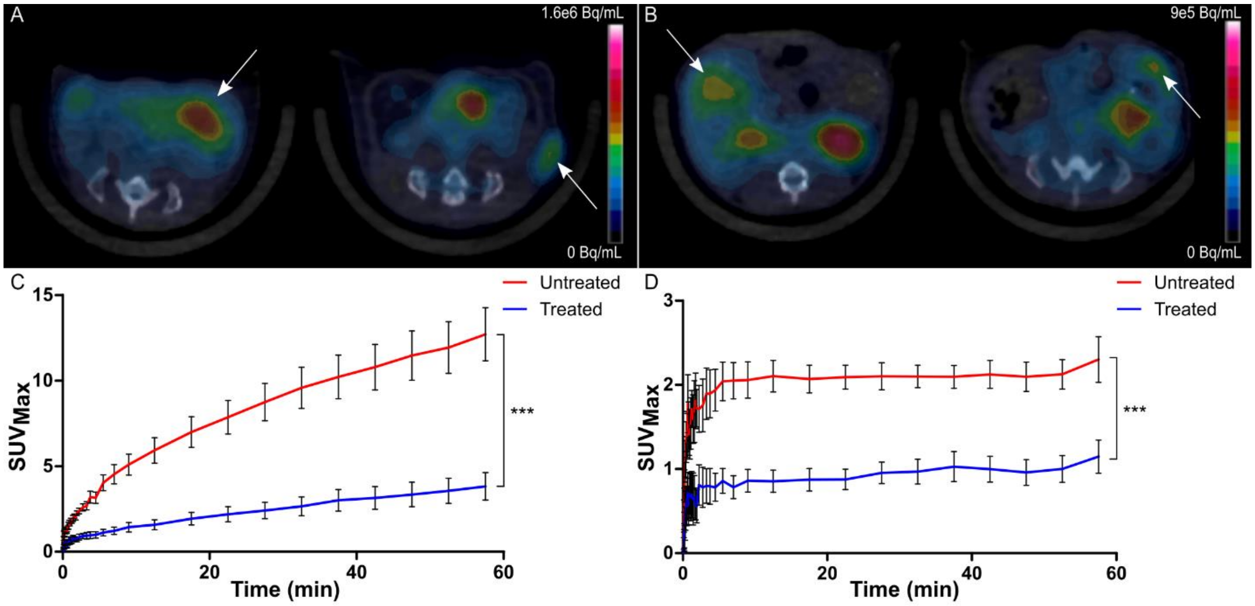

Figure 2.3: Localization of tumor and average time activity profile in treated and untreated 5TGM1 tumor-bearing C57Bl/KaLwRij mice imaged with ^{18}F-FDG and ^{18}F-FDOPA PET/CT. Representative co-registered PET/CT transverse view of (left) untreated and (right) treated tumors in dynamic (A) ^{18}F-FDG and (B) ^{18}F-FDOPA imaging. TACs from (C) ^{18}F-FDG and (D) ^{18}F-FDOPA are displayed (mean ± SEM at each time point), with statistical significance calculated using the 2-way ANOVA with repeated measures (*** $p < 0.001$).

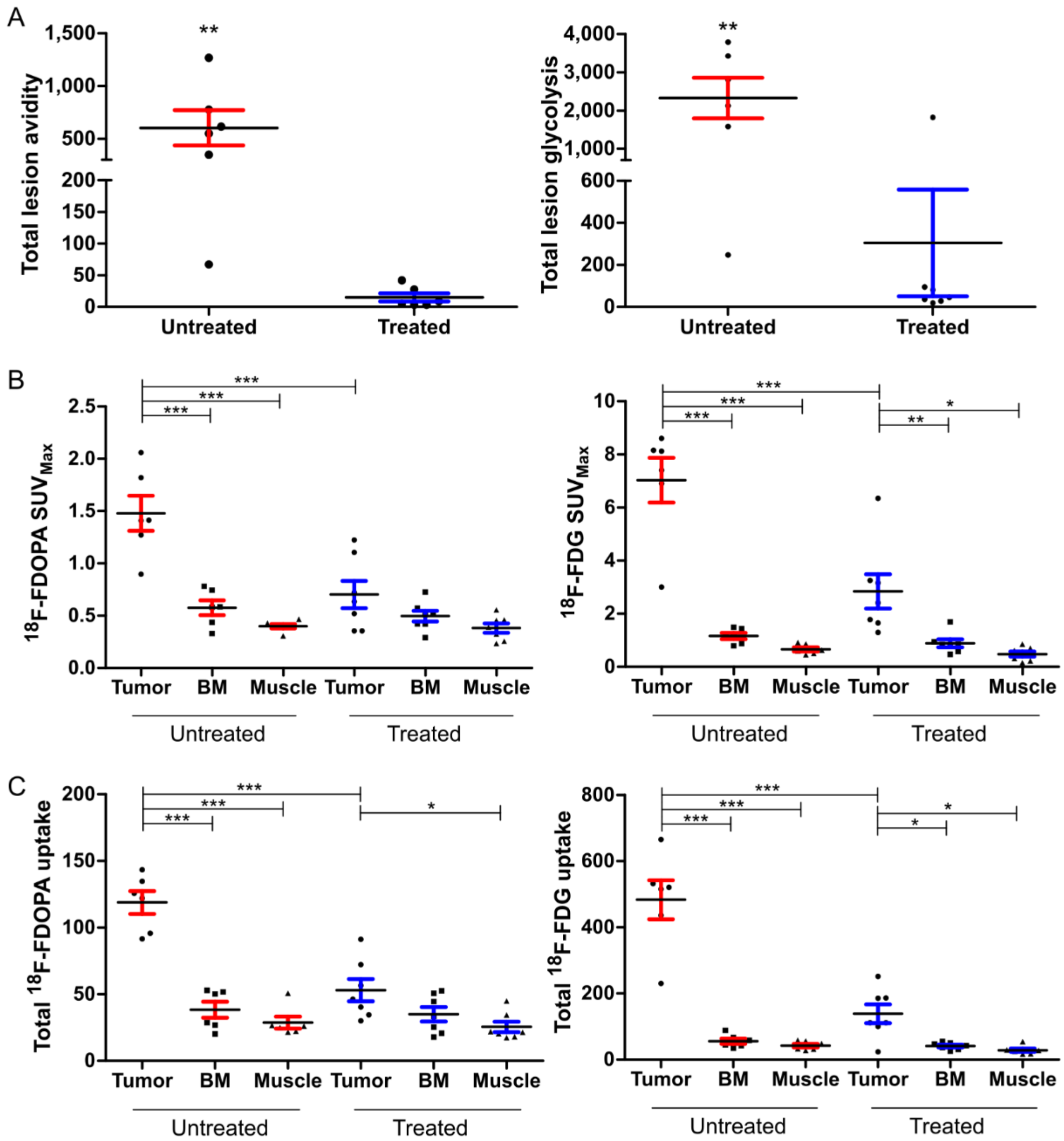

Figure 2.4: Distribution of ^{18}F-FDG and ^{18}F-FDOPA uptake and avidity metrics in treated and untreated 5TGM1 tumor-bearing C57Bl/KaLwRij mice. Scatter plots with mean and SEM distributions are displayed for (A) TLA (left) and TLG (right), (B) SUV_{Max}, and (C) total uptake for ^{18}F-FDOPA (left) and ^{18}F-FDG (right). Statistical significance between treated and untreated cohorts for TLA and TLG was calculated using the two-tailed Student's t-test, while 1-way ANOVA with the Bonferroni multiple comparison post-test was used to assess statistical significance between groups and tissue for SUV_{Max} and total uptake ($* p < 0.05$, $** p < 0.01$, and $*** p < 0.001$).

^{18}F-FDOPA measurements were also assessed against ^{18}F-FDG using Lin's concordance correlation coefficients. Avidity and MTV in the treated cohort were moderately concordant, while SUV_{Max} and total tracer uptake demonstrated poor agreement (**Table 2.2**). Interestingly, ^{18}F-FDOPA TLA and total uptake were correlated more strongly post therapy to ^{18}F-FDG, while the concordance of MTV and SUV_{max} between ^{18}F-FDOPA and ^{18}F-FDG was relatively unaffected. The lack of concordance between ^{18}F-FDOPA and ^{18}F-FDG in the SUV_{Max} and total uptake is likely linked to the difference in uptake mechanisms, while moderate agreement between MTV and avidity indicated similar global effects on metabolism in the setting of effective therapy.

Table 2.2: Summary of Lin's correlation coefficient relative to ^{18}F-FDG-PET/CT parameters

	Treated (n=7) Mean (5% - 95% CI)	Untreated (n=6) Mean (5% - 95% CI)
Avidity	0.41 (0.04 – 0.68)	0.16 (-0.08 – 0.4)
MTV	0.64 (-0.01 – 0.91)	0.55 (0.01 – 0.84)
SUV_{Max}	0.03 (-0.11 – 0.16)	0.03 (-0.03 – 0.09)
Total Uptake	0.21 (-0.02 – 0.42)	0.02 (-0.02 – 0.06)

We next performed weekly ^{18}F-FDOPA and ^{18}F-FDG-PET/CT and MRI to study the effect of therapy on established tumors (**Figure 2.1B**). T_2-weighted MRI indicated minimal structural tumor volume reduction throughout the therapy regimen (**Figure 2.2C**). ^{18}F-FDG uptake was significantly reduced in week 1 of therapy, with a return to pretreatment levels during week 2 (**Figure 2.5A; Figure 2.6A**). TLG (1.7 ± 0.4-fold), SUV_{Max} (2.1 ± 0.4-fold), and total ^{18}F-FDG uptake (2.1 ± 0.4-fold) also increased by week 2 of therapy, suggesting a rebound of glucose-avid tumor cells (**Figure 2.6B-D**). By contrast, ^{18}F-FDOPA kinetics were unaffected by the therapy regimen (**Figure 2.5B; Figure 2.6A**). There was an increase in TLA (2.4 ± 0.9-fold) between the pretreatment baseline and week 1, which remained consistent at week 2 (0.8 ± 0.2-fold relative to week 1) (**Figure 2.6B**). There was no corresponding change in SUV_{Max} or total ^{18}F-FDOPA uptake (**Figure 2.6C-D**). These results suggested that treatment of established tumors with melphalan may result in the stabilization of the structural and metabolic tumor volumes. Additionally, the lack of correlation between ^{18}F-FDOPA and ^{18}F-FDG uptake indicated that acute changes in glucose metabolism are independent of changes in the transport and intracellular metabolism of the amino acid ^{18}F-FDOPA.

Figure 2.5: Representative maximum intensity projections of longitudinal (A) ^{18}F-FDG and (B) ^{18}F-FDOPA-PET/CT at the pretreated baseline and weeks 1 and 2 during melphalan therapy.

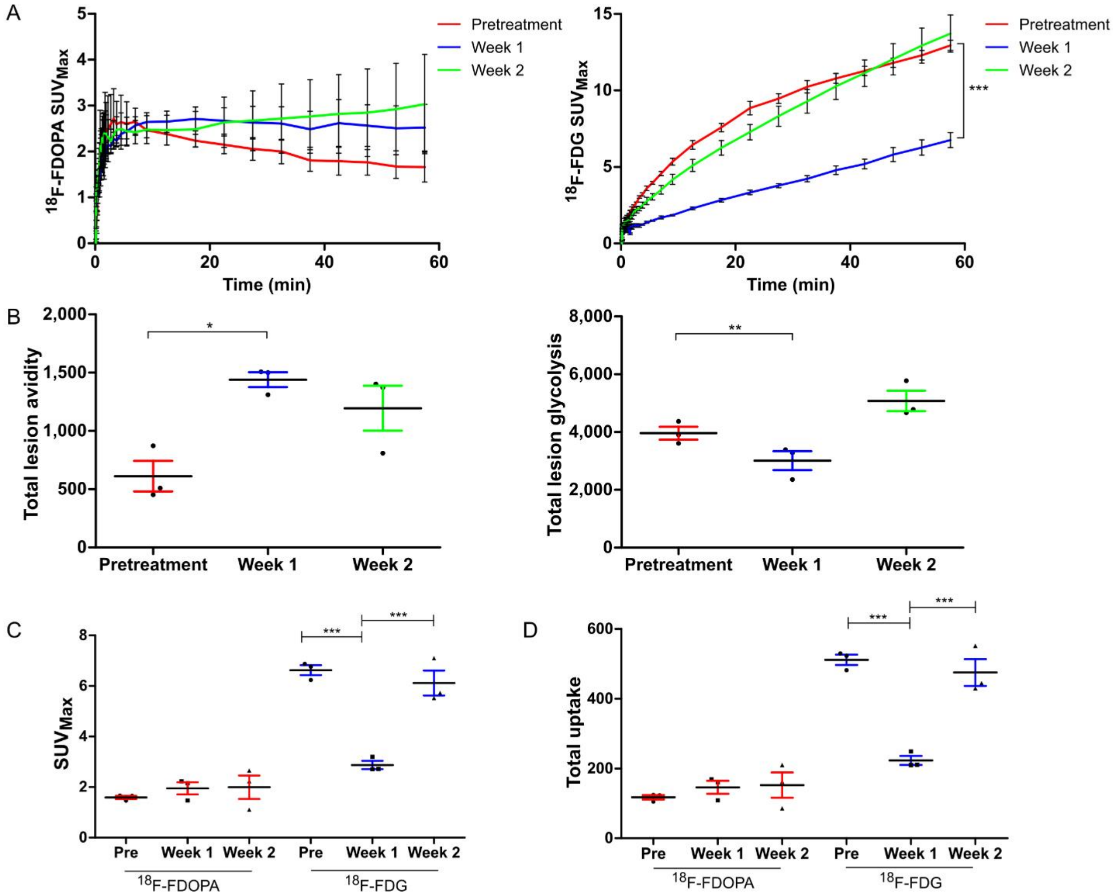

Figure 2.6: Distribution of ^{18}F-FDOPA and ^{18}F-FDG uptake metrics during longitudinal treatment and imaging. (A) TACs for ^{18}F-FDOPA (left) and ^{18}F-FDG (right), with statistical significance calculated with 2-way ANOVA with repeated measures and Bonferroni comparisons post-test. (B) TLA (left) and TLG (right) were calculated for each week, as were (C) SUV_{Max} and (D) total uptake from ^{18}F-FDOPA and ^{18}F-FDG TACs. Time points (weeks 1 and 2) were relative to pre-treatment baseline (week 3 post tumor implantation). Statistical significance for the individual comparisons was calculated using 1-way ANOVA with Tukey post-hoc test (*$p<0.05$, **$p<0.01$, ***$p<0.001$).

Immunohistochemistry was performed on tissue from both treatment groups to evaluate changes in LAT1 and GLUT1 transporter expression. Changes in LAT1 expression were modulated by both tumor size and therapy. Mice in the melphalan-treated established tumor cohort (week 3 treatment group) had reduced LAT1 (**Figure 2.7C top**) surface density relative to the treatment regimen started week 2 post tumor implantation (week 2 treatment group) and the untreated tumor (**Figure 2.7A-B top**). The high LAT1 density in the week 2 treatment group relative to the untreated tumors could be attributed to the smaller tumor size and increased tumor vascular density. Indeed, LAT1 and GLUT1 expression was generally concentrated near blood vessels, as confirmed by CD31 staining (**Figure 2.8A-B top**). The relative lack of LAT1 signal in the untreated tumor may be linked to the heterogeneous distribution of viable GFP-expressing tumor cells within the tumor mass.

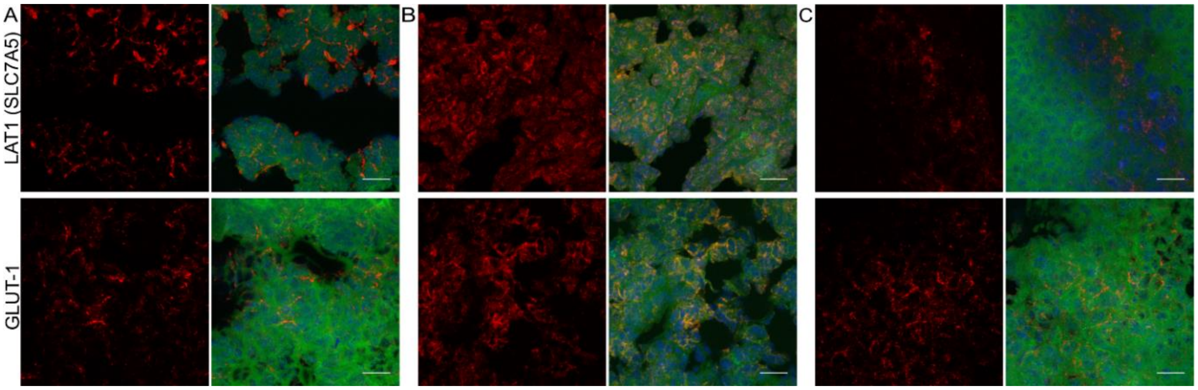

Figure 2.7: Immunohistochemistry of LAT1 (top) and GLUT1 (bottom) expression for (A) untreated and treated tumors with initialization of melphalan therapy at (B) weeks two and (C) three post tumor implantation. Expression for each stain was visualized as a maximum intensity projection (63X magnification; 20µm scale bar) separately and as a composite with GFP (green) and DAPI nuclear stain (blue).

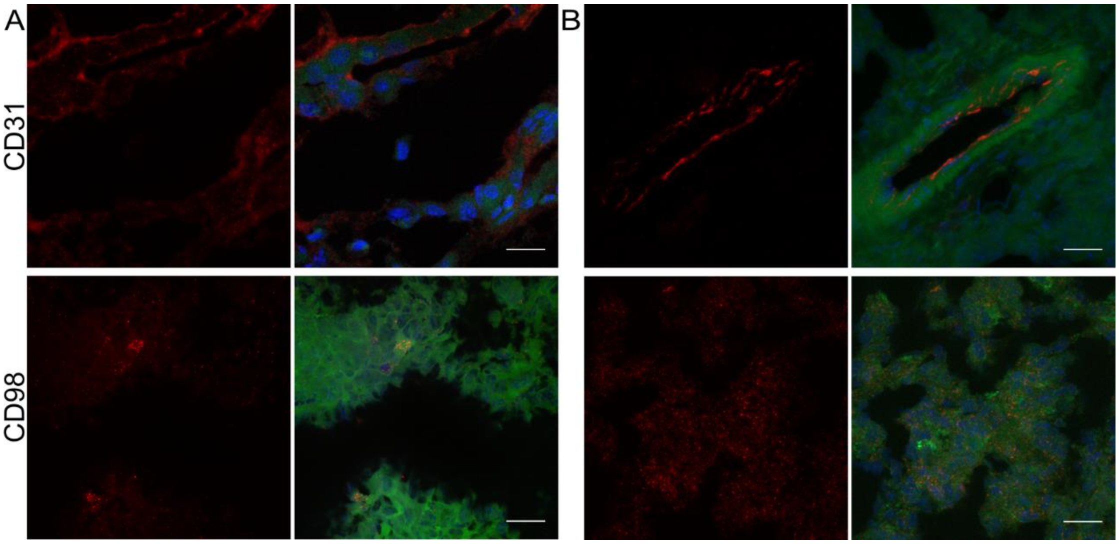

Figure 2.8: Immunohistochemistry of CD31 (top) and CD98 (bottom) for representative (A) untreated and (B) treated tumors with initialization of melphalan therapy at week 2 post tumor implantation. Expression for each stain was visualized as a maximum intensity projection (63X magnification; 20µm scale bar) separately and as a composite with GFP (green) and DAPI nuclear stain (blue).

2.5 Discussion

^{18}F-FDOPA is an aromatic amino acid PET tracer that is effective for imaging gliomas and neuroendocrine tumors (*16,17*). Dimitrakopoulou-Strauss *et al* showed that ^{18}F-FDOPA and ^{18}F-FDG uptake provided complementary detection of metastatic melanoma in pretreated patients (*22*). ^{18}F-FDOPA uptake by cancer cells is thought to be primarily mediated by LAT1, making it a promising candidate for imaging LAT1 activity *in vivo*. Since melphalan uptake is also mediated by LAT1, we used ^{18}F-FDOPA-PET as a surrogate reporter of melphalan therapy efficacy in a preclinical, immunocompetent MM model. We evaluated ^{18}F-FDOPA and ^{18}F-FDG uptake parameters, including TLA, MTV, and SUV$_{Max}$ *in vivo* in unilateral subcutaneously implanted 5TGM1 tumors in C57Bl/KaLwRij mice, which served as a model for extramedullary myeloma. Importantly, uptake of ^{18}F-FDOPA correlated strongly to LAT1 surface expression and showed a significant therapy-induced decrease in SUV_{Max}, lesion avidity, and total uptake relative to untreated tumor.

Preclinical ^{18}F-FDOPA-PET/CT showed demonstrably different tumor uptake in the untreated and the two therapy groups. Immunohistochemistry of the week 2 treatment group suggested that decreasing tumor sizes and increased viable tumor fraction were linked to increased LAT1 expression (**Figure 2.7A-B top**). To further validate changes in expression of LAT1, CD98 staining was performed. It should be noted, however, that CD98 also forms heterodimers with other amino acid transporters, including members of the LAT family(*11*). Additionally, CD98 expression is implicated in increased vascular density (**Figure 2.8A-B bottom**) (*23*). The correlation between vascular density and LAT1 expression is corroborated by ^{11}C-methionine preclinical PET studies of gliomas and brain tumors (*24*). ^{18}F-FDOPA metrics also correlated with melphalan sensitivity, with moderate concordance in MTV to the ^{18}F-FDG-PET clinical reference standard (**Table 2.2**). The reduction in ^{18}F-FDOPA uptake indicated the sensitivity of ^{18}F-FDOPA-PET/CT to melphalan cytotoxicity.

There was a larger effect on total uptake and SUV_{Max} for ^{18}F-FDG in response to aggressive melphalan therapy (**Figure 2.4B-C**). The 5TGM1 cell line is highly glucose avid and aggressive relative to several other human and murine myeloma cell lines. This avidity, coupled with minimal GLUT1 surface density differences in untreated and treated tumors, may explain the differences in overall uptake of ^{18}F-FDG relative to ^{18}F-FDOPA in this tumor model. ^{18}F-FDG SUV_{Max} and total uptake was also significantly higher in the treated tumor relative to non-tumor tissue. This effect may be partially explained by the recruitment of glucose avid macrophages and other immune cells to the tumor by therapy-induced inflammation. Nevertheless, ^{18}F-FDG-PET/CT provided accurate identification of overall response, while ^{18}F-FDOPA-PET/CT highlighted melphalan-sensitive tumor populations and showed a greater reduction in MTV in the treatment group compared to the untreated tumors than did ^{18}F-FDG.

The differences in ^{18}F-FDOPA and ^{18}F-FDG uptake induced by the aggressive therapy regimen may be overstated by several factors, including variable tumor viability, immunologic response, and the homogeneous expression of LAT1 in the viable tumor volume. To address these concerns, we performed longitudinal ^{18}F-FDOPA and ^{18}F-FDG-PET/CT on established tumors treated with melphalan (**Figure 2.1B**). There was no significant difference in ^{18}F-FDOPA MTV, SUV_{Max}, or total uptake observed during the imaging period (**Figure 2.5B; Figure 2.6**). There was a 2.4-fold increase in TLA between the baseline and first week of therapy, which remained unchanged at the second week (**Figure 2.6B**). Indeed, immunohistochemistry showed that LAT1 expression in this treatment group did not differ qualitatively from the untreated tumor, which suggests therapy-induced stabilization of LAT1 expression within the tumor environment (**Figure 2.7C**). By contrast, ^{18}F-FDG SUV_{Max} and total uptake rebounded to pre-treatment levels after the first week of therapy, indicating reduction in therapy killing effect by the second week and stabilized tumor viability (**Figure 2.6C-D**). These results suggest that functional imaging with ^{18}F-FDOPA and ^{18}F-FDG PET/CT may be linked to tumor viability and melphalan therapy response.

Use of indirect metabolic markers such as lesion avidity and radiotracer uptake have been established in the literature as potential parameters sensitive to changes in cancer staging. TLA and TLG, while derived from similar SUV data, provided different results from total uptake, due to the selective volumetric information contained within the MTV. TLA is a crucial semi-quantitative parameter that may provide a surrogate measurement for viable tumor fraction. TLG is a more mechanistic measurement that represents the tracer uptake mediated by the glucose transport proteins and the subsequent intracellular trapping of ^{18}F-FDG following phosphorylation by hexokinases. While phosphorylated ^{18}F-FDG is unable to enter glycolysis further downstream, TLG can provide information on the changing GLUT1 mediated metabolism during disease progression and following therapeutic intervention. Indeed, McDonald *et al* have shown that ^{18}F-FDG TLG, MTV, SUV_{Max}, and the number of focal lesions strongly correlated to

MM stage and progression-free and overall survival rates (*25*). Similarly, our results highlight the discordance in the changes in TLA and TLG in response to melphalan therapy in the established tumors. Therefore, ^{18}F-FDG and ^{18}F-FDOPA may provide an assessment of tumor response to melphalan during early and late stages, respectively.

This study was a proof of concept investigation into ^{18}F-FDOPA-PET imaging of myeloma and the correlation between ^{18}F-FDOPA to melphalan therapeutic efficacy in an extramedullary myeloma tumor model. There are several promising results from this study, including the correlation between ^{18}F-FDOPA and ^{18}F-FDG uptake with tumor viability and early response to melphalan therapy, respectively. Imaging in other human and murine myeloma cell lines and animal models with different LAT1 expression and melphalan sensitivity would provide additional corroboration for the trends seen within these data. Efflux transporters are predominantly linked to melphalan resistance in *in vitro* studies of melphalan-resistant myeloma cell lines (*26*). Therefore, determining the expression of efflux transporters at various time-points during melphalan therapy would also provide important information about treatment-mediated transient changes in influx and efflux transporters. Finally, further investigation into ^{18}F-FDOPA uptake and washout mechanisms with metabolite fate analyses and competitive inhibition of ^{18}F-FDOPA intracellular uptake can provide the means for developing strong predictive models of melphalan sensitivity with ^{18}F-FDOPA-PET/CT.

2.6 Conclusion

This study represents, to date, one of the first investigations linking amino acid-based imaging in MM to therapy response, *via* the correlation of ^{18}F-FDOPA-PET/CT to melphalan sensitivity and LAT1 expression. ^{18}F-FDOPA-PET/CT provided viable and complementary imaging of MM and melphalan therapy efficacy in this tumor model. Finally, uptake of ^{18}F-FDG and ^{18}F-FDOPA in established tumors were discordant early after treatment initiation, indicating the tracers' independent mechanisms and their individual applications for assessing response to different stages of melphalan therapy.

2.7 References

1. Hathi DK, DeLassus EN, Achilefu S, McConathy J, Shokeen M. Imaging Melphalan Therapy Response in Preclinical Extramedullary Multiple Myeloma with 18F-FDOPA and 18F-FDG PET. *J Nucl Med.* 2018;59:1551-1557.

2. Palumbo A, Sezer O, Kyle R, et al. International Myeloma Working Group guidelines for the management of multiple myeloma patients ineligible for standard high-dose chemotherapy with autologous stem cell transplantation. *Leukemia.* 2009;23:1716-1730.

3. Waage A, Gimsing P, Fayers P, et al. Melphalan and prednisone plus thalidomide or placebo in elderly patients with multiple myeloma. *Blood.* 2010;116:1405-1412.

4. Facon T, Mary JY, Hulin C, et al. Melphalan and prednisone plus thalidomide versus melphalan and prednisone alone or reduced-intensity autologous stem cell transplantation in elderly patients with multiple myeloma (IFM 99–06): a randomised trial. *Lancet.* 2007;370:1209-1218.

5. Kim DK, Kanai Y, Choi HW, et al. Characterization of the system L amino acid transporter in T24 human bladder carcinoma cells. *Biochim Biophys Acta Biomembr.* 2002;1565:112-122.

6. Lin J, Raoof DA, Thomas DG, et al. l-Type Amino Acid Transporter-1 Overexpression and Melphalan Sensitivity in Barrett's Adenocarcinoma. *Neoplasia.* 2004;6:74-84.

7. Isoda A, Kaira K, Iwashina M, et al. Expression of L-type amino acid transporter 1 (LAT1) as a prognostic and therapeutic indicator in multiple myeloma. *Cancer Sci.* 2014;105:1496-1502.

8. Bhutia YD, Babu E, Ramachandran S, Ganapathy V. Amino Acid transporters in cancer and their relevance to "glutamine addiction": novel targets for the design of a new class of anticancer drugs. *Cancer Res.* 2015;75:1782-1788.

9. Yanagida O, Kanai Y, Chairoungdua A, et al. Human L-type amino acid transporter 1 (LAT1): characterization of function and expression in tumor cell lines. *Biochim Biophys Acta Biomembr.* 2001;1514:291-302.

10. Napolitano L, Scalise M, Galluccio M, Pochini L, Albanese LM, Indiveri C. LAT1 is the transport competent unit of the LAT1/CD98 heterodimeric amino acid transporter. *Int J Biochem Cell Biol.* 2015;67:25-33.

11. Wagner CA, Lang F, Broer S. Function and structure of heterodimeric amino acid transporters. *Am J Physiol Cell Physiol.* 2001;281:C1077-1093.

12. Altman BJ, Stine ZE, Dang CV. From Krebs to clinic: glutamine metabolism to cancer therapy. *Nat Rev Cancer.* 2016;16:749.

13. Agarwal A, Chirindel A, Shah BA, Subramaniam RM. Evolving role of FDG PET/CT in multiple myeloma imaging and management. *Am J Roentgenol.* 2013;200:884-890.

14. Cavo M, Terpos E, Nanni C, et al. Role of 18F-FDG PET/CT in the diagnosis and management of multiple myeloma and other plasma cell disorders: a consensus statement by the International Myeloma Working Group. *The Lancet Oncology.* 2017;18:e206-e217.

15. Youland RS, Kitange GJ, Peterson TE, et al. The role of LAT1 in (18)F-DOPA uptake in malignant gliomas. *J Neurooncol.* 2013;111:11-18.

16. Schwarzenberg J, Czernin J, Cloughesy TF, et al. Treatment response evaluation using 18F-FDOPA PET in patients with recurrent malignant glioma on Bevacizumab therapy. *Clin Cancer Res.* 2014.

17. Becherer A, Szabó M, Karanikas G, et al. Imaging of advanced neuroendocrine tumors with 18F-FDOPA PET. *J Nucl Med.* 2004;45:1161-1167.

18. Mori Y, Shimizu N, Dallas M, et al. Anti-α4 integrin antibody suppresses the development of multiple myeloma and associated osteoclastic osteolysis. *Blood.* 2004;104:2149-2154.

19. Ulaner GA, Goldman DA, Corben A, et al. Prospective Clinical Trial of (18)F-Fluciclovine PET/CT for Determining the Response to Neoadjuvant Therapy in Invasive Ductal and Invasive Lobular Breast Cancers. *J Nucl Med.* 2017;58:1037-1042.

20. Vanderhoek M, Perlman SB, Jeraj R. Impact of the Definition of Peak Standardized Uptake Value on Quantification of Treatment Response. *J Nucl Med.* 2012;53:4-11.

21. Zaidi AU, Enomoto H, Milbrandt J, Roth KA. Dual Fluorescent In Situ Hybridization and Immunohistochemical Detection with Tyramide Signal Amplification. *J Histochem Cytochem.* 2000;48:1369-1375.

22. Dimitrakopoulou-Strauss A, Strauss LG, Burger C. Quantitative PET studies in pretreated melanoma patients: a comparison of 6-[18F]fluoro-L-dopa with 18F-FDG and (15)O-water using compartment and noncompartment analysis. *J Nucl Med.* 2001;42:248-256.

23. Liao Z, Cantor JM. Endothelial cells require CD98 for efficient angiogenesis-brief report. *Arterioscler Thromb Vasc Biol.* 2016;36:2163-2166.

24. Okubo S, Zhen HN, Kawai N, Nishiyama Y, Haba R, Tamiya T. Correlation of L-methyl-11C-methionine (MET) uptake with L-type amino acid transporter 1 in human gliomas. *J Neurooncol.* 2010;99:217-225.

25. McDonald JE, Kessler MM, Gardner MW, et al. Assessment of total lesion glycolysis by (18)F FDG PET/CT significantly improves prognostic value of GEP and ISS in myeloma. *Clin Cancer Res.* 2017;23:1981-1987.

26. Kuhne A, Tzvetkov MV, Hagos Y, Lage H, Burckhardt G, Brockmoller J. Influx and efflux transport as determinants of melphalan cytotoxicity: Resistance to melphalan in MDR1 overexpressing tumor cell lines. *Biochem Pharmacol.* 2009;78:45-53.

Chapter 3: Near-infrared imaging of VLA-4 expression for monitoring bortezomib efficacy in preclinical MM

3.1 Overview

In this study, the uptake of the near-infrared contrast agent LLP2A-Cy5 was correlated to bortezomib therapy response in an intramedullary MM tumor model. Bortezomib reduces myeloma cell adhesion to the bone marrow stroma, *via* the downregulation of the very-late antigen-4 (VLA-4) integrin. VLA-4 is a bidirectional heterodimeric integrin receptor that is overexpressed in its active conformation on myeloma cells and is implicated in several MM pathogenic pathways. We have previously demonstrated VLA-4 overexpression as a promising imaging biomarker for monitoring MM disease progression using a high affinity peptidomimetic ligand, LLP2A, conjugated to a nuclear contrast agent. Here, we proposed to use uptake of the near-infrared fluorescent analog LLP2A-Cy5 for imaging activated VLA-4 overexpression in response to bortezomib therapy in syngeneic, intramedullary MM.

Our results showed significant decrease in LLP2A-Cy5 uptake in the tumor-bearing hematopoietic tissue following bortezomib therapy. Flow cytometry and *ex vivo* tissue biodistribution identified reduction in LLP2A-Cy5$^+$ populations across most tissue, indicating the anti-inflammatory behavior of bortezomib. This study suggests that LLP2A-Cy5 optical imaging can provide an economical and high-throughput alternative to nuclear imaging for imaging activated VLA-4 expression and bortezomib therapy response. The material in this chapter is part of a prepared manuscript submission to the journal *Blood*.

3.2 Introduction

In multiple myeloma (MM) clinical care, the proteasome inhibitor bortezomib is a key therapeutic agent in front-line regimens. Bortezomib therapy modulates bone marrow (BM) remodeling by inhibiting the myeloma cells’ interactions with the BM microenvironment. One of the main molecules affected by this interruption is the very-late antigen-4 (VLA-4; $\alpha_4\beta_1$ integrin, also known as CD49d/CD29). VLA-4 is a bidirectional integrin receptor overexpressed on myeloma cells in the high affinity activated conformation and is strongly implicated in key signaling pathways of disease pathogenesis, including cell proliferation, trafficking, and adhesion-mediated drug resistance (*1,2*). The activated form of VLA-4 binds to fibronectin and the vascular cell adhesion marker-1 expressed on the surface of BM stromal cells, resulting in increased cell adhesion and survival within the BM niche (*2,3*). Bortezomib inhibits several oncogenic pathways, including NF-κB and MAPK cascades, resulting in increased osteoclast apoptosis and the downregulation of several inflammatory and angiogenesic cytokines and factors (*4-6*). Bortezomib abrogates BM adhesion by downregulating production of the α_4 subunit in the VLA-4 heterodimer (*1*). Thus, bortezomib efficacy may be linked to VLA-4 expression in myeloma cells.

We have previously demonstrated the affinity of the peptidomimetic ligand LLP2A for the activated conformation of VLA-4 in preclinical extramedullary and intramedullary MM (*7-9*). In particular, VLA-4 overexpression was used to monitor MM disease progression in the BM. To study *in vivo* and *ex vivo* overexpression of VLA-4 in an economical and high-throughput manner, we developed a near-infrared (NIR) fluorescent imaging agent by conjugating LLP2A to the NIR cyanine dye Cy5 (*9*). Melanin, hemoglobin, and other endogenous chromophores have reduced absorption and autofluorescence in the NIR window (650-900nm), resulting in improved depth penetration (*10*). Here, we have demonstrated LLP2A-Cy5 as a surrogate for activated VLA-4 overexpression in syngeneic, intramedullary MM tumors in an immunocompetent mouse strain. The correlation between bortezomib treatment and activated VLA-4 expression was also studied.

3.3 Materials and Methods

3.3.1 Cell culture and reagents

5TGM1-GFP cells (5TGM1; kind gift from Dr. K. N. Weilbaecher, Washington University, Department of Medicine) were maintained at 10^6 cells/mL in Iscove's Modified Dulbecco Medium supplemented with 10% v/v fetal bovine serum and 1% penicillin/streptomycin (all from Thermo Fisher Scientific, MA, USA). Bortezomib (Sigma Aldrich, MO, USA) doses were prepared prior to each therapy injection. LLP2A-PEG4-Cy5 (LLP2A-Cy5) and scrambled LLP2A-PEG4-Cy5 (scLLP2A-Cy5) were synthesized as previously described (*9*).

3.3.2 In vitro LLP2A-Cy5 uptake and specificity

5TGM1 cells were plated on 35mm glass bottom MatTek dishes pre-coated with poly-D-lysine (glass no. 1.5; MatTek Corporation, MA) at 10^5 cells/cm^2, and allowed to attach for 1 h at 37^{o}C. Cells were incubated with 1 µM of the Cy5-labelled probes at 4^{o}C for 15 min, and at 37^{o}C for 2.5 h to assess cell surface binding specificity and cellular internalization, respectively. 10 µg/L Hoechst 34580 (Invitrogen, CA) was added for the last 15 min of incubation to counterstain cell nuclei. Fluorescence confocal microscopy was performed on a Nikon A1Rsi confocal microscope (Nikon Corporation, Tokyo, Japan) with 60X and 100X oil immersion objectives using excitation-emission at 405-450/40 nm (Hoechst 34580), 488-530/20 nm (GFP), and 640-660/20 nm (Cy5).

3.3.3 Saturation binding assay

Selective affinity was determined with fluorescence activated cell sorting (FACS). $1.5x10^5$ 5TGM1-GFP cells were incubated with varying concentrations of LLP2A-Cy5, with or without 100nM BIO5192 (Tocris Bioscience, Bristol, United Kingdom), which was used to assess nonspecific binding. BIO5192 is a highly specific inhibitor for activated VLA-4 (*11*). Samples were analyzed on a Beckman Coulter Gallios flow cytometer and data were analyzed using FlowJo software (TreeStar, Ashland, OR). Total and nonspecific binding coefficients (dissociation constant (K_d) and receptor density (B_{max})) were calculated by fitting mean fluorescence intensity (MFI) versus LLP2A-Cy5 concentration using Prism 5.0 (GraphPad Software, Inc., CA).

3.3.4 Tumor model and bortezomib therapy

All animal studies were conducted according to protocols approved by the Washington University Institutional Animal Care and Use Committee. Mice were anesthetized under 2% v/v isoflurane/100% O_2 prior to tumor implantation. Female 4-8 week old C57Bl/KaLwRij mice were injected intravenously with 10^6 5TGM1 cells, *via* the lateral tail vein.

Tumor-bearing animals were divided into untreated (n=5) and treated (n=3) groups. Bortezomib therapy was administered intraperitoneally at 1 mg/kg twice a week beginning on day 14 post tumor implantation (*12*). Untreated animals received vehicle control on the same schedule.

3.3.5 In vivo NIR imaging

Prior to imaging, hair was removed by gentle clipping and depilatory cream to improve light transmission. Mice were imaged before and after 18-24 h after intravenous injection of 100 µL of 25 µM LLP2A-Cy5 in 5% v/v DMSO/H_2O using the Optix MX3 time-domain diffuse optical imaging system (Advanced Research Technologies, Montreal, Canada) as previously described (*13*). The images were background subtracted to reduce the effects of autofluorescence.

3.3.6 Statistical analysis

Statistical analysis was performed using GraphPad Prism 7.0 (GraphPad, CA, USA). One-way analysis of variance (ANOVA) with Sidak multiple comparisons test was used to assess statistical significance between multiple groups, while the Student's two-tailed *t*-test was used for comparisons between two groups. A *p*-value less than 0.05 was defined as statistically significant.

3.4 Results

The specificity and binding affinity of LLP2A-Cy5 for activated VLA-4 expression on cells was tested *in vitro* in 5TGM1 cells. 5TGM1 cells were first incubated with LLP2A-Cy5 at 4^{o}C to reduce non-specific uptake and binding (**Figure 3.1A**). Cell surface fluorescence was significantly reduced when 5TGM1 cells were incubated with the scrambled peptidomimetic (5.86 ± 2.25-fold) and 100-fold excess unlabeled LLP2A blocking (5.01 ± 2.04-fold) (**Figure 3.1B, C**; **Figure 3.2A**). Incubation at 37^{o}C for 2.5 h did not result in an increase in intracellular uptake, with predominantly cell surface signal (Figure 1D). The binding specificity was further corroborated using saturation binding, resulting in K_d of 117.7 ± 8.69 nM (**Figure 3.2B**). Minimal nonspecific binding (NS, 0.01 ± 0.003) was observed in the presence of BIO5192. These results indicate that LLP2A-Cy5 is specific to VLA-4 expression.

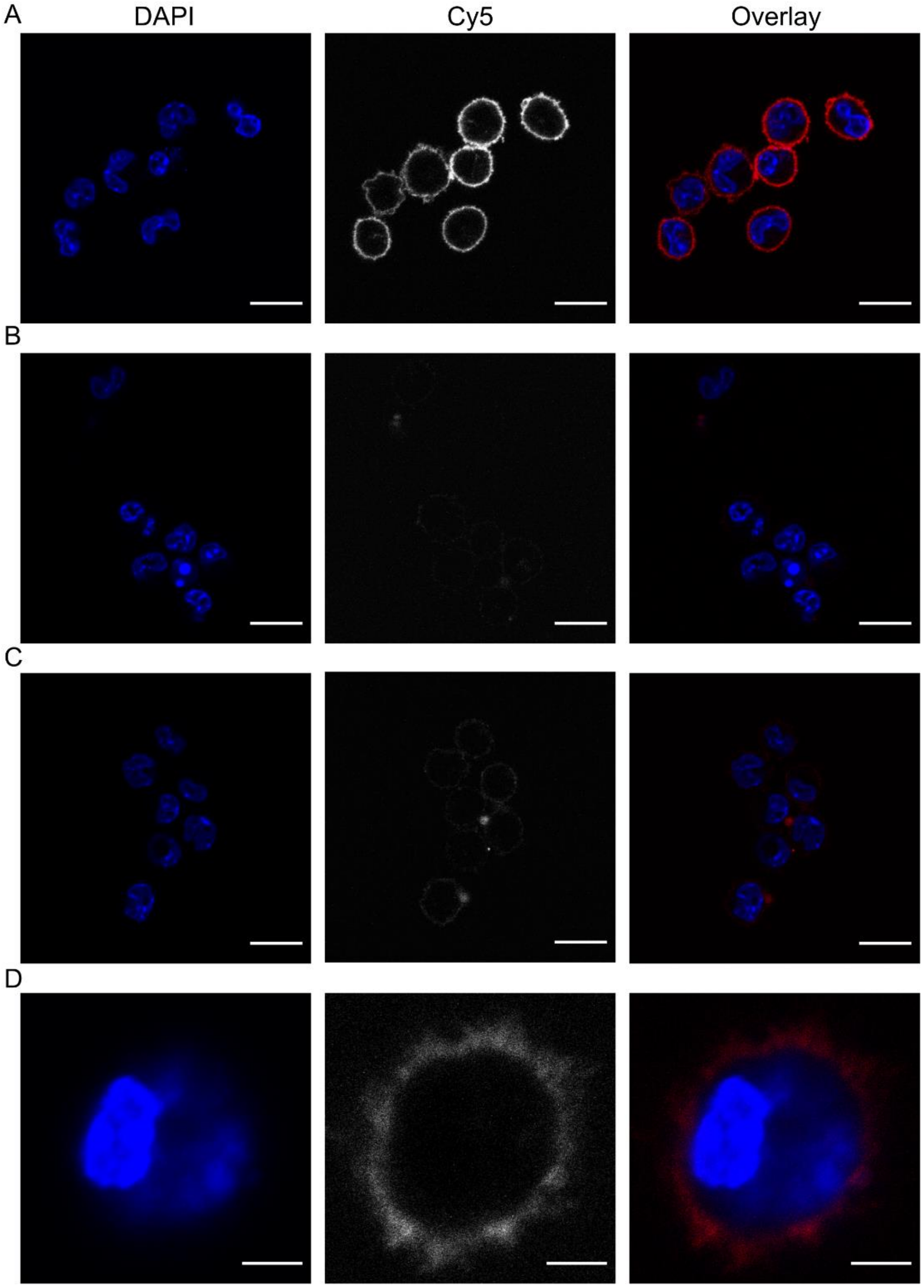

Figure 3.1: Representative confocal fluorescent images of LLP2A-Cy5 binding in 5TGM1 cells. (A) 1 µM LLP2A-Cy5, (B) 1 µM scLLP2A-Cy5, and (C) 1 µM LLP2A-Cy5 in presence of 100 µM unlabeled LLP2A, were incubated with 5TGM1-GFP cells at 4°C for 15 min. (D) 5TGM1 cells were incubated with 1 µM LLP2A-Cy5 at 37°C for 2.5 h. A-C, 60X magnification, scale bar, 15 µm; D, 100X magnification, scale bar, 3um. Blue channel, DAPI; Red channel, Cy5.

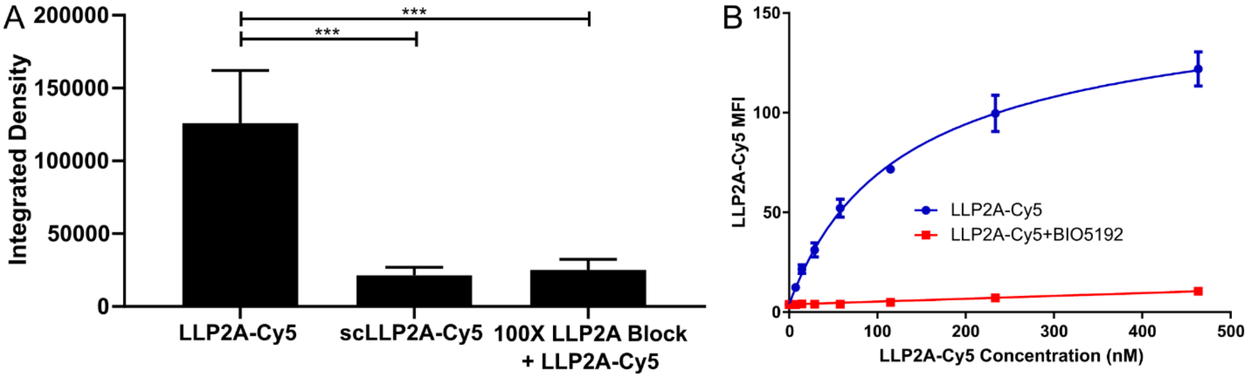

Figure 3.2: LLP2A-Cy5 uptake in 5TGM1 cells *in vitro*. (A) Total uptake in cells at 4^{o}C (15 min incubation). Integrated density is the product of the region of interest area and mean intensity value. (B) Saturation binding of LLP2A-Cy5 in 5TGM1 cells. Statistical significance was assessed using 1-way ANOVA with Tukey multiple comparisons test (***$p<0.001$).

Next, LLP2A-Cy5 was injected intravenously into end-stage untreated (week 4 post implantation) and bortezomib-treated (week 6 post implantation) mice to assess VLA-4 activity in response to bortezomib therapy. Imaging was performed 18-24 h after injection of the contrast agent. *In vivo* GFP expression was similar in both groups, although LLP2A-Cy5 signal was approximately 5-fold higher in the treated mice (**Figure 3.3A, B**). LLP2A-Cy5 signal in the treated animals was reduced in the pelvis and lower spine, and was primarily concentrated in the upper vertebrae and other tissue. In the untreated animals, the spatial distribution of LLP2A-Cy5 uptake correlated to GFP^{+} regions, indicating specific uptake within 5TGM1 tumors.

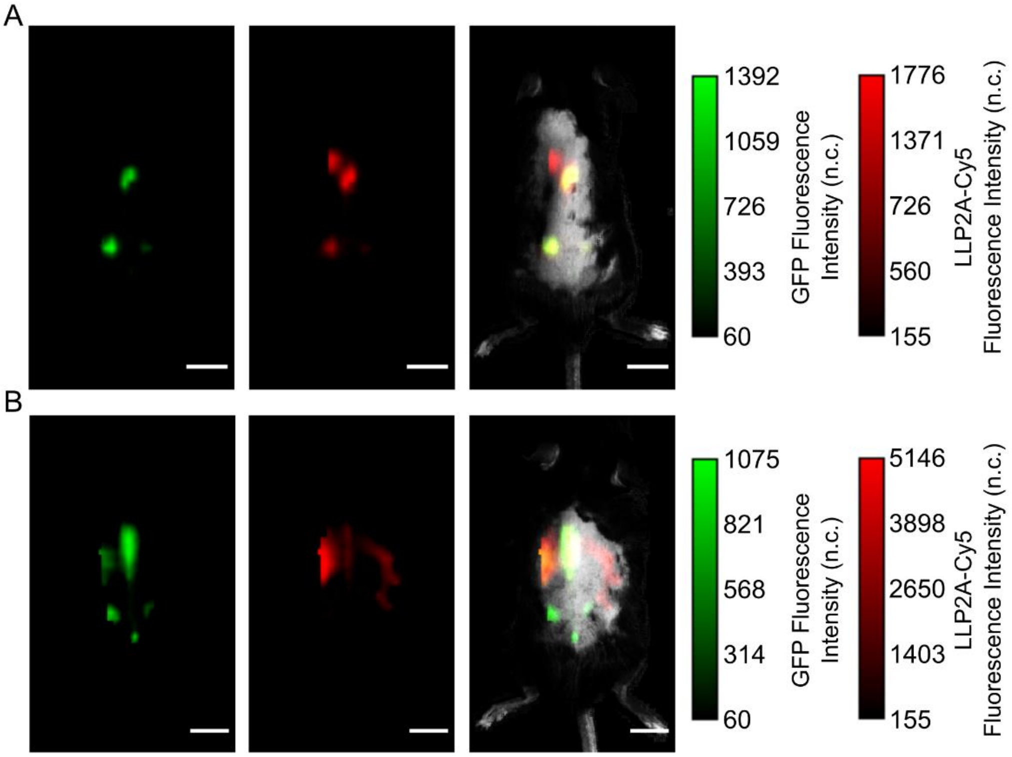

Figure 3.3: Representative 18-24 h fluorescence signal in C57Bl/KaLwRij mice bearing diffuse, intramedullary 5TGM1 tumors. (A) Untreated, week 4 post tumor implantation. (B) Bortezomib treated, week 6 post implantation. (Left) GFP, (Middle) Cy5, (Right) Overlay of GFP and Cy5 signal. Scale bar, 10mm.

Ex vivo fluorescent biodistribution confirmed that maximal LLP2A-Cy5 uptake was seen in the BM and spleen. There was statistically significant reduction in LLP2A-Cy5 fluorescence in the end-stage treated BM relative to the untreated tissue (6.34 ± 4.48-fold; **Figure 3.4A**). Indeed, tissue-to-muscle ratios for each of the extracted organs, including BM (1.11 ± 0.55) were within 1.26 ± 0.45, indicating minimal uptake of the contrast agent following bortezomib therapy. Additionally, GFP signal, which is an indicator for tissue-specific, viable tumor burden, decreased significantly in both spleen (3.42 ± 2.0-fold) and BM (9.78 ± 6.28-fold) (**Figure 3.4B**). These data contradict *in vivo* fluorescence imaging results, which seemed to suggest an increase in LLP2A-Cy5 signal following treatment.

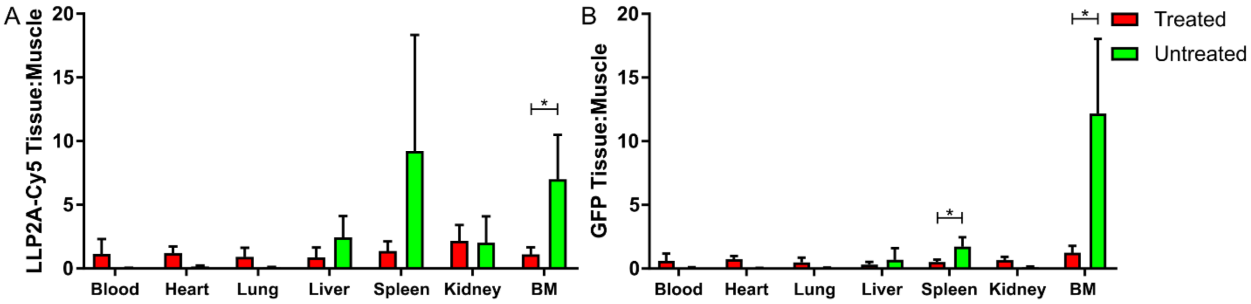

Figure 3.4: Ex vivo fluorescence biodistribution in end-stage treated and untreated mice. Background subtracted fluorescence intensity in each tissue was normalized by the mean muscle intensity, and presented as Tissue to Muscle ratios. (A) LLP2A-Cy5 biodistribution. (B) GFP biodistribution. Statistical significance was assessed using 2-way ANOVA with Sidak multiple comparisons test (**p*<0.05).

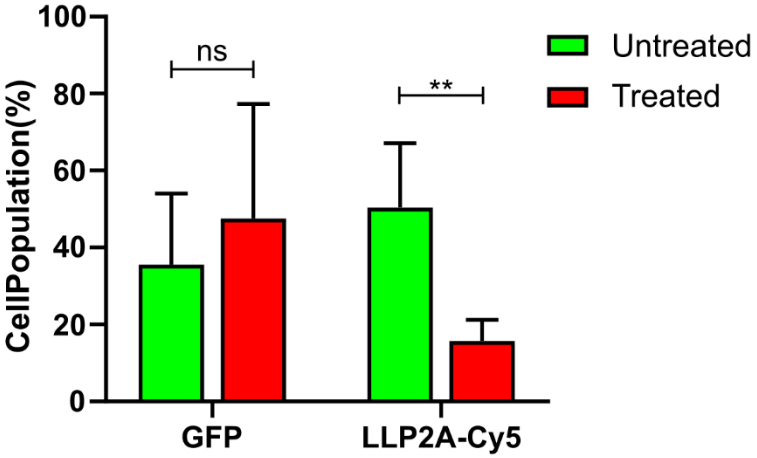

Figure 3.5: FACS of treated and untreated BM in the femur and tibia. The cell population is the percentage of GFP$^+$ and LLP2A-CY5$^+$GFP$^+$ cells within all cells in the BM. Statistical significance was assessed using the Student's two-tailed t-test within each gated group (***p*<0.01, ns, not significant).

Finally, tumor burden and LLP2A-Cy5$^+$ populations were quantified in both hematopoietic organs with FACS. There was no significant change in tumor burden in either BM or spleen following treatment (**Figure 3.5**). By contrast, the activated VLA-4$^+$ cell population within the BM was significantly reduced following bortezomib therapy (3.21 ± 1.55-fold). Consistent with the fluorescence intensity biodistribution, spleen tumor burden was low, and as a result, remained relatively similar in the treated group compared to the untreated animals (1.05 ± 0.96-fold reduction). These data indicate that BM uptake of LLP2A-Cy5 and activated VLA-4 expression changes following therapy response with bortezomib.

3.5 Discussion

LLP2A-Cy5 is a highly specific peptidomimetic ligand conjugated to a NIR fluorescent contrast agent (*7,9*). It is targeted to the activated conformation of the VLA-4 heterodimer, which is overexpressed on the surface of myeloma cells. Overexpression of VLA-4 is linked to increased drug resistance in MM, due to its participation in cell adhesion-mediated drug resistance pathways (*2*). In hematologic malignancies, studies have shown conflicting effects of VLA-4 expression on prognosis. In acute myeloid leukemia, for instance, overexpression of VLA-4 on tumor cells is correlated to better prognosis and low to intermediate disease stage (*14*). In MM, there is some evidence that VLA-4 expression is linked to reductions in overall survival and poor response to therapy (*15*). To further assess the role of VLA-4 in mediating therapy response in MM, we studied the uptake of LLP2A-Cy5 in a diffuse, intramedullary MM model using the immunocompetent C57Bl/KaLwRij strain.

We have previously demonstrated that LLP2A conjugated radiotracers have nanomolar binding affinities to activated VLA-4 expression on 5TGM1 cells (*16*). To ascertain the specificity of the optical LLP2A conjugate, saturation binding and confocal imaging of LLP2A-Cy5 incubation with 5TGM1 cells was performed. Non-specific binding was minimal, as demonstrated by co-incubation with the VLA-4 inhibitor BIO5192, excess unlabeled LLP2A blocking, and a scrambled, non-specific version of LLP2A-Cy5. Furthermore, the dissociation constant (K_d) for LLP2A-Cy5 was in the nanomolar range, and within two orders of magnitude of the nuclear conjugate. This difference in K_d is likely due to the sensitivity of the PET radiotracer, since the PET tracer is unaffected by noise driven by the confluence of optical absorption, scattering, and autofluorescence. Nevertheless, these results demonstrated the specificity of the optical LLP2A conjugate for activated VLA-4 expression on myeloma cells.

Confocal binding specificity experiments were first run at 4°C to minimize non-specific uptake and pinocytosis. Thus, fluorescence signal was concentrated at the cell surface with little to no internalization. Interestingly, however, when cells were incubated with LLP2A-Cy5 at physiologic temperature (37°C) for 2.5 h, cell internalization remained minimal. Fluorescence signal was predominantly localized at the cell surface. VLA-4 has a longer cell surface exposure relative to other integrins, which suggests that the fluorophore remains trapped at the cell surface due to constant integrin recycling (*17*). This behavior suggests an antagonist mechanism for LLP2A-Cy5, since ligand-based activation of integrins results in endocytosis and ligand uptake into the endosomes prior to integrin recycling (*18*).

Next, LLP2A-Cy5 uptake was used to study VLA-4 expression following bortezomib therapy. Bortezomib is known to inhibit VLA-4 expression and downstream adhesion-mediated resistance. As a result, we expected reduction in LLP2A-Cy5 uptake following treatment in our tumor model. Biodistribution and flow cytometry of the hematopoietic organs corroborated this expectation, although, interestingly, there was a similar, though not significant, decrease in LLP2A-Cy5 uptake in other tissue, especially muscle and the clearance organs. Bortezomib has been shown to have anti-inflammatory properties, with reductions in several inflammatory cytokines observed in arthritic models (*19*). Thus, bortezomib-induced reduction in general inflammation and MM-expressed VLA-4 may result in the overall depression in LLP2A-Cy5 uptake and subsequent rapid clearance from tissue within 24 hrs.

The decrease in LLP2A-Cy5 uptake in the tumor-bearing organs correlated to tumor burden reduction, as measured by flow cytometry. However, *in vivo* imaging of LLP2A-Cy5 and GFP expression contradicted *ex vivo* data, with an increase in LLP2A-Cy5 signal in the end-stage, treated cohort. This increase was statistically insignificant, but it suggests the need for additional longitudinal experiments. To assess the change in VLA-4 expression noninvasively in response to therapy, LLP2A-Cy5 imaging could be performed weekly, prior to treatment. This imaging strategy would also provide necessary normalization and adequate baseline comparison for the *in vivo* fluorescent signal.

3.6 Conclusion

In conclusion, our study has demonstrated the comparable viability of LLP2A-Cy5 *in vivo* and *in vitro* to previously studied nuclear LLP2A tracers. LLP2A-Cy5 showed selective VLA-4 binding in tumor tissue, with minimal nonspecific uptake *in vitro*. Additionally, we present the utility of LLP2A-Cy5 for tracking activated VLA-4 expression noninvasively in response to bortezomib therapy. Future work would include longitudinal observation of LLP2A-Cy5 uptake, testing in alternate myeloma cell lines with different VLA-4 expression profiles, and modeling bortezomib sensitivity in VLA-4 negative or knockout cell lines. These studies would improve understanding of VLA-4-driven stratification of proteasome inhibitor therapy response.

3.7 References

1. Noborio-Hatano K, Kikuchi J, Takatoku M, et al. Bortezomib overcomes cell-adhesion-mediated drug resistance through downregulation of VLA-4 expression in multiple myeloma. *Oncogene.* 2009;28:231-242.

2. Abe M, Hiura K, Ozaki S, Kido S, Matsumoto T. Vicious cycle between myeloma cell binding to bone marrow stromal cells via VLA-4-VCAM-1 adhesion and macrophage inflammatory protein-1alpha and MIP-1beta production. *J Bone Miner Metab.* 2009;27:16-23.

3. Uchiyama H, Barut BA, Mohrbacher AF, Chauhan D, Anderson KC. Adhesion of human myeloma-derived cell lines to bone marrow stromal cells stimulates interleukin-6 secretion. *Blood.* 1993;82:3712-3720.

4. von Metzler I, Krebbel H, Hecht M, et al. Bortezomib inhibits human osteoclastogenesis. *Leukemia.* 2007;21:2025.

5. Hideshima T, Richardson P, Chauhan D, et al. The proteasome inhibitor PS-341 inhibits growth, induces apoptosis, and overcomes drug resistance in human multiple myeloma cells. *Cancer Res.* 2001;61:3071-3076.

6. Roccaro AM, Hideshima T, Raje N, et al. Bortezomib Mediates Antiangiogenesis in Multiple Myeloma via Direct and Indirect Effects on Endothelial Cells. *Cancer Res.* 2006;66:184-191.

7. Peng L, Liu R, Marik J, Wang X, Takada Y, Lam KS. Combinatorial chemistry identifies high-affinity peptidomimetics against α4β1 integrin for in vivo tumor imaging. *Nat Chem Biol.* 2006;2:381-389.

8. Soodgupta D, Hurchla MA, Jiang M, et al. Very late antigen-4 (alpha(4)beta(1) Integrin) targeted PET imaging of multiple myeloma. *PLoS One.* 2013;8:e55841.

9. Soodgupta D, Zhou H, Beaino W, et al. Ex Vivo and In Vivo Evaluation of Overexpressed VLA-4 in Multiple Myeloma Using LLP2A Imaging Agents. *J Nucl Med.* 2016;57:640-645.

10. Weissleder R. A clearer vision for in vivo imaging. *Nat Biotechnol.* 2001;19:316-317.

11. Ramirez P, Rettig MP, Uy GL, et al. BIO5192, a small molecule inhibitor of VLA-4, mobilizes hematopoietic stem and progenitor cells. *Blood.* 2009;114:1340-1343.

12. Hurchla M, Garcia-Gomez A, Hornick M, et al. The epoxyketone-based proteasome inhibitors carfilzomib and orally bioavailable oprozomib have anti-resorptive and bone-anabolic activity in addition to anti-myeloma effects. *Leukemia.* 2013;27:430-440.

13. Hathi D, Zhou H, Bollerman-Nowlis A, Shokeen M, Akers WJ. Noninvasive imaging of multiple myeloma using near infrared fluorescent molecular probe. Paper presented at: Reporters, Markers, Dyes, Nanoparticles, and Molecular Probes for Biomedical Applications VIII, 2016.

14. Bae MH, Oh S-H, Park C-J, et al. VLA-4 and CXCR4 expression levels show contrasting prognostic impact (favorable and unfavorable, respectively) in acute myeloid leukemia. *Ann Hematol.* 2015;94:1631-1638.

15. Riaz W, Pham J, Zhang L, et al. Prognostic Significance of VLA4 and CD44 Expression by Flow Cytometry in Multiple Myeloma (MM). *Blood.* 2012;120:4975-4975.

16. Soodgupta D, Hurchla MA, Jiang M, et al. Very Late Antigen-4 (α4β1 Integrin) Targeted PET Imaging of Multiple Myeloma. *PLoS One.* 2013;8:e55841.

17. Bretscher MS. Circulating integrins: alpha 5 beta 1, alpha 6 beta 4 and Mac-1, but not alpha 3 beta 1, alpha 4 beta 1 or LFA-1. *EMBO J.* 1992;11:405-410.

18. Rainero E, Howe Jonathan D, Caswell Patrick T, et al. Ligand-Occupied Integrin Internalization Links Nutrient Signaling to Invasive Migration. *Cell Reports.* 2015;10:398-413.

19. Yannaki E, Papadopoulou A, Athanasiou E, et al. The proteasome inhibitor bortezomib drastically affects inflammation and bone disease in adjuvant-induced arthritis in rats. *Arthritis Rheum.* 2010;62:3277-3288.

Chapter 4: Longitudinal MRI of bortezomib-treated diffuse tumor burden in intramedullary myeloma

4.1 Overview

In this study, magnetic resonance imaging (MRI) was used to perform longitudinal, noninvasive imaging of the bone marrow (BM) space in a diffuse infiltration model of intramedullary MM. MRI is well established in clinical MM care, and is used extensively in diagnosis, staging, and identifying therapy response. However, there is a paucity of preclinical MRI applications for imaging MM disease progression and therapy response. Preclinical studies afford significant insight into BM remodeling as a function of pathogenesis and treatment. Here, we have validated longitudinal, multi-parametric MRI for imaging changes in the BM following treatment with bortezomib, which is known to induce significant remodeling of the bone and BM microenvironments. To approximate diffuse infiltrative lesions, the immunocompetent C57Bl/KaLwRij mouse strain was implanted intravenously with the syngeneic 5TGM1-GFP cells.

Our results showed that uptake of gadolinium contrast increased in the relapsed, treated cohort compared to the untreated, tumor-bearing animals. There were also significant regional differences in T1-weighted normalized signal intensities following bortezomib therapy, which correlated to spatially heterogeneous tumor viability. Parametric T2 relaxation identified overall tumor burden within the BM. Histology also indicated a reduction in total tumor burden and cell density following therapy, which was in line with MRI observations. This study highlighted potential preclinical MR markers for assessing viable tumor burden and BM permeability following therapy, and demonstrated the application of longitudinal, noninvasive imaging in an immunocompetent, intramedullary setting. The material covered in this chapter has been submitted to *NMR in Biomedicine*, under the title, “Longitudinal preclinical magnetic resonance imaging of diffuse tumor burden in intramedullary myeloma following bortezomib therapy.”

4.2 Introduction

Multiple myeloma (MM) is a cancer of terminally differentiated plasma B-cells in the bone marrow (BM) that accounts for approximately 15% of all mortalities associated with hematologic malignancies (*1,2*). Despite recent improvements in MM treatment, the efficacy of MM therapeutic strategies is still variable, especially at the late stages of cancer progression (*3*). Changes in therapy efficacy are influenced, in part, by the interactions of myeloma cells with the BM microenvironment. As a result, imaging strategies to noninvasively assess changes in the BM microenvironment can provide valuable information for treatment stratification.

In MM, clinical magnetic resonance imaging (MRI) is used extensively to delineate lesions and stage disease progression following treatment (*4*). Traditional biological markers, including bone remodeling and angiogenesis-related factors and plasma cell infiltration, are correlated to the presence of diffuse, variegated, and focal lesions in T1-weighted, non-contrast enhanced and fat-suppressed, T2-weighted MRI (*5,6*). In particular, T1-weighted MRI revealed a high correlation between diffuse infiltration and poor prognosis (*5*). Diffusion weighted imaging of MM patients has also identified significant differences in median apparent diffusion coefficients between responders and non-responders to systemic treatment (*7*). Kinetic modeling of vascular transport with T1-weighted, dynamic contrast-enhanced (CE) imaging identified increases in BM angiogenesis and vascular bed density, which may correspond to the transition to malignant states of MM (*8*). Finally, magnetic resonance spectroscopy of spinal and pelvic BM showed a statistically significant increase in lipid fractions in patients responding to therapy, indicating a reduction in the ratio of hematopoietic marrow to adipose tissue (*9*). These clinical studies demonstrate that MRI is as an attractive option for noninvasively studying relative changes in the BM microenvironment during disease progression and for monitoring therapy response.

While the role of MRI is well established in the clinic, studies demonstrating the potential of preclinical MRI in MM are scarce. Due to its excellent soft-tissue contrast and resolution, MRI provides a preclinical platform for studying the BM microenvironment in a noninvasive, longitudinal manner. Here, we demonstrate the use of multi-parametric MRI for longitudinal imaging of the viable tumor burden in the BM in a syngeneic immunocompetent model of intramedullary diffuse MM. Treatment with a proteasome inhibitor, bortezomib, was performed, due to its relevance in MM clinical care at all stages and its effect on BM remodeling (*10*). Effective changes in MR markers were correlated with histology for validation.

4.3 Materials and Methods

4.3.1 Cell culture and reagents

5TGM1-GFP cells (5TGM1; kind gift from Dr. K. N. Weilbaecher, Washington University, Department of Medicine) were maintained at 10^6 cells/mL in Iscove’s Modified Dulbecco Medium supplemented with 10% v/v fetal bovine serum and 1% penicillin/streptomycin (all from Thermo Fisher Scientific, MA, USA). Bortezomib (Sigma Aldrich, MO, USA) doses were prepared prior to each therapy injection.

4.3.2 Tumor model and bortezomib therapy

All animal studies were conducted according to protocols approved by the Washington University Institutional Animal Care and Use Committee. Mice were anesthetized under 2% v/v isoflurane/100% O_2 prior to tumor implantation. Female 4-8 week old C57Bl/KaLwRij mice were injected intravenously with 10^6 5TGM1 cells, *via* the lateral tail vein.

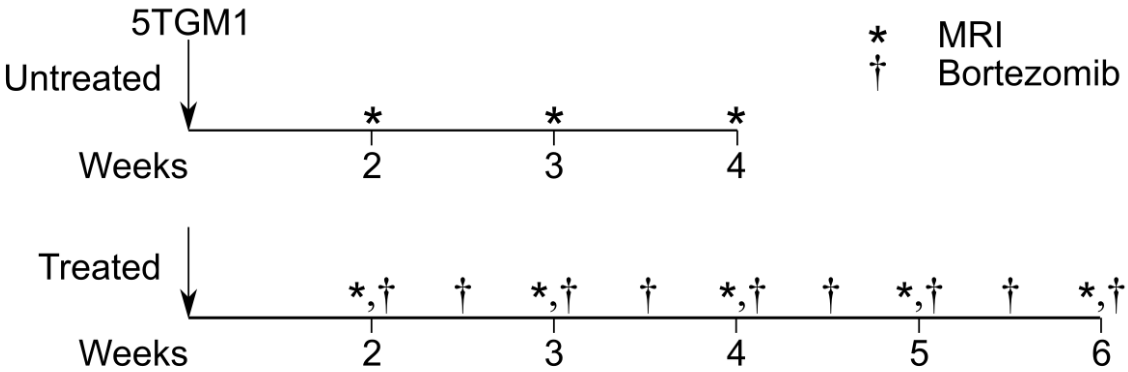

Figure 4.1: Study design, imaging, and therapy timeline. Untreated tumor-bearing (N = 5) 5TGM1/KaLwRij were imaged weekly with non-CE T2 parametric mapping and 3D CE T1-weighted MR weekly beginning two weeks post 5TGM1 tumor implantation. The bortezomib treatment cohort (N = 9) was similarly implanted with 5TGM1 tumors and injected with bortezomib via intraperitoneal injection at 1 mg/kg twice a week, beginning two weeks post tumor implantation. On imaging days (e.g., day 14, 21, 28), therapy and vehicle injections were performed immediately following imaging. As with the untreated tumor-bearing cohort, each mouse was imaged weekly with non-CE T2 parametric mapping and a 3D CE T1-weighted pulse sequence.

Tumor-bearing mice were separated into randomly assigned untreated (n=5) and bortezomib-treated (n=9) independent cohorts (**Figure 4.1**). Bortezomib therapy was administered intraperitoneally at 1 mg/kg twice a week beginning on day 14 post tumor implantation(*11*). Untreated animals received the vehicle control on the same schedule. Non-tumor bearing animals (n=4) were imaged once.

4.3.3 Preclinical MRI

Preclinical ^{1}H MRI experiments were performed on a 4.7-T Agilent/Varian (Santa Clara, CA, USA) DirectDrive MRI scanner employing a horizontal Oxford Instruments (Abington, Oxfordshire, UK) magnet with 40-cm clear bore diameter and an actively shielded Resonance Research Inc. (Billerica, MA) gradient/shim coil assembly of 11.5-cm bore diameter driven by Oy International Electric Company (IEC; Helsinki, Finland) model A-240 amplifiers (~70 gauss/cm is achievable with a rise time of ~120 µs). All imaging experiments were conducted under 1% v/v isoflurane/100% O_2 anesthesia. Mice were placed prone, with the hind leg immobilized within a tuned circular radiofrequency surface coil. The hind leg was used to image changes in large BM sites with minimal motion artifacts. Body temperature was maintained with an external air heater. Planning and localization of femur and tibia regions of interest (ROIs) were performed using sagittal (field of view (FOV) 2.5x2.5x0.5 cm^3) and transverse (FOV 1.5x1.5x1 cm^3) T1-weighted gradient echo sequences (flip angle 20^o, repetition time (TR) 100ms, echo time (TE) 5 ms). Following field shimming, T2 parametric maps were collected using multi-slice, multiple spin echo (FOV 2x2x0.3 cm^3, TR 2s, 7.1 ms ≤ TE ≤ 113.5 ms, 16 echoes, 0.156x0.156x1 mm^3 voxel dimensions, 128x128x3 matrix dimensions, 1 average). Mice were then injected intraperitoneally with 12 µmol MultiHance (Bracco Diagnostics, NJ, USA). To allow the contrast agent to accumulate and approach steady state, CE T1-weighted gradient echo 3D images were collected 8-10 minutes following injection of the agent (FOV 2x1x1 cm^3, flip angle 20^o, TR 25 ms, TE 4.2 ms, 0.78x0.78x0.78 mm^3 voxel dimensions, 128x256x128 matrix dimensions, 4 averages).

4.3.4 Bone histology and imaging

Following euthanasia, femur and tibia were removed and decalcified. Bone tissue was embedded in paraffin, sectioned at 5 µm thickness, and stained with hematoxylin and eosin (H&E). Brightfield images of the H&E stained slides were acquired using the NanoZoomer Digital Pathology System (NanoZoomer 2.0-HT, Hamamatsu, Japan).

4.3.5 Data analysis

Image analysis was performed using in-house routines developed on MATLAB R2014b (Mathworks, MA, USA). ROIs for the femur, tibia, and muscle volumes were drawn on each slice of T1-weighted, non-CE and CE images using ImageJ (National Institutes of Health, MD, USA). To minimize variability in inter-scan T1-weighted image intensity resulting from unavoidable modest variability in coil placement and subject positioning, CE T1-weighted images were normalized by the mean voxel intensity of the muscle volume of interest (VOI). T2 parametric maps were generated using non-linear least squares fitting of the equation $S(t) = A + B \times \exp(-t/C)$ for each voxel, where $S(t)$ is the signal intensity, t is TE, A and B are scaling constants, and C is the voxel-specific T2. The constant, A, accounts for both the positive, non-zero mean of Rician noise and any steady-state, non-zero transverse magnetization resulting from imperfect, slice-selective 180^o refocusing pulses.

The T1-weighted CE 3D images were also analyzed using texture statistics to assess the spatial distribution of the signal within the femur and tibia VOIs. Image histograms were distributed into equally sized integer bins and voxels were relabeled to the integer values of their respective bins. A gray-level co-occurrence matrix (GLCM) was computed on the VOI covering each neighboring voxel in 3D space. Texture statistics were calculated from the 3D GLCM (*12,13*).

Bone histology images were imported into MATLAB using ImageJ and the Bio-Formats application interface (*14*). Images were first manually segmented into femur and tibia BM ROIs, and then into tumor and non-tumor ROIs. Tumor burden (%) was calculated for tumor-bearing groups as (Total ROI area – Non-tumor area)/(Total ROI area) * 100%.

4.3.6 Statistical analysis

Statistical analysis on histogram and texture statistics from the imaging and histology was performed using GraphPad Prism 7.0 (GraphPad, CA, USA). One-way analysis of variance (ANOVA) with Tukey multiple comparisons test was used to assess statistical significance between multiple treatment groups for femur and tibia VOI individually. A *p*-value less than 0.05 was defined as statistically significant.

4.4 Results

4.4.1 Observed differences in normalized 3D CE T1-weighted MRI

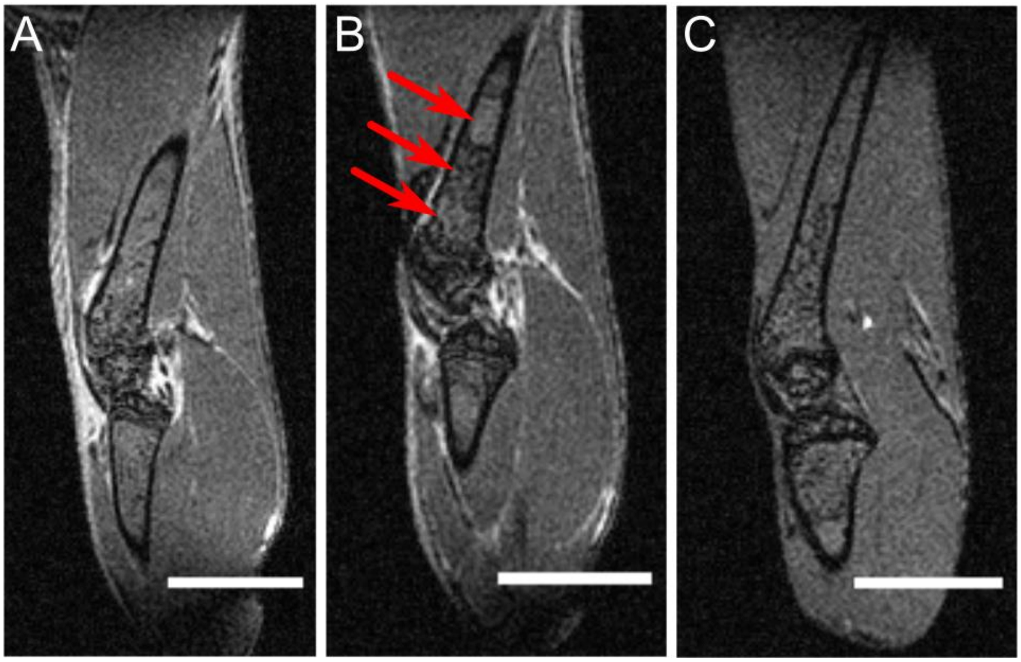

Figure 4.2: Representative sagittal sections of T1-weighted CE-MRI. Each voxel in the volume was normalized by the mean of representative muscle VOI located in the lower leg. (A) Non-tumor bearing. (B) Untreated tumor-bearing, week 4. (C) Treated tumor-bearing, week 6. Red arrows highlight regions of significant spatial intensity variation. Scale bar, 4 mm.

Diffuse tumor burden in the femur and tibia VOIs in treated and untreated C57Bl/KaLwRij mice bearing intramedullary 5TGM1 tumors was visualized using normalized CE T1-weighted imaging. Due to heterogeneity in the BM composition of the femur and tibia, end-stage untreated mice displayed spatial variation in T1-weighted CE image intensity in the femur, and to a lesser extent, tibia (**Figure 4.2B**). By contrast, non-tumor bearing (**Figure 4.2A**) and end-stage treated (**Figure 4.2C**) groups showed minimal spatial heterogeneity in either femur or tibia. These observations were supported by the equivalent gray-level normalized images, which corroborated the overall homogeneity of the signal in the non-tumor and treated mice (**Figure 4.3A, C**) relative to the untreated animals (**Figure 4.3B**). Mid-stage, untreated (week 3) and treated (week 4) mice had similar spatial distributions in both femur and tibia (**Figure 4.4A-D**).

Textural analysis of these images using 3D GLCM and Haralick features confirmed the observed spatial distributions. The GLCM autocorrelation, which measures the fineness of the textured image, was significantly reduced in the femurs of untreated tumor-bearing mice ($p<0.05$) relative to the non-tumor bearing and treated tumor-bearing groups (**Figure 4.5A**). Furthermore, there was a statistically significant increase in the difference in autocorrelation between the treatment time points and the pre-treatment baseline relative to the untreated groups ($p<0.01$) ((**Figure 4.5B**). These results demonstrate that region-specific permeability and contrast agent uptake via vascular availability are affected by bortezomib treatment response.

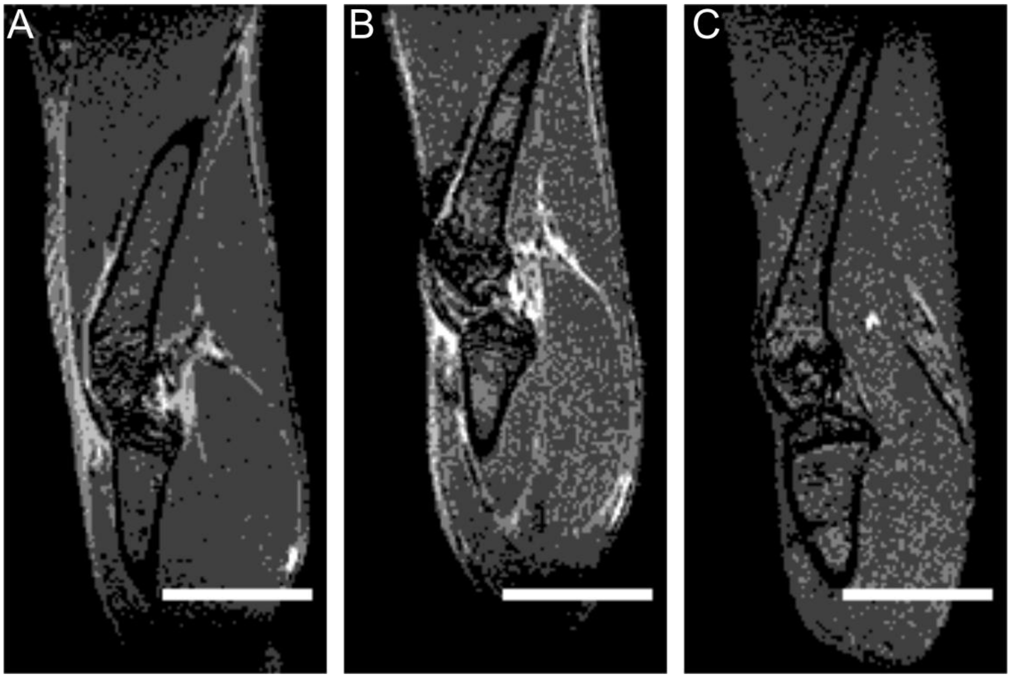

Figure 4.3: Gray-level, normalized, CE T1-weighted representative sagittal sections. Images were normalized by distributing the grayscale intensity value of each voxel into 8 equal-width bins. (A) Non-tumor bearing. (B) Untreated tumor-bearing, week 4. (C) Treated tumor-bearing, week 6. Scale bar, 4 mm.

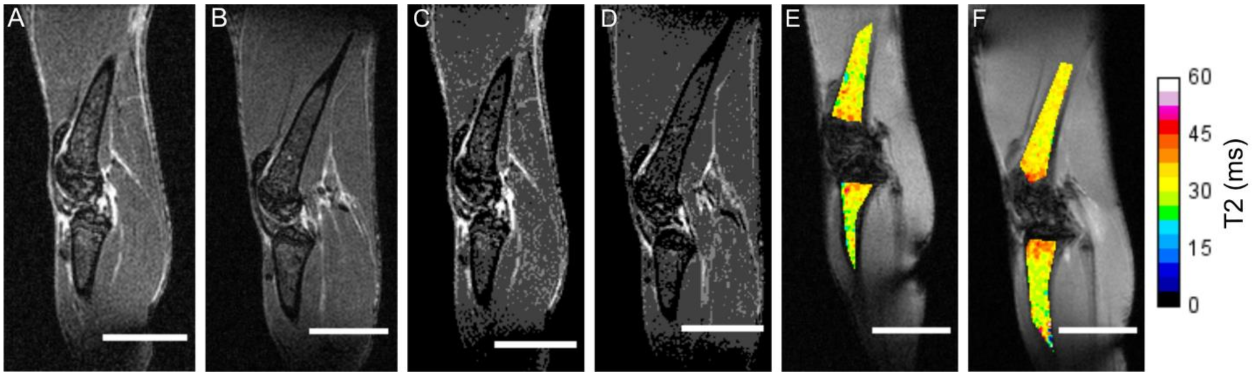

Figure 4.4: Representative sagittal sections of T1-weighted CE and T2 parametric images of mid-series time points in untreated and treated tumor-bearing mice. (A-B) T1-weighted CE 3D MRI, normalized by the mean voxel intensity of the representative muscle ROI in untreated (week 3) and treated (week 4) tumor-bearing. (C-D) T1-weighted CE 3D MRI, normalized by gray level equalization. (E-F) T2 parametric maps of femur and tibia ROIs overlaid on T1-weighted non-CE oblique slices. Scale bar, 4 mm; T2 range, 0-60 ms.

Statistical analysis of mean T1-weighted CE normalized intensities supported the spatial heterogeneity observations in representative sections (**Figure 4.6A**). End-stage (weeks 5-6), treated tumor-bearing mice showed a statistically significant increase in T1-weighted intensity relative to the mid-stage (weeks 3-4) treated and untreated groups in the tibia ($p<0.01$). Interestingly, in the femur, the mean T1-weighted intensity in the non-tumor bearing group was significantly higher ($p<0.001$) than in the rest of the groups and had a tighter intra-group distribution relative to the non-tumor tibia VOI. To minimize the underlying intra-animal heterogeneity, the %difference between the pre-treatment and the latter stage time-points was calculated. The end-stage treated group showed a statistically significant increase in the %difference in T1-weighted intensity relative to the mid-stage treated and untreated groups in the tibia ($p<0.05$), but not the femur (**Figure 4.6B**).

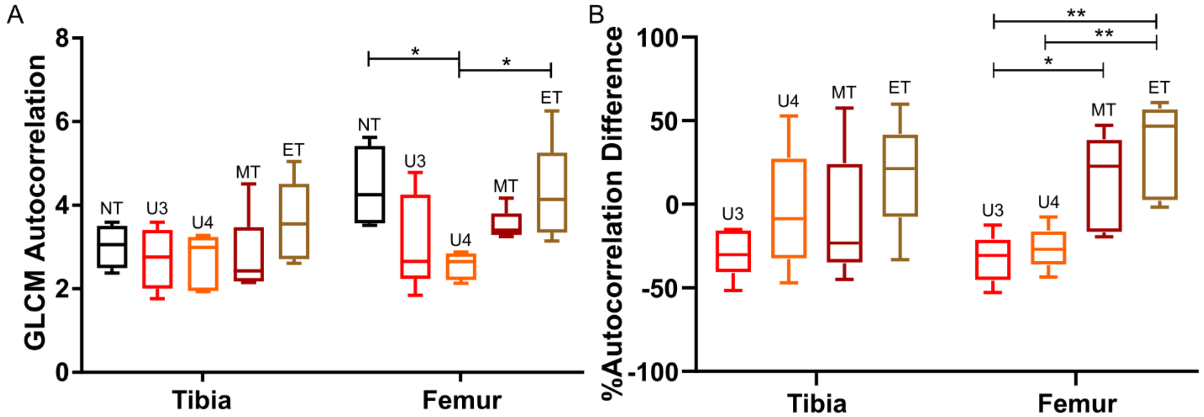

Figure 4.5: Mean autocorrelation of 3D gray-level co-occurrence matrix (GLCM) in tibia and femur VOIs in T1-weighted CE images. (A) Mean GLCM autocorrelation for non-tumor bearing (NT), untreated tumor-bearing at weeks 3 (U3) and 4 (U4), and treated tumor-bearing at weeks 3-4 (MT) and weeks 5-6 (ET) groups. (B) Mean GLCM autocorrelation relative to week 2 baseline for each animal (%difference = (Time-point Mean – Baseline Mean)/(Baseline Mean)). Statistical significance was assessed using a one-way ANOVA with Tukey multiple comparisons test performed individually on the tibia and femur VOIs (*$p < 0.05$). Whiskers indicate 5-95% confidence intervals.

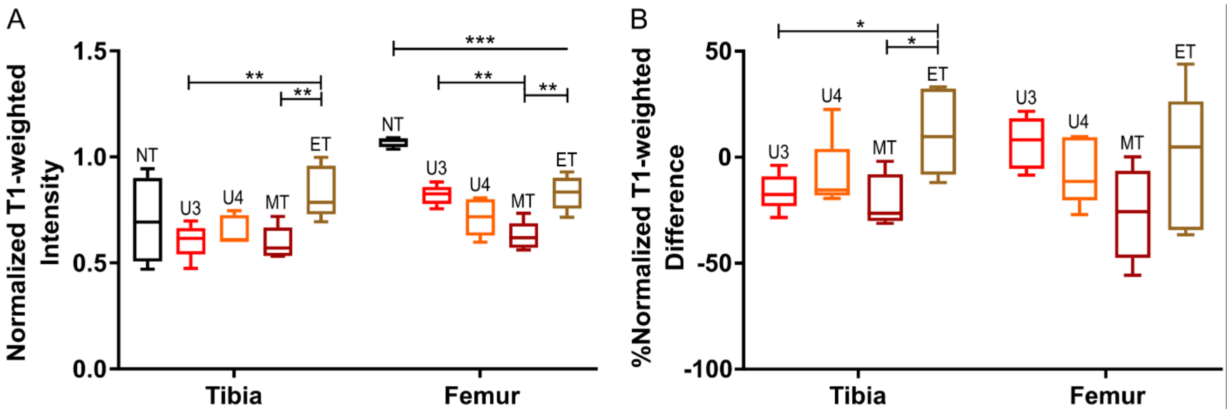

Figure 4.6: Mean CE T1-weighted intensity, normalized by mean muscle intensity, in femur and tibia VOIs. (A) Mean CE T1-weighted normalized intensity in non-tumor bearing (NT) mice, untreated tumor bearing mice at weeks 3 (U3) and 4 (U4), and treated tumor-bearing mice at weeks 3-4 (MT) and 5-6 (ET). (B) Mean CE, T1-weighted normalized intensity relative to week 2 baseline for each animal (%difference = (Time-point Mean – Baseline Mean)/(Baseline Mean)).

Statistical significance was calculated using a one-way ANOVA with the Tukey multiple comparisons test performed individually on the tibia and femur VOIs (*p < 0.05, **p < 0.01, ***p < 0.001; closed line indicates comparison between two groups, open-ended line indicates statistical significance between one group against all other included groups). Whiskers indicate 5-95% confidence intervals.

4.4.2 Effect of disease stage and bortezomib therapy on T2 parametric maps

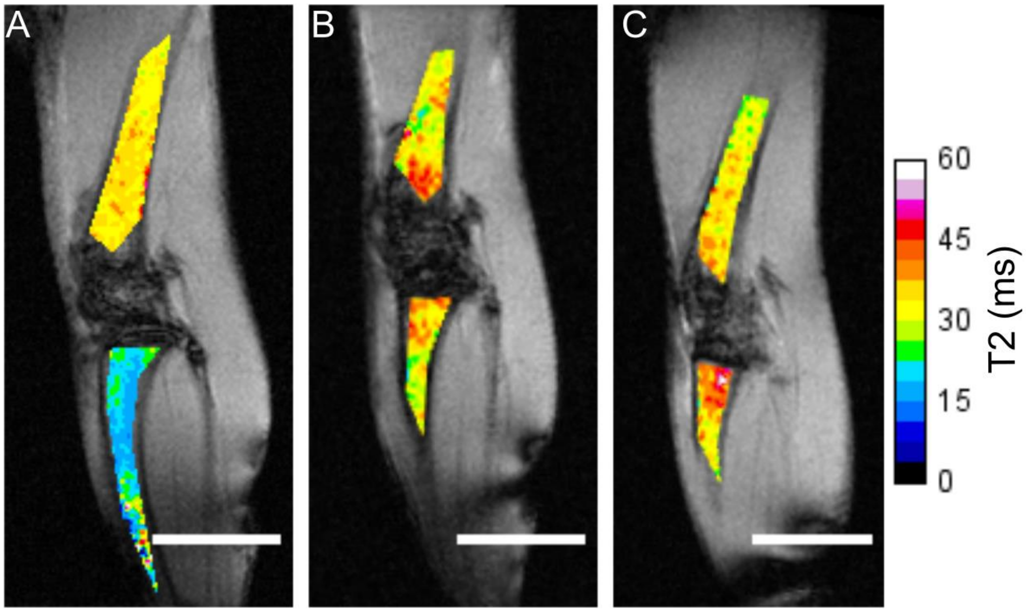

Figure 4.7: Representative T2 parametric maps of femur and tibia BM. (A) Non-tumor bearing mice. (B) Untreated tumor-bearing mice, week 4. (C) Treated tumor-bearing mice, week 6. Femur and tibia T2 maps were overlaid on non-CE, oblique, T1-weighted intensity images normalized by the mean voxel intensity of the muscle ROI. Scale bar, 4 mm; T2 range 0-60 ms.

To identify the effect of treatment on viable tumor burden, T2 parametric maps were generated. These maps identified substantive changes in the tibia VOI after tumor implantation. The non-tumor-bearing tibia had low overall T2 (**Figure 4.7A**), relative to all other groups. By contrast, representative end-stage untreated (week 4) and treated (week 6) groups displayed similar overall distribution of T2 values in both VOIs. There was an increase in spatial heterogeneity in the treated tibia VOI relative to the femur VOI and both VOIs in the representative untreated image (**Figure 4.7B, C**). Interestingly, high T2 values (>45 ms) in both groups were clustered near the epiphyseal plate of the femur and tibia. This result was seen in the mid-stage untreated (week 3) and treated (week 4) representative images as well, albeit to a lesser degree (**Figure 4.4E, F**). The representative T2 parametric maps correlated with changes in the viable tumor burden and changes in the homogeneity of the BM tissue observed in the representative T1-weighted CE images.

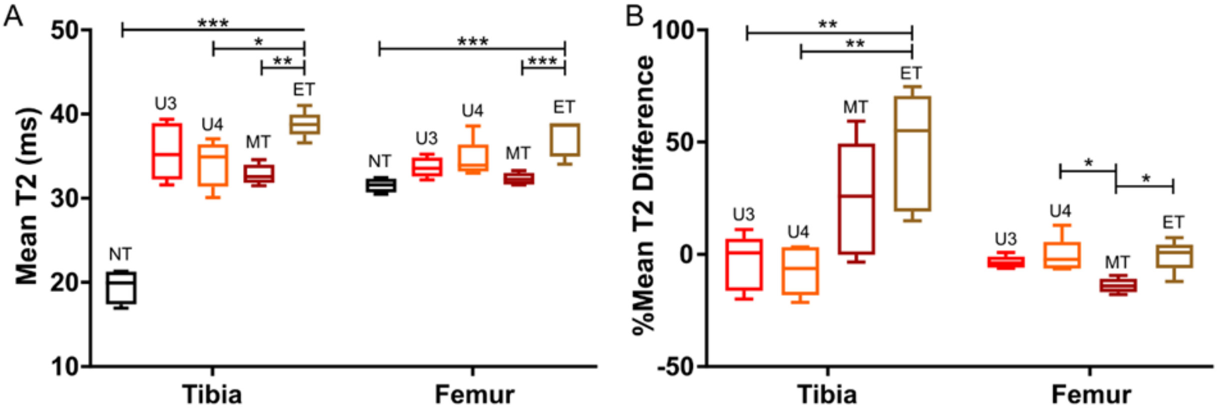

Figure 4.8: Mean T2 in femur and tibia VOIs. (A) Mean T2 in non-tumor bearing (NT) mice, untreated tumor-bearing mice at weeks 3 (U3) and 4 (U4), and treated tumor-bearing mice at weeks 3-4 (MT) and weeks 5-6 (ET). (B) Mean T2 relative to week 2 baseline for each animal (%difference = (Time-point Mean – Baseline Mean)/(Baseline Mean)). Statistical significance was assessed using a one-way ANOVA with Tukey multiple comparisons test performed individually on the tibia and femur VOIs (*p < 0.05, **p < 0.01, ***p < 0.001; closed line indicates comparison between two groups, open-ended line indicates statistical significance between one group against all other included groups). Whiskers indicate 5-95% confidence intervals.

Quantitative analysis of the T2 parametric images showed similar overall trends to the qualitative observations from the representative parametric images (**Figure 4.8A**). In both femur and tibia, mean T2 times in the end-stage (weeks 5-6), treated tumor-bearing group was significantly increased relative to the T2 times in the mid-stage treated group (*p*<0.01). The T2 relaxation time in the end-stage, treated group showed a statistically significant increase relative to the end-stage untreated group in the tibia (*p*<0.05), but not femur. In both VOIs, the non-tumor bearing group had low mean T2, although as observed, the non-tumor T2 in the tibia was significantly lower than in the other groups (*p*<0.001). Following normalization with pre-treatment imaging, the treated end-stage and mid-stage groups were more heterogeneous in the tibia VOI than in the femur (**Figure 4.8B**). In the tibia, there was a statistically significant difference in the %T2 difference between the untreated groups and the end-stage treated group (*p*<0.01). By contrast, in the femur, there was a significant reduction in the %T2 difference mid-stage treated relative to the end-stage untreated and treated groups (*p*<0.05). These results suggest that the T2 parametric maps are responsive to the overall disease stage following treatment.

The spatial and temporal distributions of contrast uptake and T2 relaxation times in the BM were most affected by response to bortezomib therapy. Spatial intensity heterogeneity was maximized in the untreated tumor-bearing group and reduced following treatment with bortezomib. Similarly, mean T2 relaxation times were significantly increased following tumor implantation and showed significant difference from the untreated groups relative to pre-treatment imaging. In summary, T1-weighted CE imaging and T2 parametric maps were indicative of viable tumor burden, with significant longitudinal changes seen at the end-stage of the treated tumor-bearing group.

4.4.3 Validation of imaging results with H&E of femur and tibia BM

To validate MRI results, the femur and tibia were extracted at end-stage disease and stained with H&E. The %tumor burden was quantified as the total tumor tissue relative to non-tumor tissue in the femur and tibia ROIs. Non-tumor bearing mice had high lipid content clustered near the femur epiphyseal plate and low overall cell density (**Figure 4.9A**). In the end-stage, untreated tumor-bearing group, the healthy BM was overtaken by densely packed, mononuclear tumor cells (**Figure 4.9B**, **Figure 4.10B**). Non-tumor BM tissue was sequestered in the epiphysis of the femur and tibia. By contrast, the end-stage, treated tumor-bearing group showed a statistically significant reduction in tumor burden in the femur (*p*<0.001) and tibia (*p*<0.001) relative to the untreated mice (**Figure 4.9C**, **Figure 4.10B**). Tumor tissue was primarily concentrated proximal to the epiphyseal plate in both femur and tibia, with minimal tumor burden at distal sites in either bone (**Figure 4.9C**). Tumor burden was also highest near the epiphyseal plate in the mid-treatment cohort, although the overall distribution of tumor burden within the cohort was highly heterogeneous in both femur and tibia (**Figure 4.10A, B**). These results suggest that bortezomib therapy restricts tumor cell growth to the rapidly growing epiphyseal plate region, which may correlate with the observed high T2 values near the epiphyseal plate in the end-stage treated group (**Figure 4.8C**).

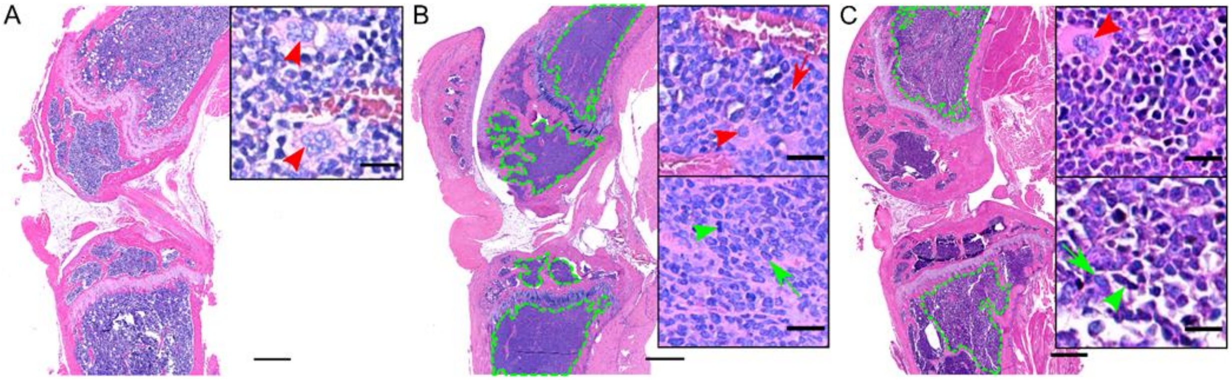

Figure 4.9: Representative H&E sections. (A) Non-tumor bearing mice. (B) Untreated tumor-bearing mice, week 4. (C) Treated tumor-bearing mice, week 6. Green outline indicates tumor boundaries. Top inset highlights non-tumor cells, as indicated by the presence of megakaryocytes (red arrowhead) and segmented nuclei (red arrow). The bottom inset highlights tumor cells, as indicated by the presence of mitoses (green arrowhead) and oval plasma cell nuclei (green arrow). Scale bar, 500 µm; inset scale bar, 20 µm.

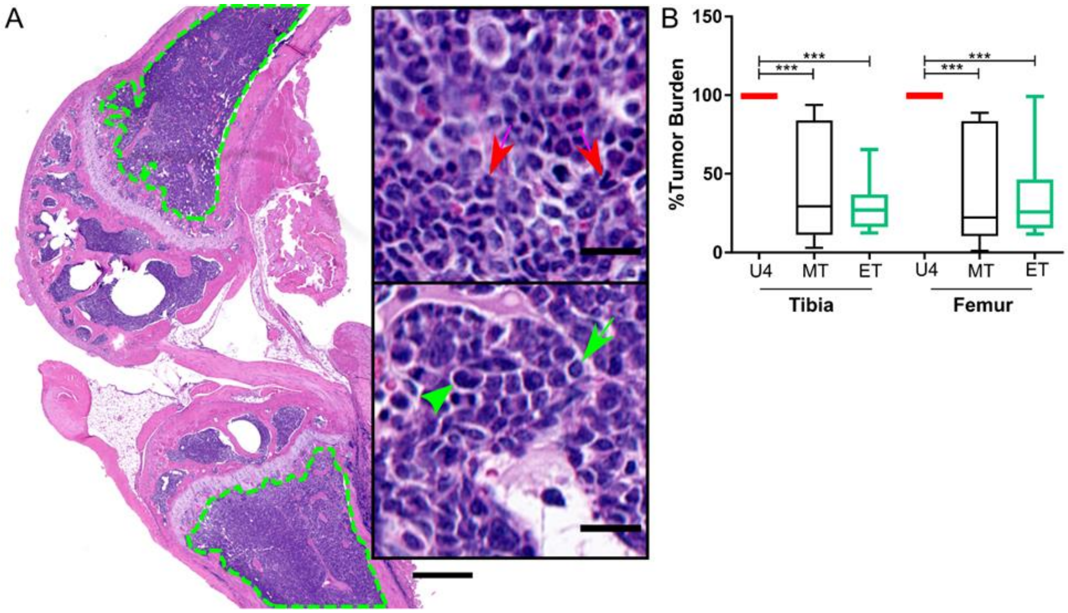

Figure 4.10: Representative H&E sections and quantification of total tumor burden. (A) Mid-treatment, week 4. Green outline indicates tumor boundaries. Top inset highlights non-tumor cells, as indicated by the presence of segmented nuclei (red arrows). Bottom inset highlights tumor cells, as indicated by the presence of mitoses (green arrowheads) and oval plasma cell nuclei (green arrows). (B) %Tumor burden in untreated week 4 (U4) and treated weeks 3-4 (MT) and weeks 5-6 (ET) (%tumor burden = (Total Tissue Area – Non-tumor Area)/(Total Tissue Area)*100%). Statistical significance was assessed using one-way ANOVA with Tukey multiple comparisons test on the tibia and femur individually (***p<0.001). Whiskers denote 5-95% confidence intervals. Scale bar, 500 µm; Inset scale bar, 20 µm.

In summary, histology and *ex vivo* tumor burden quantification demonstrated the difference in the distribution of tumor between the end-stage untreated and treated tumor-bearing groups. BM in the femur and tibia of untreated animals was dominated completely by tumor tissue, while tumor burden was concentrated proximal to the epiphyseal plate in the treated animals. Tumor cell density was also reduced in both tibia and femur, especially at the end-stage, following relapse from bortezomib therapy. Spatial distributions of the tumor and normal BM in the tibia and femur were similar to the observed trends in the imaging acquired using T1-weighted CE and T2 parametric pulse sequences.

4.5 Discussion

This study marks one of the first instances utilizing multi-parametric MRI to longitudinally follow changes in the BM in response to MM stage and therapy in a preclinical immunocompetent model. Previously, Fryer *et al* demonstrated that a combination of *in vivo* bioluminescence and T2-weighted tumor volume were correlated to therapy response in an intratibial immunocompromised model of MM (*15*). Similarly, Gauvain *et al* used a metastatic melanoma model in immunocompetent C57Bl/6 mice to identify early stage bone metastases using a combination of T2-weighted and T2 parametric imaging (*16*). In both studies, the tumor model resulted in focal lesions, which have well-defined boundaries. However, in this study, a diffuse intramedullary tumor model was generated by intravenous injection of syngeneic tumor cells within an immunocompetent strain. The advantages of this model include the preservation of the immune response to the myeloma cells and the presence of therapy-induced inflammation. Since MRI offers high soft-tissue contrast and spatial resolution, we hypothesized that MRI could provide a noninvasive, longitudinal approach for studying changes in the BM induced by bortezomib therapy and MM disease progression. The key MR features and their corresponding biological correlates in the BM are summarized in **Table 4.1**.

Table 4.1: Summary of MR markers and their corresponding biological features for each imaging group relative to the untreated week 4 group. 0, no effect; +, difference in features; ++, significant difference in features.

			Untreated		Treated	
MR marker	Biological Correlate	Non-tumor	Week 3	Week 4	Mid-stage (Wks 3-4)	Relapse (Wks 5-6)
Autocorrelation (femur)	Tissue Homogeneity	++	0	0	+	++
Mean normalized T1-weighted intensity	Viable tumor burden	N/A	0	0	++	++
Mean T2 relaxation times	Diffuse tumor burden	N/A	0	0	+	++
H&E cell density	Total tumor burden	N/A	N/A	0	++	++

T1-weighted, CE, 3D MRI signal intensities were indicative of contrast uptake within regions of tissue. Gadolinium-based contrast agents induce shortening of T1 relaxation times, resulting in increases in T1-weighted signal intensity in highly vascular and permeable regions relative to necrotic and less vascularized regions (*17*). The uptake of contrast within the BM in the femur and tibia was spatially heterogeneous, especially in the end-stage, untreated, tumor-bearing animals. In general, significant spatial heterogeneity and the presence of well-defined regions of differential contrast uptake within the BM were restricted to the femur in the untreated mice. This could be due to the presence of higher overall hematopoiesis in the femur, with concentrated marrow adipocyte tissue near the epiphyseal plate in the femur. The role of adipose tissue in myeloma progression is considered controversial, with some literature presenting a supporting role for adipose tissue and other studies showing that adipose tissue may restrict myeloma growth (*18*). Nevertheless, the presence of adipose tissue in the BM may result in increased myeloma cell viability, thus generating the region-specific uptake patterns seen in the T1-weighted CE MRI. The underlying hematopoietic niches may also drive the concentrations of vascularized and accessible tumor burden within the femur BM, especially in sites distal to the femur epiphyseal plate.

Treatment with bortezomib also induced increases in contrast agent uptake within the BM in both femur and tibia. Bortezomib causes significant marrow remodeling, resulting in reduction in osteoclast activity and cytokine secretion, and inhibition of tumor-induced angiogenesis (*19,20*). At the same time, healing and tumor cell death induced by bortezomib may also generate increases in angiogenesis and inflammation, which may result in increased uptake of contrast within high tumor burden regions after relapse. By contrast, in the mid-stage treated group, bortezomib efficacy and inhibition of neo-vascularization likely dominates, resulting in low normalized T1-weighted intensity.

In contrast to T1-weighted CE imaging, which was directly correlated to tumor vascularization and permeability, T2 parametric maps are representative of tumor burden and overall water content. There was less spatial heterogeneity in the T2 parametric maps, although this observation may have partially resulted from the reduced resolution in the T2 maps compared to the T1-weighted 3D images. T2 values were highest in both treated and untreated mice near the epiphyseal plate. This may be caused by the high tumor burden in those regions due to the presence of hematopoietic niches in the epiphysis and the availability of tumor-promoting cellular and extracellular matrix factors. Interestingly, mean T2 relaxation time was significantly increased in the tibia of the tumor-bearing groups relative to the non-tumor bearing group. The increase in T2 relaxation from the non-tumor group compared to the tumor-bearing groups was not as exaggerated in the femur. These trends may be a function of the underlying composition of the femur and tibia in the C57Bl/KaLwRij model. There is higher hematopoietic and cellular content in the femur BM, with the tibial BM, especially in the distal tibia, dominated by adipose tissue (*21*). In the presence of myeloma, T2 relaxation times increased, although interestingly, the relative difference in T2 relaxation was higher in the treated animals than in the untreated groups. These results suggest that T2 relaxation is indicative of overall tumor burden and post-treatment disease progression.

Histology with H&E staining was used to validate the MRI observations. Tumor burden in the end-stage untreated animals completely displaced normal BM in the femur and tibia. This result approximates advanced MM in humans, with homogeneous, packed diffuse infiltration dominating the BM (*22*). The lack of marrow adipose tissue in the tumor-bearing animals may be partly due to the age of the mice, since significant changes in marrow adipocyte depositions occur in older animals. The study used young, 4-6 week old mice, since young animals have high rates of bone remodeling and higher plasticity in the marrow composition. Both mid-treatment and relapsed end-stage cohorts had reduced tumor burden, which was concentrated proximal to the epiphyseal plate. However, cells in the BM of the mid-treatment group were more densely packed compared to the relapsed group, and were qualitatively similar in density to the end-stage untreated cohort. The observed continuum of cell densities in the treated and untreated groups, and the highly heterogeneous tumor burden in the mid-treatment group, is likely caused by the individual kinetics and response rates to bortezomib therapy. The concentration of the tumor tissue at the epiphyseal plate also agreed with the observed increases in normalized T1-weighted intensity and T2 relaxation times at the epiphyseal plate. The tumor cells were also less densely packed in the treated mice relative to the highly packed tumor tissue in the untreated BM, which likely resulted in improved viability. It is likely that the improvement in tumor viability resulted in the relatively large difference in T2 relaxation time following therapy.

The main limitations of this study are the absence of validation with a focal lesion model a non-tumor bearing, treated control cohort. Contrast uptake and changes in the spatial distribution of signal intensities were affected by the underlying heterogeneity in the distribution of hematopoietic and fatty marrow in the BM. Comparison with a well-circumscribed, focal lesion model may further validate the observations of this study and minimize the effect of spatiotemporal heterogeneity on the imaging results, especially at early and mid-stage disease. Finally, T2 relaxation times and normalized T1-weighted intensities in the both tumor-bearing groups were compared to the non-tumor bearing, untreated cohort. Since mean T2 relaxation times were significantly increased from the non-tumor group to the tumor bearing groups, an additional cohort with non-tumor bearing, bortezomib-treated animals may provide a useful control for therapy-induced inflammation.

4.6 Conclusion

In conclusion, this study demonstrates that T1-weighted CE MRI and T2 relaxation times are indicative of disease progression and response to bortezomib therapy in an immunocompetent intramedullary model of MM. As such, it marks the first instance of using MRI to longitudinally study the behavior of the BM in the preclinical model with diffuse MM infiltration, showing significant histogram and textural feature correlation to viable tumor burden in the presence of myeloma therapy. The study also highlighted potential preclinical MRI markers for assessing changes to the BM induced by MM and therapy. Future studies will include MR spectroscopy to assess changes in adipose tissue composition in response to myeloma in both young and old mice, the use of alternate hypo-proliferative myeloma cell lines, and testing with combination therapies and newer proteasome inhibitors.

4.7 References

1. Becker N. Epidemiology of multiple myeloma. In: Moehler T, Goldschmidt H, eds. *Multiple Myeloma*. Berlin, Heidelberg: Springer Berlin Heidelberg; 2011:25-35.

2. Palumbo A, Anderson K. Multiple myeloma. *New England Journal of Medicine.* 2011;364:1046-1060.

3. Brenner H, Gondos A, Pulte D. Recent major improvement in long-term survival of younger patients with multiple myeloma. *Blood.* 2008;111:2521-2526.

4. Rajkumar SV, Dimopoulos MA, Palumbo A, et al. International Myeloma Working Group updated criteria for the diagnosis of multiple myeloma. *Lancet Oncol.* 2014;15:e538-e548.

5. Moulopoulos LA, Dimopoulos MA, Christoulas D, et al. Diffuse MRI marrow pattern correlates with increased angiogenesis, advanced disease features and poor prognosis in newly diagnosed myeloma treated with novel agents. *Leukemia.* 2010;24:1206-1212.

6. Lee S-Y, Kim H-J, Shin YR, Park H-J, Lee Y-G, Oh SJ. Prognostic significance of focal lesions and diffuse infiltration on MRI for multiple myeloma: a meta-analysis. *Eur Radiol.* 2017;27:2333-2347.

7. Hillengass J, Bauerle T, Bartl R, et al. Diffusion-weighted imaging for non-invasive and quantitative monitoring of bone marrow infiltration in patients with monoclonal plasma cell disease: a comparative study with histology. *Br J Haematol.* 2011;153:721-728.

8. Nosàs-Garcia S, Moehler T, Wasser K, et al. Dynamic contrast-enhanced MRI for assessing the disease activity of multiple myeloma: a comparative study with histology and clinical markers. *J Magn Reson Imaging.* 2005;22:154--162.

9. Oriol A, Valverde D, Capellades J, Cabanas ME, Ribera JM, Arus C. In vivo quantification of response to treatment in patients with multiple myeloma by 1H magnetic resonance spectroscopy of bone marrow. *MAGMA.* 2007;20:93-101.

10. Mitsiades CS, Mitsiades NS, Munshi NC, Richardson PG, Anderson KC. The role of the bone microenvironment in the pathophysiology and therapeutic management of multiple myeloma: interplay of growth factors, their receptors and stromal interactions. *Eur J Cancer.* 2006;42:1564-1573.

11. Hurchla M, Garcia-Gomez A, Hornick M, et al. The epoxyketone-based proteasome inhibitors carfilzomib and orally bioavailable oprozomib have anti-resorptive and bone-anabolic activity in addition to anti-myeloma effects. *Leukemia.* 2013;27:430-440.

12. van Griethuysen JJM, Fedorov A, Parmar C, et al. Computational Radiomics System to Decode the Radiographic Phenotype. *Cancer Res.* 2017;77:e104-e107.

13. Haralick RM, Shanmugam K, Dinstein I. Textural Features for Image Classification. *IEEE Transactions on Systems, Man, and Cybernetics.* 1973;SMC-3:610-621.

14. Linkert M, Rueden CT, Allan C, et al. Metadata matters: access to image data in the real world. *The Journal of Cell Biology.* 2010;189:777-782.

15. Fryer RA, Graham TJ, Smith EM, et al. Characterization of a novel mouse model of multiple myeloma and its use in preclinical therapeutic assessment. *PLoS One.* 2013;8:e57641.

16. Gauvain KM, Garbow JR, Song S-K, Hirbe AC, Weilbaecher K. MRI detection of early bone metastases in b16 mouse melanoma models. *Clin Exp Metastasis.* 2005;22:403--411.

17. Tokuda O, Hayashi N, Matsunaga N. MRI of bone tumors: Fast STIR imaging as a substitute for T1-weighted contrast-enhanced fat-suppressed spin-echo imaging. *J Magn Reson Imaging.* 2004;19:475-481.

18. Falank C, Fairfield H, Reagan MR. Signaling Interplay between Bone Marrow Adipose Tissue and Multiple Myeloma cells. *Front Endocrinol (Lausanne).* 2016;7:67.

19. Zangari M, Suva LJ. The effects of proteasome inhibitors on bone remodeling in multiple myeloma. *Bone.* 2016;86:131-138.

20. Caravita T, de Fabritiis P, Palumbo A, Amadori S, Boccadoro M. Bortezomib: efficacy comparisons in solid tumors and hematologic malignancies. *Nat Clin Pract Oncol.* 2006;3:374-387.

21. Bartelt A, Koehne T, Tödter K, et al. Quantification of Bone Fatty Acid Metabolism and Its Regulation by Adipocyte Lipoprotein Lipase. *Int J Mol Sci.* 2017;18:1264.

22. Bartl R, Frisch B, Burkhardt R, et al. Bone-Marrow Histology in Myeloma - Its Importance in Diagnosis, Prognosis, Classification and Staging. *Br J Haematol.* 1982;51:361-375.

Chapter 5: Conclusions and Future Work

5.1 Summary

This thesis aimed to identify preclinical imaging markers correlating to therapy response in MM for efficient imaging, with the long term goal of improving staging and patient stratification. To achieve this goal, the project was designed to address myeloma pathogenesis and therapy efficacy through a micro-environmental lens at different levels of granularity. Thus, these studies followed myeloma progression and response to clinically relevant therapies through three specific aims:

Aim 1: To validate LAT1 surface expression imaging using FDOPA-PET and develop FDOPA-PET uptake metrics as a surrogate for melphalan efficacy

In this study, I adapted the phenylalanine analog ^{18}F-FDOPA for imaging melphalan therapy response in extramedullary myeloma. The uptake of melphalan and ^{18}F-FDOPA is mediated by LAT1, which is overexpressed in several cancers and is linked to poor prognosis in MM. ^{18}F-FDOPA uptake was significantly reduced in melphalan-treated mice, as was uptake of the gold standard ^{18}F-FDG. These results demonstrated that ^{18}F-FDOPA-PET provides complementary imaging of LAT1 behavior in MM to currently established ^{18}F-FDG-PET.

The conclusions regarding ^{18}F-FDOPA and ^{18}F-FDG were validated using immunohistochemistry of the tumor and muscle tissue using antibodies against LAT1, GLUT1, and CD31. GLUT1 and CD31 are markers for glucose uptake and vascularity, respectively. LAT1 expression in melphalan-treated tumors was heterogeneous, and was increased relative to vehicle-treated tumors in some animals, while GLUT1 expression remained qualitatively similar between the treated and untreated cohorts. This heterogeneity in LAT1 expression is likely driven by an increase in tissue vascularity, as visualized by anti-CD31 staining, and reduction in structural tumor volume. These results highlight the importance of LAT1 for myeloma cell function, and imply the presence of other sources of resistance to offset the melphalan-induced downregulation of LAT1 expression.

Aim 2: To study the uptake of the VLA-4 specific optical contrast agent for identifying VLA-4 expression *in vivo* and in response to bortezomib therapy

In this aim, I comprehensively validated the peptidomimetic near-infrared fluorophore LLP2A-PEG$_4$-Cy5 (LLP2A-Cy5) for economical and high-throughput imaging of activated VLA-4 expression. The Shokeen research group has extensively published on the use of the nuclear LLP2A analog for imaging activated VLA-4 expression in intramedullary myeloma pathogenesis. Furthermore, we have shown cell line and patient-specific heterogeneity in VLA-4 expression using the fluorescent LLP2A-Cy5. Here, we were interested in imaging VLA-4 expression following bortezomib therapy, since bortezomib induces downregulation of VLA-4 and causes partial inhibition of cell adhesion-mediated drug resistance. Imaging was performed in intramedullary, diffuse lesions, within an immunocompetent MM model to accurately study effects of the immune system on MM pathogenesis.

The results of this aim proved the sensitivity and specificity of LLP2A-Cy5 relative to the more established nuclear LLP2A conjugate. *In vitro* studies showed nanomolar specificity of LLP2A-Cy5 to activated VLA-4 expression, while confocal imaging established the predominantly cell surface concentration of LLP2A-Cy5 binding. *Ex vivo* analysis of LLP2A-Cy5 uptake demonstrated the viability of using activated VLA-4 expression for studying the effects of proteasome inhibitor therapy in MM.

Aim 3: To identify preclinical MRI parameters for longitudinal imaging of diffuse, intramedullary tumor burden in response to myeloma therapy

Finally, in aim 3, I addressed the gross, anatomical scale changes in the BM induced by both MM disease progression and response to bortezomib therapy. Bortezomib induces BM remodeling in addition to abrogating adhesion-mediated drug assistance. To assess BM remodeling in a longitudinal manner in a diffuse infiltrative intramedullary MM model, I evaluated preclinical, high-resolution MRI parameters. While MRI is used extensively in MM clinical care, there is a scarcity of preclinical MRI studies for noninvasive, longitudinal imaging of MM pathogenesis. In this study, MR T1-weighted and T2 parametric markers were correlated to structural changes in the BM following bortezomib therapy.

The MR imaging results were validated with histology of the femur and tibia BM at each treatment stage. H&E staining of the BM was used to assess tumor burden. In untreated animals, end-stage disease caused near-complete infiltration of the BM space by myeloma cells, while in end-stage, treated disease, the tumor was primarily concentrated near the epiphyseal plate in the distal femur and proximal tibia. These observations correlated to T1-weighted contrast uptake and parametric T2 using both summary statistics and spatial analysis. Crucially, high-resolution imaging established the spatial heterogeneity between BM sites.

5.2 Limitations

There are certain limitations to our approach in this project. Most aim-specific limitations are addressed in each chapter individually, but there were some inherent, general limitations that may affect the results in the project. The primary limitations were the use of a single myeloma cell line and sample sizes in some of the experiments. Both limitations are easily addressed by additional validation studies.

Additionally, in aim 1, the use of the 5TGM1-GFP cell line presented translatability challenges, due to two main factors. The cell line is highly proliferative, resulting in rapidly growing tumors, which do not necessarily represent the general MM progression, where the medullar spaces motivate quiescence and slow growth. As a result of this growth behavior, 5TGM1 cells are also highly glucose avid, which increases ^{18}F-FDG intratumoral uptake. In the general MM population, the overexpression of GLUT1 and hexokinase is inconsistent, resulting in poor ^{18}F-FDG sensitivity in intramedullary disease. These concerns were slightly abrogated due to the use of a late-stage, extramedullary model, although it may be necessary to study intramedullary models to establish ^{18}F-FDOPA-PET for use in MM care.

In aims 1 and 2, single time point imaging was used, at the end-stage of the treated and untreated groups. This was done to reduce complexity inherent in longitudinal imaging. However, due to clonal and spatiotemporal heterogeneity in intra- and inter- patient levels, the comparison of these two groups may lose relevant information regarding changes in expression resulting from disease progression. Use of longitudinal imaging would be especially helpful for aim 2, where end-point imaging of the LLP2A-Cy5 contrast reduces the value of fluorescent imaging.

In aim 3, the intra-site heterogeneity was hinted at, but not fully studied. Imaging of the femur and tibia BM showed regional differences in viable tumor burden and BM recovery following bortezomib therapy. In clinical MM care, MRI of the spinal column and vertebrae is combined with the leg bone imaging. Furthermore, in patients, the distal BM is primarily composed of adipose marrow, with hematopoietic marrow concentrated in spinal and pelvic sites. Our model did not approximate this behavior, since we used young, 6-8 week old mice. These mice were used due to their rapid bone turnover and corresponding BM activity, which exaggerated the myeloma-induced changes in the BM for MR validation.

Finally, we used single agent therapies for each of our aims to simplify the experimental models and validate the imaging strategies. Single agent treatment is not used in clinical care to delay the onset of resistance to the individual agents. Future studies should address this limitation by using clinically relevant combinations to study the effect on the targeted imaging biomarkers for increasing the translatability and clinical value of the imaging strategies tested in this thesis.

5.3 Future work

As with the limitations, aim-specific future studies were addressed in each chapter. Here, briefly, there are some general future studies that could be performed to improve upon the results and conclusions generated by each aim.

One important addition to the intramedullary model would be to test intramedullary imaging on focal lesions, since MM patients typically have a combination of diffuse and focal BM lesions. Such a model would be generated using direct injection of cells into the tibia. Crucially, this approach also generates metastatic tumor burden at late stages of the disease, and may also show diffuse infiltration in the spinal column. Use of multiple cell lines can also approximate different MM pathogenic behaviors for assessing the robustness of each biomarker in the presence of heterogeneous protein expression and growth profiles.

This thesis highlighted use of longitudinal imaging for identifying changes in the BM microenvironment in response to disease progression and treatment response. The use of the 5TGM1 cell line also allowed the influence of the intact immune system on the myeloma pathogenesis, although due to the rapid proliferation profile *in vitro* and *in vivo*, disease progression within the BM was accelerated. In addition, the cell line presented an external stressor, which may have adversely affected the biology, resulting in potentially inaccurate conclusions drawn from the imaging data. As a result, one exciting strategy for studying changes in biomarker expression and BM remodeling is to use naturally progressing MM model with the vk*myc animal model. Longitudinal imaging in this model would help identify novel features that could be directly translated for clinical care.

Finally, there is growing availability of tandem PET and MRI systems (PET/MRI) that aim to utilize the functional imaging and high-resolution, soft tissue contrast of the constituting technologies. Our work has highlighted the use of each technology in assessing changes to expression of critical surface markers and the overall BM structure. Therefore, there is potential for using PET/MRI to generate co-registered results that can be used for early stratification of therapy response.

5.4 Conclusions

In conclusion, this study used a combination of qualitative observations and quantitative metrics for addressing therapy response monitoring and stratification in MM. We took an integrated, multi-modal approach to assessing therapy response by observing changes to a spectrum of myeloma pathogenic behaviors. This structured approach harnessed the unique role of the BM microenvironment in supporting MM progression and response to clinical relevant therapies. In doing so, we have validated the use of several imaging markers in preclinical MM models that have translation potential.